Università degli Studi di Cagliari

PhD Thesis

DOTTORATO DI RICERCA

Corso di Dottorato in Scienze e Tecnologie Chimiche

Ciclo XXVII

Settore scientifico disciplinare di afferenza CHIM/02

Matteo Sestu

The structure of nano sized poorly-crystalline iron oxy-hydroxides

Coordinatore Dottorato: Prof. Mariano Casu

Relatore: Dott. Gabriele Navarra

A.A. 2013 – 2014

The structure of nano sized poorly-crystalline iron oxy-hydroxides

Matteo Sestu

Dipartimento di Scienze Chimiche e Geologiche

Universita' degli Studi di Cagliari

A thesis for the degree of

Doctor of Philosophy

03 13 2015

The structure of nano sized poorly-crystalline iron oxy-hydroxides

---

Author: Matteo Sestu
Supervisor: Gabriele Navarra

Matteo Sestu gratefully acknowledges Sardinia Regional Government for the financial support of his PhD scholarship (P.O.R. Sardegna F.S.E. Operational Programme of the Regione Autonoma della Sardegna, European Social Fund 2007-2013 - Axis IV Human Resources, Objective l.3, Line of Activity l.3.1.)

Ai miei genitori

"Nature is a language, can't you read?"
Ask, The Smiths

Acknowledgements

I would like to acknowledge

- Gabriele Navarra, for our long fruitful scientific cohabitation
- Maria, Danilo, Claudia and all the people that "went through" the Functional Materials Team
- Erika, who shares with me the PhD experience
- Anna, Gavin and Andrea for their precious scientific, and especially human, contribution
- The Elettra MCX and XAFS Teams
- Alex, for being so kind. I hope that our collaboration will continue in the future
- All the colleagues of the Sala Dottorandi and all the colleagues that in these years shared lunches and laughs with me
- Francesco, Bruno and all my colleagues in Kent. Please, keep in mind the importance to enjoy lunch in UK!
- Joe, for his essential work
- My father, my brother, my comrades and my friends
- The "Regione Autonoma della Sardegna" for funding the PhD grant

Abstract

In this thesis the structures of three nano sized poorly-crystalline iron oxy-hydroxides, feroxyhyte, ferrihydrite and schwertmannite, are studied and analyzed with the aim of clarifying some dubious structural features. The widely used Rietveld refinement and EXAFS analysis are employed in order to address the consistency of the structural models proposed for these materials, one of which, feroxyhyte, is suggested in this thesis. Furthermore, a new computer program exploiting the Reverse Monte Carlo algorithm and the Debye Scattering Equation is presented and used in order to analyze the elusive structures of these iron oxy-hydroxides.

Contents

List of Figures

Chapter 1

Introduction

The study of the structure of crystals has recently celebrated its centenary. During this time enormous improvements have been made: theories have evolved for x-ray, neutron and electron diffraction and x-ray absorption and fluorescence; many experimental techniques have been developed following the growth of the theories; more and more powerful facilities, from small diffractometers in research laboratories to large synchrotrons, from microscopes to neutron reactors, are available to the scientific community; the invention and the tremendous advancement of computer processing has allowed the development of programs able to control instruments, analyze data, predict results and simulate structural models. Nowadays, the study of the structure of complex organic molecules appears to be within reach of thousands of people. In spite of that, the structure of some inorganic phases even with very simple stoichiometry remains so far undetermined or ambiguously solved. In this thesis we discuss the structure of three iron oxy-hydroxides, feroxyhyte, ferrihydrite and schwertmannite, the structures of which are not completely known. This is due to their nanometric size and the presence of disorder, which produce elusive diffraction patterns. These iron oxy-hydroxides are widely used as pigments or as adsorbents and they present very interesting chemistry from a geological point of view, although in this thesis we will focus only on their structure: advanced studies are presented with the aim to clarify some dubious structural features. Because of their poorly-crystalline nature, the techniques traditionally used for solving crystal structure fails to accurately describe the diffraction patterns. On the other hand, their structure is not amorphous and we cannot exclusively rely upon methods of determining short range order and local structure. In this thesis, three techniques are principally used: the first two are the popular and widely used Rietveld Refinement on powder diffraction patterns and EXAFS. The third represents the more original contribution to this work. A computer program combining the Debye Scattering Equation and the Reverse Monte Carlo algorithm is built and used for the

refinement of nanoparticles. The program runs partially on graphics processors to speed up computation time. These techniques are applied to study the structure of feroxyhyte, ferrihydrite and schwertmannite. This thesis is organized as follows: the Chapter 2 is dedicated to the family of iron oxy-hydroxides. Their common structural features are displayed and an overview of the proposed models for feroxyhyte, ferrihydrite and schwertmannite is presented. In Chapter 3 the x-ray diffraction and absorption theory is illustrated briefly, with a specific interest in the study of the structure of nanomaterials. The computer program introduced above is described completely in Chapter 4, with a specific section dedicated to the calculation of diffraction patterns using graphics processors. Sample synthesis and characterization and structural analysis of feroxyhyte, ferrihydrite and schwertmannite are examined in Chapters 5, 6 and 7 respectively. Concluding remarks close the thesis in Chapter 8. We hope to stimulate the interest of the reader and offer some food for thought.

Chapter 2

Poorly-crystalline iron oxy-hydroxides

2.1 The family of iron-oxides

Iron oxides are common compounds occurring in nature. With the term iron oxides we refer to either the proper oxides, or the oxy-hydroxides and hydroxides. They are present in ores, waters, soils, rocks and they also play an important role in biological processes. As a trivial example, common rust belongs to this family. In Figure 2.1 a general scheme of the global iron-oxides system detailing their occurrence and uses is shown [1].

They are used in industry both as catalysts and precursors in the production of metallic iron or iron alloys (steel) [6]. In recent decades growing attention has been focused on the magnetic properties of iron oxide nanoparticles, which strongly depend on size. Iron oxides display a large range of different colors (yellow, red, orange, dark brown). A table of the colors of the main phases is shown in Figure 2.2. Due to their natural occurrence and wide-spread availability, iron oxides have been used as pigments since prehistoric times.

As shown in Table 2.1, there are 16 known iron oxides. Goethite and hematite are the most wide-spread, due to their higher thermodynamic stability. Goethite occurs in almost all soils and other surface formations (e. g. lakes, streams), whereas hematite is a typical component of soils of tropical and subtropical regions, in the presence of higher temperatures and less abundant water. The heating process in atmospheric conditions of any Fe oxide generates hematite. Goethite has also been found in the teeth of certain mollusks (limpets, chitons) [7], but as yet, hematite has not been found in any living organism.

Lepidocrocite formation is favored in environments containing Fe^{2+}, from which it is synthesized by oxidation. Its formation is competitive with the for-

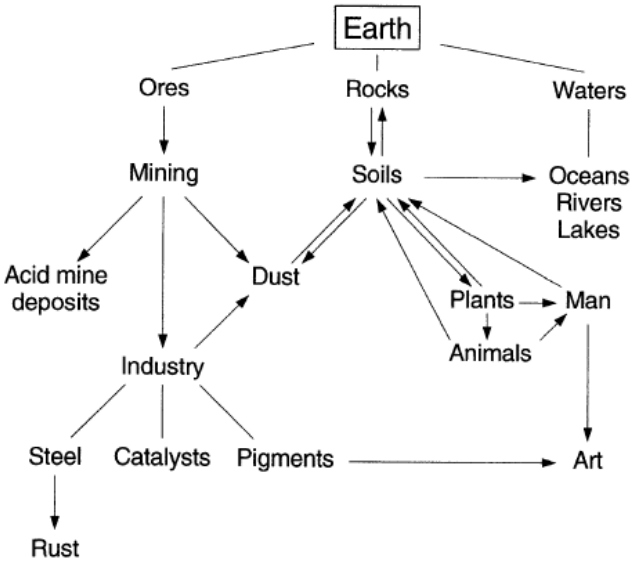

Figure 2.1: Scheme of the global iron oxides system [1].

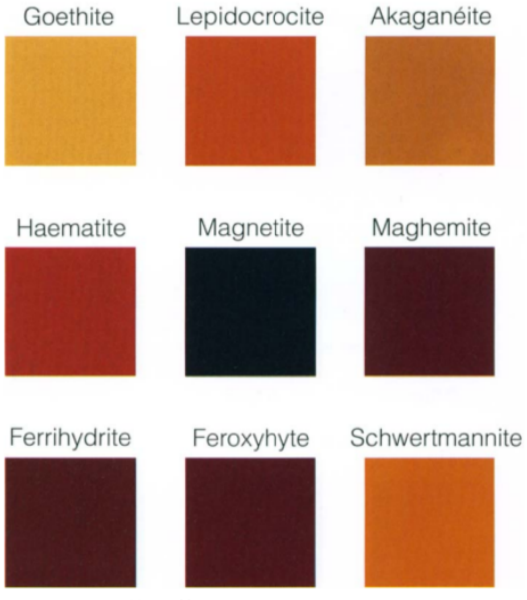

Figure 2.2: Table of colors of the main iron oxides [1].

Mineral Name	Formula	Magnetism	Density (g cm^{-3})
iron oxy-hydroxides			
goethite	α -FeOOH	antiferr	4.26
lepidocrocite	γ -FeOOH	antiferr	4.09
akaganeite	β -FeOOH	antiferr	
schwertmannite	$Fe_{16}\ O_{16}\ (OH)_y\ (SO_4)_z\ nH_2O$	antiferr	3.8
feroxyhyte	δ -FeOOH	ferrimag	4.20
high pressure	FeOOH		
ferrihydrite	$Fe_5HO_8 \cdot 4H_2O$	speromag	3.96
bernalite	$Fe(OH)_3$		3.32
	$Fe(OH)_2$		
green rusts	FeOOH (non stoich.)		
iron oxides			
hematite	α -Fe_2O_3	antiferr	5.26
magnetite	Fe_3O_4	ferrimag	5.18
maghemite	γ -Fe_2O_3	ferrimag	4.87
	β -Fe_2O_3		
	ϵ -Fe_2O_3		
wustite	FeO (non stoich.)	antiferr	5.9

Table 2.1: The family of iron oxides.

mation of goethite and, despite it being a metastable phase, it may be kinetically favored. Lepidocrocite is found in living organisms including sponge spicules and the teeth of chitons [7]. Also magnetite, which is a mixed Fe(III) and Fe(II) oxide, requires Fe^{2+} environments, although its formation requires basic conditions. It is the most common material in the manufacture of magnetic storage devices. It commonly occurs in rocks, however, it can be formed in surface environments by biological processes: it has been found in various bacteria (magnetotactic bacteria) [8] [9], bees and pigeons [10] [11]. Due to its magnetic properties, the presence of magnetite should be related to the directional sense of these organisms. Maghemite is obtained from the oxidation of magnetite. It is found in the soils of the tropics and subtropics. Another, probably widespread mechanism involves conversion of other Fe oxides such as goethite under heat (from bush or forest fires) and the presence of organic matter. Akaganeite contains chloride ions trapped in the channel of its structure. The presence of chloride is then an essential prerequisite in its formation, which also needs elevated temperatures (60^oC). Ferrihydrite, feroxyhyte and schwertmannite are thermodynamically unstable and can be found only in the form of nanosized and poorly-crystalline particles. They have an important role in controlling the formation and interconversion of more stable iron oxides. Feroxyhyte is found in some soils, ocherous bands of Pleistocene sediments and in marine concretions, but its natural occurrence is rare. Its formation involves rapid oxidation in Fe^{2+} environments [12]. Also ferrihydrite occurs mainly in situations where Fe^{2+} is oxidized rapidly or where crystallization of Fe^{3+} solutions is inhibited by organics, phosphate or silicate species. Ferrihydrite is found in drainage lines, lake oxide precipitates, ground water and stagnant-water soils and spodosols, river sediments and, in the oceans, deep sea crusts and Mn nodules [13]. Ferrihydrite has been detected in the core of ferritin, an intracellular protein that stores and releases iron in living organism which acts as an iron reservoir [14]. Its concentration in ferritin seems to be related to Alzheimers disease [15]. The stoichiometry for this iron oxy-hydroxide is not widely accepted and variable water contents are found. As proof of its ambiguous nature, ferrihydrite is commonly defined as 2L or 6L, depending on the number of the main peaks observed in the x-ray powder diffraction pattern, which is related to the size of the scattering domain and the presence of more structural disorder. Schwertmannite is a sulfate iron oxy-hydroxide and it is a common precipitate in iron-rich, acid sulfate waters, like natural water courses draining pyrite (FeS_2) or lakes and streams affected by acid mine drainage [16]. Its formation is commonly associated with the presence of the iron minerals goethite and jarosite ($KFe_3(SO_4)_2(OH)_6$). In this thesis the structure of feroxyhyte, ferrihydrite and schwertmannite is studied in depth and discussed. In fact feroxyhyte, ferrihydrite and schwertmannite are poorly-crystalline materials with elusive diffraction patterns which feature broad peaks and diffuse scattering. Because of that, their

structures are not unambiguously determined: different models were proposed in literature and the debate continues to this day.

2.2 Structural features of iron oxides

The basic structural unit of all iron oxides is an octahedron. Depending on whether or not it is a proper oxide or a hydroxide, each Fe atom is surrounded by six O or by both O and OH ions. Tetrahedral coordination occurs only in the structure of the oxides magnetite and maghemite. The most common anion network in iron-oxides is hexagonally close-packed (hcp). Goethite and hematite show this structural packing, and for this reason, they are both termed $\alpha-phases$. Approximate cubic close packing (ccp) occurs in lepidocrocite and maghemite, termed $\gamma-phases$. The structural differences among Fe oxides are mainly found in the arrangement of the octahedra. In iron oxides corner, edge and face-sharing occurs between octahedra. In hematite [17], the octahedral sites in the hexagonal close packing of oxygen atoms are two thirds filled by iron atoms, in a way that pairs of octahedra share faces along the z axis. One octahedron of the pair is linked in the x-y plane with three octahedra of the other three pairs via edge-sharing. The resulting structure is shown in Figure 2.3. The distance from two centers of octahedra sharing faces is energetically too short for iron atoms, causing a shift of the site towards the unshared face and a distortion of the sublattice. Magnetite (Figure 2.4 and Figure 2.5) shows an inverse spinel structure [18], with octahedral and tetrahedral sites in the 2:1 ratio. Divalent iron occupies only octahedral sites, whereas trivalent iron occupies both tetrahedral and octahedral sites. Maghemite has a structure extremely close to that of magnetite [19]. All of the cations are trivalent, so some of the octahedral sites are partially occupied in order to balance the charge. Depending on the synthesis procedure and on the size of crystallites, vacancies can be randomly or tidily distributed.

Iron oxy-hydroxides with well-known structures do not exhibit octahedral face-sharing. goethite [20], lepidocrocite [21] and akaganeite [22] structures (Figures 2.6, 2.7 and 2.8) show similar network features: pairs of octahedra sharing edges are linked to others by corner-sharing and run parallel along one axis, creating channels. Hydrogen atoms are hosted in the channels and hydrogen bonds are established between the oxygen atoms belonging to different octahedra. In the structure of akaganeite the channels host chlorine atoms and its formation is strictly related to the presence of $FeCl_3$. Depending on the linkage between octahedra, different Fe-Fe distances may be observed. Face-sharing causes a shift of the iron atom from the center. In hematite, Fe-Fe minimum distance is 2.89 Å, whereas the distance between the centers of two octahedra sharing faces is 2.67 Å. Due to this distortion, significant differences between Fe-O distances occur.

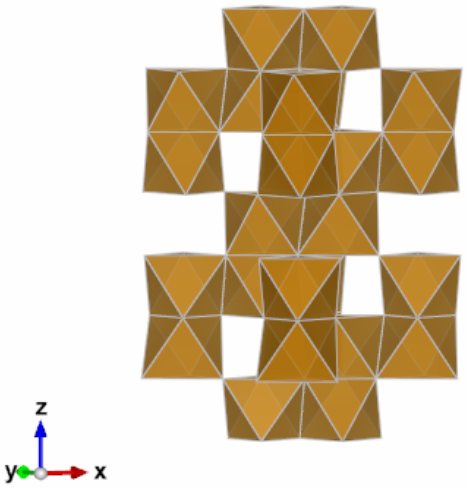

Figure 2.3: The structure of hematite.

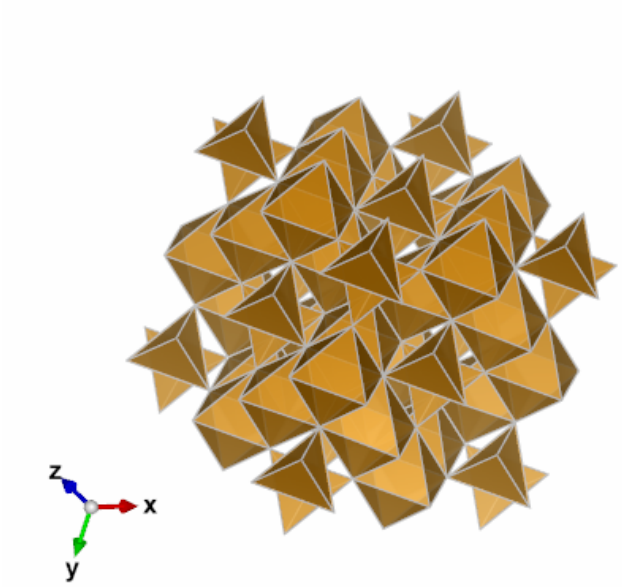

Figure 2.4: The structure of magnetite.

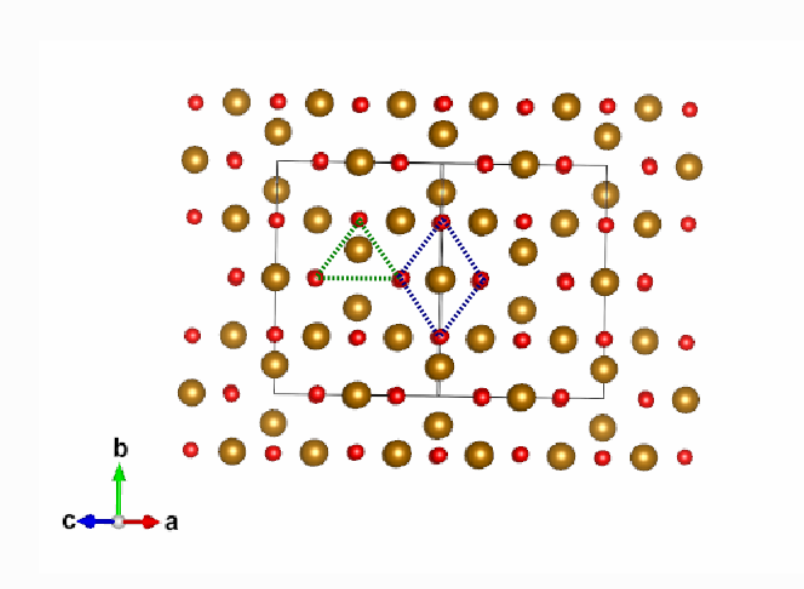

Figure 2.5: The structure of magnetite: tetrahedral (green) and octahedral (blue) sites can be recognized along (110) direction. Unit cell is delimited in black.

Fe-Fe distance for octahedral edge-sharing depends on the angle between the two octahedra and on the distortion of the polyhedron. Due to the shift from the center of the octahedron in hematite, a 2.97 Å Fe-Fe distance is observed for octahedra sharing edges. Iron oxy-hydroxides have both O^{2-} and OH^{-} groups bonded to the iron atom. Different first Fe-O distances occur, causing distortion of the octahedron and therefore different Fe-Fe distances: 3.06 Å in lepidocrocite, 3.05 Å in akaganeite and 3.01 Å and 3.26 Å in goethite. Fe-Fe distances greater than 3.4 Å are related to octahedra sharing corners. First Fe-O distances are generally found in the range between 1.9 Å and 2.2 Å. In magnetite and maghemite slightly shorter distances are observed for Fe and O atoms which are tetrahedrally arranged. In Figure 2.9 the diffraction pattern for the main iron oxides are reported [1].

2.3 Structural models for feroxyhyte

The feroxyhyte structural models proposed so far have a hematite-like structure, although none of the well-known structures of iron oxy-hydroxides display face-sharing octahedra. The only exception is given by Okamoto [23], where face-sharing is excluded on the basis of magnetic measurements. The more recent

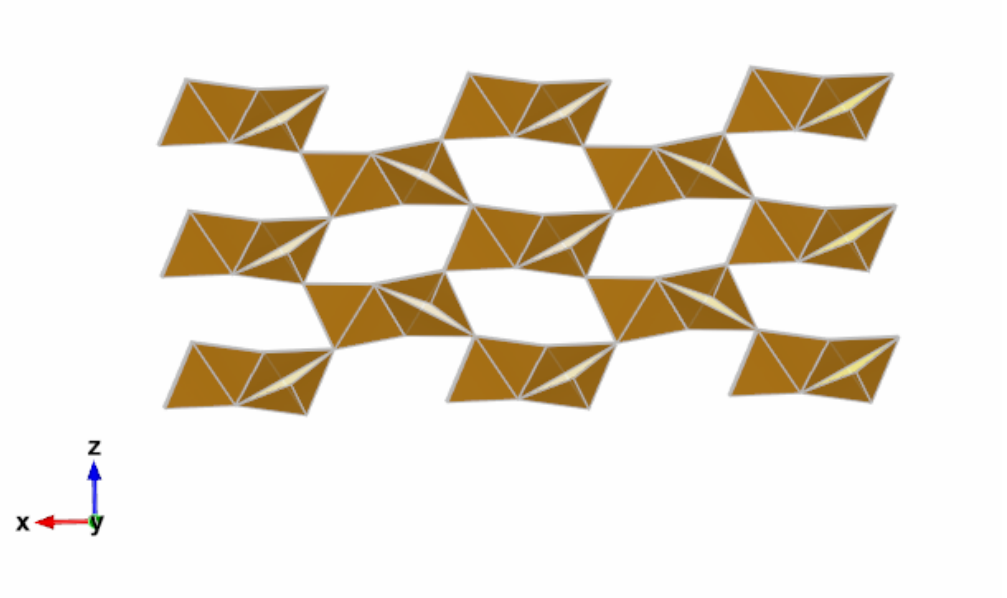

Figure 2.6: The structure of goethite.

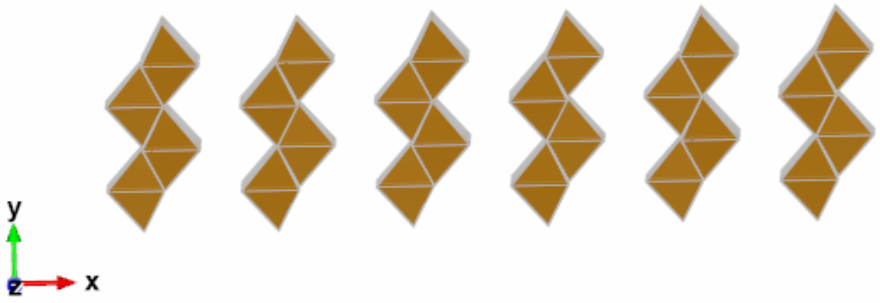

Figure 2.7: The structure of lepidocrocite.

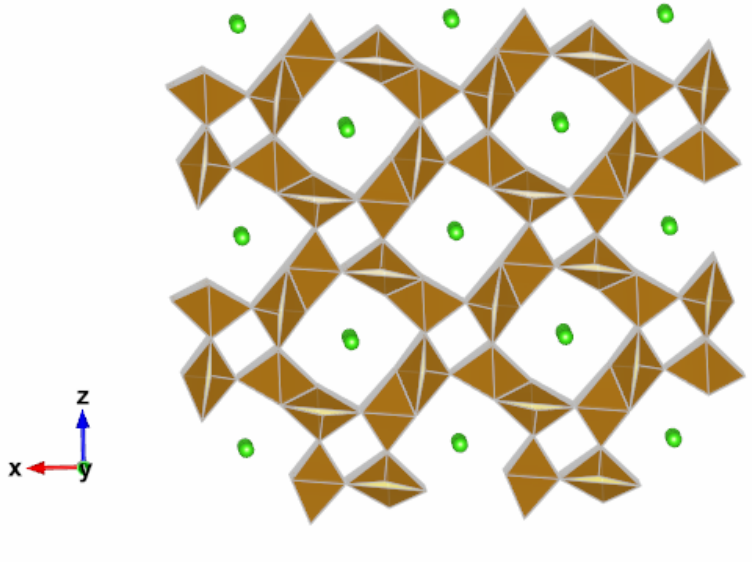

Figure 2.8: The structure of akaganeite.

models are presented by Patrat (1983) [24] and Drits (1993) [3]. The latter represents the current accepted model describing the feroxyhyte structure. This model considers feroxyhyte as a mixture of two different phases, proper feroxyhyte and ultradispersed hematite in the 9:1 volume ratio. According to the Drits model the structure of proper feroxyhyte shares the main local structural features of hematite: iron occupies octahedral sites and octahedra share edges, corners and faces. In particular, Drits suggests that the local structure of feroxyhyte is made by face-sharing octahedra-chains along the z-axis: two octahedral sites occupied by the iron atom are followed by two unoccupied sites (Figure 2.10a). Depending on the position of the occupied octahedra sites, four kinds of chains can be detected (called 0, 1, 2, 3 in Figure 2.10b). These chains are randomly distributed over the hexagonal-lattice nodes of the x-y plane. In the Drits model the iron atoms are shifted 0.3 Å in opposite directions along the c-axis from the center of the face-sharing octahedra to ensure that the Fe-Fe distance is 2.88 Å, as in hematite. The unit cell describing this structure is shown in Figure 2.10c and is a slight modification of the cell previously proposed by Patrat et al. It belongs to the trigonal crystal system (space group P-3m1) and it contains two oxygen atoms located in a 2d site and one iron atom which can be set in four different positions along the c-axis, each one with site occupancy factor (SOF) equal to 0.25 (Table 2.2).

It is interesting to note that face-sharing octahedra do not occur in the other

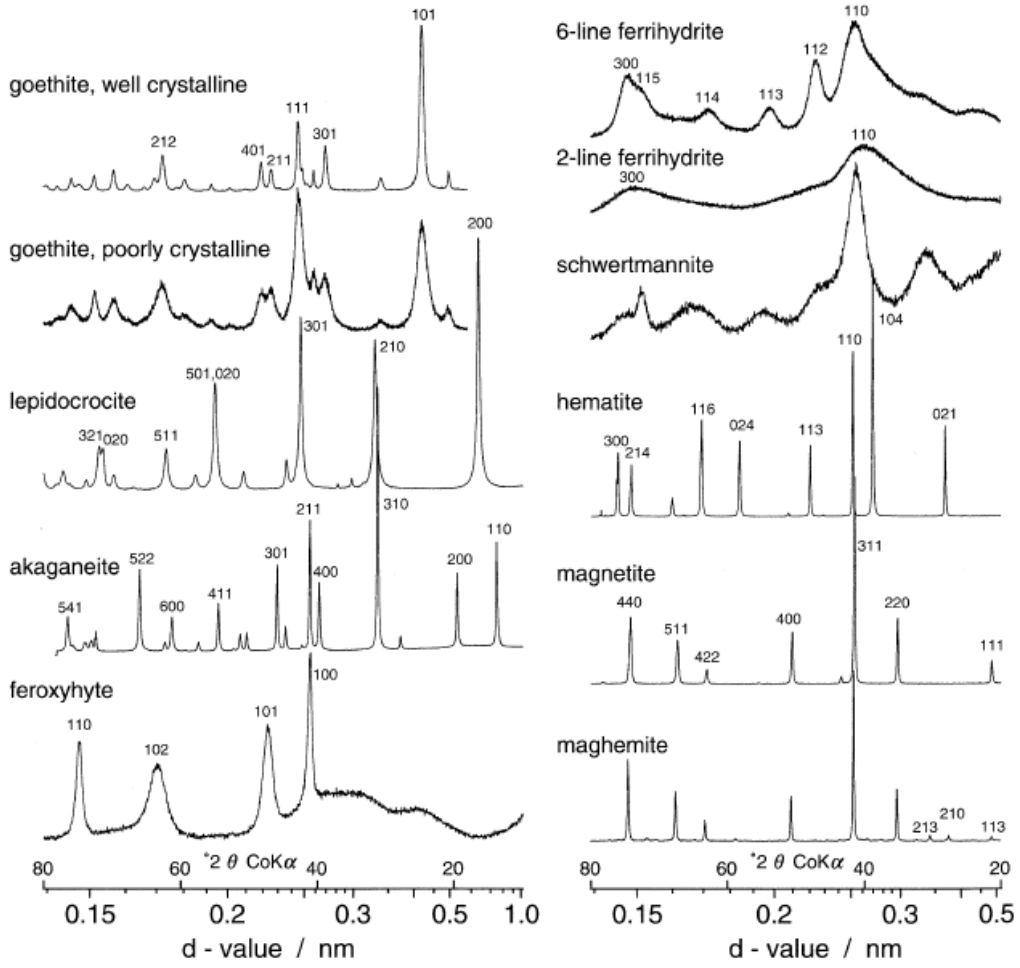

Figure 2.9: Diffraction patterns of the iron oxides [1]. Miller index in ferrihydrite and feroxyhyte patterns are referred to the unit cells proposed by Drits [2] [3].

Atom	Site	x	y	z	SOF
Fe1	2c	0	0	0.065	0.25
Fe2	2c	0	0	0.435	0.25
O	2d	1/3	2/3	0.25	1

Table 2.2: Atomic coordinates and sites occupancy (SOF) of the unit cell for the Drits model of feroxyhyte (space group P-3m1, a = 2.947 Å, c = 4.56 Å).

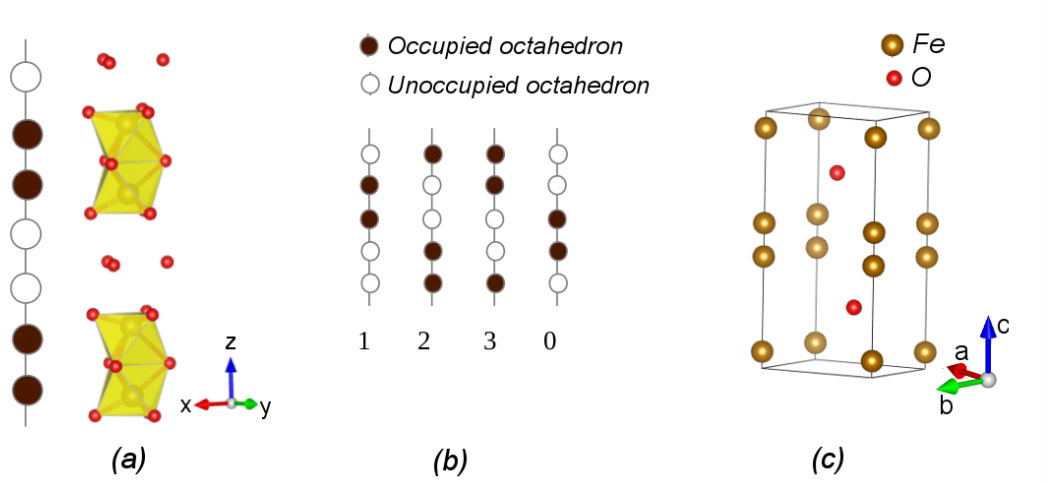

Figure 2.10: (a) Octahedra-chains along the c-axes in which two occupied site at the center of the octahedra are followed by two vacant octahedra, corresponding to the main local structure network in the Drits model for feroxyhyte (see Drits et al., 1993). These chains can be of type 0-3 depending on the position of the vacant (empty circle) and occupied (filled circle) octahedra along the c axes (b); (c) the average cell proposed by Drits (atomic coordinates and sites occupancy in Table 2.2).

iron oxy-hydroxides with well-known structures, goethite, lepidocrocite and akaganeite and that the face sharing occurrence predicted by the Drits model is in contrast with magnetic measurement results [23]. With the aim of integrating the structure of feroxyhyte among those of other, well characterized iron oxy-hydroxides, an interesting correspondence between the mean cell proposed by Drits and the structure of goethite is found by Sestu et al [25]. The authors show that a mean model can be built using a number of local structures sharing characteristics common to the other iron oxy-hydroxides, that is to say that a mean structure very similar to that proposed by Drits can be obtained taking into account local structures different from the one proposed by Drits. This topic will be addressed in detail in Chapter 5.

2.4 Structural models for ferrihydrite

The same short range structure seems to be present in both ferrihydrite 6L (fh6L) and ferrihydrite 2L (fh2L) [1]. Differences are hypothesized to be related to the size of the particles, with fh6L showing a coherently scattering domain of the 3 to 10 nm limit (most crystallites are 5-6 nm across) and fh2L showing a consistently smaller scattering domain (2-4 nm) [26]. Several models were proposed for ferrihydrite [27; 28; 29], but the first consistent model appeared in 1993 (Drits et al. [2]), on the basis of the agreement between experimental and calculated diffraction patterns and EXAFS results [30]. According to Drits, ferrihydrite consists of a mixture between three different phases: defect-free ferrihydrite, defective ferrihydrite, ultradispersed hematite. The defect-free phase shows an ABACA oxygen packing sequence in which iron atoms occupy 50% of the available octahedral sites. In Figure 2.11b the unit cell is shown. The defective phase has a feroxyhyte-like structure and can be interpreted as a defect-free phase with stacking faults. The oxygen atoms forms an ABABA or an ACACA layer sequence in which iron atoms are located on the octahedral interstices. Similarly to feroxyhyte, iron atoms are shifted from the center of the octahedra as a consequence of the octahedral face-sharing occurrence. The representative unit cells are shown in Figure 2.11a. Defect-free and defective phases occur in the 2:1 ratio. Hexagonal superlattices may form from the defect-free phase. The authors suggested also the presence of 25% of ultradispersed hematite. This complex model, composed of several different structural networks, is reflected in electron nanodiffraction analysis [31] and Rietveld Refinement from neutron scattering data [32]. The latter shows differences regarding the abundance of the phases: defect-free and defective ferrihydrite were estimated with the same percentage and no hematite was required to obtain a good fit. In 2007 Michel et al. showed a new model on the basis of PDF calculations [33]. In this model, ferrihydrite is isostructural

with the Al oxy-hydroxide akdaleite ($Al_{10}O_{14}(OH)_2$). The structure, shown in Figure 2.12, in ideal form consists of 20% of the iron atoms involved in tetrahedral coordination and the remaining 80% in the typical octahedral coordination. According to Michel, depending on the size of the domains, occupancy of iron atoms may change and defects, surface-relaxation effects and water molecules on the surface are hypothesized. Some authors criticized the model proposed by Michel with respect to several aspects:

1. The calculated diffraction pattern of the Michel model is not completely in agreement with the observed diffraction pattern [34; 35];The density of the Michel model, including Fe vacancies, is 4.9 g/cm^3, whereas 3.96 g/cm^3 is found with pycnometric measurement [27; 34];

2. Although the stoichiometry of $Fe_5O_8H \cdot 4H_2O$ is not widely accepted, the Michel model is tremendously poor in hydrogen [34];

3. The Michel model does not reproduce the experimental EXAFS data, neither in the k-space, nor in the r-space [35];

4. The Pauling's 2^{nd} rule for ionic structures, which states that the sum of the bond valences around each atom or functional group in a structure should equal its oxidation state, is violated [36];

Furthermore the presence of tetrahedral coordination is controversial [34]. The structure of the other iron oxy-hydroxides does not show this feature. In 2010 Michel revised his model on the basis of a study regarding phase transformation from fh2L to hematite using citrate [37]. The previous model has been changed with respect to the positions of some atomic sites and occupancies. New positions were in accordance with the Pauling's 2^{nd} rule and improved the agreement between experimental and calculated pattern, although not entirely negligible differences persist [38], whereas using new occupancies the density is 4.0 g/cm^3 and the stoichiometry is no longer H-poor ($Fe_{8.2}O_{8.5}(OH)_{7.4} \cdot 3H_2O$). PDF analysis on neutron diffraction data [39] and high resolution EXAFS results [38] agreed with revised Michel model, the latter focusing on the possible Fe tetrahedral coordination. The authors show that first Fe-O distances in Fh are found to be closer to that of maghemite, than to those of goethite or hematite. Nevertheless, some of the previous remarks remain (i.e. the agreement of the Michel model with EXAFS data) and further criticisms were pointed out regarding the possible presence of maghemite in the samples used by Michel in order to infer his model [40] and the presence of anomalous O-O distances [36]. In 2013 a new model as a hybrid between Drits and Michel models has been presented [41]. In this work a RMC refinement on single particle model has been performed on the Drits model, the Michel model and a third model representing a structural mixture of

the two. The hybrid model, which shows tetrahedral coordination, seems to be in agreement both for reciprocal and real space diffraction data.

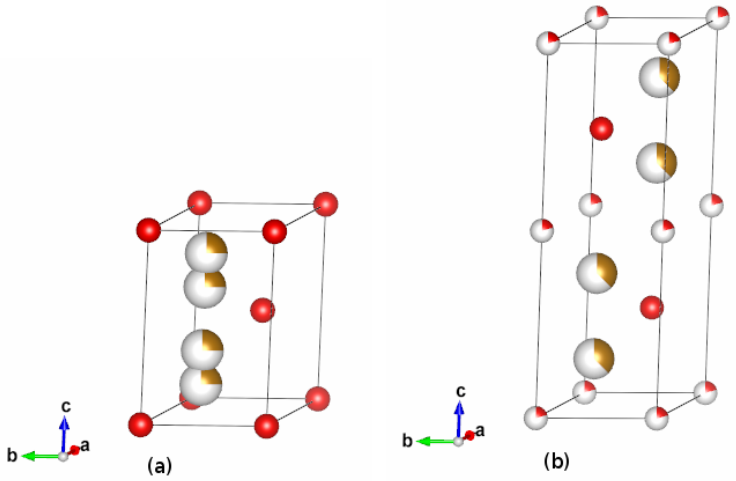

Figure 2.11: Defective (a) and defect-free (b) cells of the Drits model. The partially white sites indicate a partial occupancy.

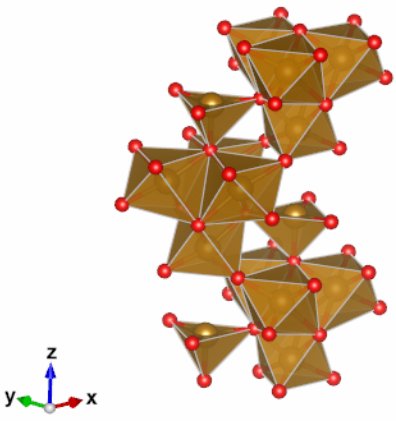

Figure 2.12: The structure of ferrihydrite according to Michel. Iron can be tetrahedrally or octahedrally coordinated.

2.5 Structural models for schwertmannite

The first model describing the structure of this recently recognized mineral was proposed by Bigham et al. (1994) [4]. On the basis of the similarities between x-ray diffraction patterns, infrared absorption data and Mossbauer spectroscopy data, the authors suggest that schwertmannite is isostructural with akaganeite, with the sulfate groups replacing the chlorides. The sulfate group shares two oxygen atoms with the octahedra assembling the akaganeite-like structure. This model was recently confirmed by a pair distribution function (PDF) analysis of synchrotron powder diffraction data [5]. The authors hypothesize however two possible arrangements for the sulfate group, one sharing two oxygens with the Fe-O network (inner sphere sulfate), and the other connected with the octahedra *via* H-bond (outer sphere sulfate). Nevertheless this model seems to be the most consistent, an electron nanodiffraction study on synthetic schwertmannite did not show evidence for an akaganeite-like structure, whereas similarities were found with 2-line ferrihydrite [42]. This relationship was recently confirmed by Hockridge et al. [43] using HRTEM analysis. The authors propose that schwertmannite has a ferrihydrite-like core with needles of goethite nucleating from the core. French et al. [44] recently reported HRTEM results in contrast with those obtained by Hockridge, using a different synthetic approach and demonstrating the elusive nature of this iron oxy-hydroxide. Schwertmannite is characterized by small aggregates of coherent structural domain of 3-4 nm forming needles, with large amounts of amorphous content [45]. The easy transformation of this phase into goethite [46] complicates the study of the structure. As further example supporting the ambiguous nature of this iron oxy-hydroxide, no unique value describing the solubility product is found, with a large range of K_{sp} reported in literature [47] and with uncertainty in the stoichiometry.

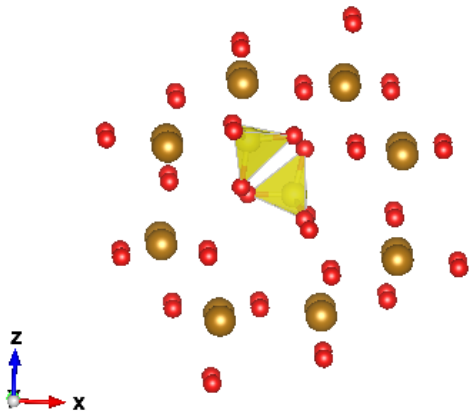

Figure 2.13: The channel of the structure of Schwertmannite proposed by Bigham [4]. Sulfate groups are hosted in two possible sites (inner and outer sphere), according to Fernandez-Martinez [5].

Chapter 3

X-ray techniques for nanoparticles

3.1 X-ray diffraction at the nanoscale

Traditionally an x-ray diffraction pattern is interpreted as a result of the interference of the x-ray radiation with an infinite set of periodically arranged atoms, called crystal. This approach relates each reflection of the pattern, from both powder or single crystal, with the distance between the parallel hkl planes in the unit cell. Using the very popular Bragg's Law [48], the distance between these planes can easily be calculated from the 2θ angle from which the reflection falls.

$$n\lambda = 2d\sin\theta \tag{3.1}$$

where λ is the wavelength of the radiation, d is the distance between hkl planes and θ is the incident angle. The intensity I of each hkl reflection is proportional to the square of the modulus of the Structure Factor F:

$$I_{hkl} \propto |F_{hkl}|^2 \tag{3.2}$$

$$F_{hkl} = \sum_{j=1}^{N} g_j f_j(\theta_{hkl}) e^{-B_j sin^2(\theta_{hkl})/\lambda^2} e^{2\pi i(hx_j+ky_j+lz_j)} \tag{3.3}$$

with the sum running over all the N atomic sites in the cell and where

- g_j is the occupancy of the atomic site j;
- f_j is the atomic form factor of the atom occupying site j;

- e $^{-B_j sin^2(\theta_{hkl})/\lambda^2}$ is the thermal factor with B_j as the atomic temperature factor of the atom occupying site j;
- x_j, y_j, z_j are the coordinates of the atom occupying site j.

The scattering vector q, which is defined as the difference between the incident and the scattered wavevectors, is sometimes used (and in some data presented in this thesis it will be used) instead of the angle theta in order to express the diffraction pattern:

$$q = \frac{4\pi \sin\theta}{\lambda} \tag{3.4}$$

In the description stated above the reflections have no width, assuming a perfect infinite crystal and, thus, an infinite and periodic scattering domain. When the size of the domain decreases, the peaks become wider. Amorphous materials, the structure of which is not periodic, represent an extreme case: the diffraction pattern shows broad bands and we cannot talk in terms of planes, symmetry or unit cell anymore. The first problem in order to study the structure of nanoparticles is technical: due to the nanometric size single crystal experiments, using x-rays are excluded and electron diffraction techniques, which are constantly improving [49; 50], must be exploited for this purpose. Anyhow, the structure can be studied also by analyzing x-ray powder diffraction data. The peak shape, the background, the size effect, the texture effect (preferred orientations affect the intensity of part of the reflections), structure strain effect and instrumental effect can be taken into account using specific corrective functions [51; 52; 53; 54]. This approach is at its most intense in the Rietveld refinement procedure [55], where the whole calculated diffraction pattern is refined minimizing the differences with the experimental pattern. Rietveld refinement will be briefly discussed in Section 3.3.

Although particle size and shape effects can be managed using specific broad functions and other effects of structural defects have been studied and well integrated into the refinement of the powder diffraction pattern [56], a question can be posed: what is the limit using this approach in order to describe a structure in which disorder also occurs? In this thesis the structures of three poorly-crystalline materials are investigated. They are neither completely amorphous nor crystalline, with diffraction patterns showing broad peaks and diffuse scattering. In the proposed models for the iron oxy-hydroxides studied in this thesis, stacking faults, amorphous content, polyphasic nature, surface disorder and other defects are hypothesized. They cannot be treated using the common strategies to identify the structure of crystalline materials. Other techniques, such as the local probe PDF, which gives information on the local structure, or the use of

the Debye Equation, in which a structure can be built without the concept of the unit cell, should be taken into account. In the PDF and the Debye Equation techniques, the entire diffraction pattern is considered. This approach is called the total scattering approach.

3.1.1 Behind the powder diffraction pattern

Before discussing the main structure analysis tools used in this thesis, we would like to dedicate a section to the information contained in the signal of the diffraction experiment. Unfortunately, different formalisms are used in different fields of the structural study of materials. A name or a symbol can have different meanings depending on the book or on the research paper. Here, we try to give a short summary of the mathematics behind x-ray diffraction (which is mostly also valid for neutron scattering). In the following, we try to unify the typical formalism of pure crystallography with that of the total scattering approach. The following formalism can be found in reference [57] The total scattering intensity registered in a diffraction experiment is composed of several parts:

$$I_{tot} = I_{coh} + I_{inc} + I_{ms} + I_{bg} \tag{3.5}$$

The incoherent scattering I_{inc} is due to the Compton Effect. Part of the x-ray beam comes out from the sample with a different wavelength, since part of the energy of the incoming photons is transferred to the recoiling electrons [58]. Multiple-scattering I_{ms} occurs when the diffracted beam coming out from a group of atoms becomes the incident beam for another group [59]. The background intensity I_{bg} arises from the scattering of everything there is in the beams path except the sample, such as the air, the optical systems, the sample holder, etc. The coherent scattering intensity I_{coh} is given by:

$$I_{coh} = sAP\frac{\partial\sigma_c}{\partial\Omega} \tag{3.6}$$

where A is the correction for the absorption contribution and depends on the geometry of the diffraction experiment, P is the correction for the Lorentz-Polarization and s is a normalization factor needed to express the *scattering cross-section* $\partial\sigma_c/\partial\Omega$ in the appropriate units of intensity per atom. The latter contains all of the structural information.

$$\frac{\partial\sigma_c}{\partial\Omega} = \sum_{i,j}^{N} f_i f_j e^{iq(r_i - r_j)} \tag{3.7}$$

where N is the total number of scatterers, f_i and f_j are the atomic form factors and r_i and r_j are the distance vectors of the atoms i and j. The scattering cross-

section can be rewritten by separating the self-scattering terms (i=j), that is the contribution to the total scattering of each atom interacting with itself, from the term that takes into account the interference between different atoms.

$$\frac{1}{N}\frac{\partial\sigma_c(q)}{\partial\Omega} = [\langle f(q)^2\rangle - \langle f(q)\rangle^2] + \langle f(q)\rangle^2 S(q) \tag{3.8}$$

where

$$\langle f(q)^2\rangle = \sum_{i=1}^{M} x_i f_i(q)^2 \tag{3.9}$$

$$\langle f(q)\rangle^2 = (\sum_{i=1}^{M} x_i f_i(q))^2 \tag{3.10}$$

with f_i the atomic form factor of the atom i^{th}, M the total number of atomic species and x_i the molar fraction of the atom i^{th}. The function *S(q)* is known as structure factor. It has, unfortunately, the same name as the F_{hkl} seen in the formulas 3.2 and 3.3. They have a strictly related meaning, but, in order to avoid confusion, we will call *S(q)* the *total scattering structure function*, since it is a continuous function of the scattered intensity and not a discrete factor that scales a Bragg peak amplitude as in the case of F_{hkl}. In the traditional crystallographic analysis, when the diffraction pattern shows well defined sharp Bragg peaks, it is common to consider all of the intensity in-between the Bragg peaks as background, thus including I_{inc}, I_{ms} and I_{bg} as a unique contribution and treating the coherent scattering intensity as a discrete function, as shown in the formulas 3.2 and 3.3. This approach is used in the Rietveld refinement, where the background is subtracted using polynomial functions that best fit the data in-between the peaks (as shown in the next section). If disorder occurs, some of the diffuse scattering could contain structural information, which could be erroneously included in the background information [60]. For this reason, when an experiment is done in order to obtain local structural information, as in the PDF method, the true background intensity has to be independently measured, by carrying out a scattering measurement without a sample, and other contributions opportunely calculated.

3.1.2 The Rietveld refinement

The Rietveld method [55] is a structure refinement procedure based on a crystalline approach. It is not a tool for *ab initio* crystal structure analysis: it requires

a starting model, that is a unit cell with cell parameters and atomic sites reasonably close to the final results and other parameters contributing to the profile of the powder diffraction pattern:

$$I(2\theta_i) = s \sum_{hkl} L(2\theta_{hkl}) P(2\theta_{hkl}) F_{hkl}^2 T_{hkl} \phi(2\theta_i - 2\theta_{hkl}) + B(2\theta_i) \tag{3.11}$$

where

- s is a scale factor
- L($2\theta_{hkl}$) is the Lorentz correction;
- P($2\theta_{hkl}$) is the Polarization correction;
- F_{hkl} is the structure factor (see formula 3.3);
- T_{hkl} is the preferred orientation correction;
- $\phi(2\theta_i - 2\theta_{hkl})$ is the peak shape function;
- B ($2\theta_i$) is the background correction function;

A powder diffraction pattern is calculated and compared with the experimental data. The difference between them is improved by refining the parameters on which the calculated pattern depends and minimizing the sum of the square of the residuals:

$$S = \sum_i w_i (I_{calc}(2\theta_i) - I_{exp}(2\theta_i))^2 \tag{3.12}$$

As said before, the starting parameters must be reasonably close to the final values. Moreover, the sequence into which the different parameters are being refined needs to be carefully studied.

3.1.3 The Debye Equation

The Debye Scattering Equation is a continuous function in the reciprocal q space describing the total coherent scattering cross-section produced by a multiple-particle system, in which all the possible orientations are equally represented [61].

$$\frac{\partial \sigma_c(q)}{\partial \Omega} = \sum_{i=1}^{N} \sum_{j=1}^{N} f_i(q) f_j(q) \frac{\sin(q r_{ij})}{q r_{ij}} \tag{3.13}$$

where f_i and f_j are the scattering factors of the i and j atoms set at the distance r_{ij}. It implies a bottom-up approach starting from the atomic coordinates from the scattering body. Interestingly, the Debye Scattering Equation does not rely on the concept of symmetry, although it helps to simplify calculation when present. This feature can be exploited to obtain a better description of defects, disorder, surface effects, dislocations or stacking faults [62; 63; 64; 65]. For this reason, nanostructured and poorly crystalline samples are ideal candidates to be studied with this method. The use of this equation is limited to its computational complexity, with computing time strongly depending on the number of atoms N. Although this formula has been known since 1915, its first application to obtain information on particle size and structure was performed in 1941 [66] on spherical small FCC Cu clusters. In recent years, due to advances in computer performance and in several computational strategies optimizing its calculation, the Debye Scattering Equation has been applied to finite size crystals, such as nanocrystalline particles [67; 68; 69]. In particular, the availability of faster computation due to the use of graphics processing units for general purpose (GP-GPU) has allowed one to extend the use of this equation [70; 71].

3.1.4 The PDF analysis

The Pair Distribution Function (PDF) g(r) is a function describing the interatomic positional correlations in a structure:

$$g(r) = \frac{1}{4\pi N r^2 \rho_0} \sum_i \sum_j \delta(r - r_{ij}) \tag{3.14}$$

where ρ_0 is the number density of the atoms in the system of N atoms. The δ is a Dirac Delta function of the distances r-r_{ij}. The PDF function gives the probability of finding two atoms separated by the distance r. This function is related to the experimental diffraction pattern by a Fourier Transform:

$$G(r) = 4\pi r \rho_0 [g(r) - 1] = \frac{2}{\pi} \int_0^\infty q[S(q) - 1] \sin(qr) dq \tag{3.15}$$

where *G(r)* is called *Reduced Pair Distribution Function* and *S(q)* is the total scattering structure function introduced in Section 3.1.1. The inverse Fourier Transform yields the *S(q)* in terms of *G(r)*.

$$S(q) = 1 + \frac{1}{q} \int_0^\infty G(r) \sin(qr) dr \tag{3.16}$$

The PDF function provides substantial information about the distances between pairs of atoms and their coordination numbers. For this reason, it is a

useful probe in order to understand aspects concerning the local structure that cannot be revealed through the classic crystallographic methods [ref fullerene, ref alloys, underneath the bragg peaks]. The integration in 3.15 is from q = 0 to q = ∞ Å^{-1}. This range is obviously only ideal, since q = ∞ can be obtained only if the wavelength is equal to zero. In any case, the smaller the wavelength of the beam, the more detailed the information from the PDF. For this reason, total scattering experiments usually take place in synchrotron facilities, where radiation with wavelengths abundantly smaller than 1 Å is available. Laboratory diffractometers should have sources different from the classic Cu or Co (experiments are commonly performed using Mo or Ag tubes). Some Rietveld-like programs are available for the refinement of structures in the real space, so as to minimize the difference between the experimental PDF and the calculated PDF of a starting model. Refinable structural parameters (cell parameters, atomic positions, etc...) are changed in order to improve the agreement between the two curves [72; 73].

3.2 Extended X-ray Absorption Fine Structure

When an electron is ejected from an atom as a result of an opportune energy contribution, its wavefunction interacts with the wavefunction of the neighboring atoms. As a consequence, the x-ray absorption coefficient shows oscillations as a function of energy just above the absorption edge. In some cases, oscillations can be observed to an extent of 1000 eV. The oscillating function describing this behavior is called EXAFS (Extended X-ray Absorption Fine Structure) and it is defined as the normalized modulation of the absorbance of the energy:

$$\chi(E) = \frac{\mu(E) - \mu_0(E)}{\mu_0(E)} \tag{3.17}$$

$\mu(E)$ is the measured absorbance given by the Lambert-Beer law [74; 75]:

$$\ln(I/I_0) = -\mu x \tag{3.18}$$

where I is the measured intensity of the incident beam after the passage through the material of thickness x and I_0 is the intensity of the incident beam at the source. μ_0 is the atomic background absorption. It is calculated fitting the function $\chi(E)$ far from the edge where the oscillations are reduced to zero. It is common to express the EXAFS signal as a function of the momentum k instead of the energy:

$$k = \sqrt{m(E - E_0)}/\hbar \tag{3.19}$$

where E_0 is the energy of the absorption edge. The EXAFS signal can be interpreted in terms of the local structure around the atom responsible for the emission of the photoelectron [76; 77]:

$$\chi(k) = \sum_j \frac{N_j S_0^2(k)}{k r_j^2} |f_j^{eff}(k)| e^{-2k^2\sigma_j^2} e^{-2r_j/\Lambda(k)} \sin(2kr_j + \phi_j(k)) \tag{3.20}$$

The function is obtained by summing the contribution coming from each path j of N_j atoms at a distance r_j from the central atom. $S_0^2(k)$ is the amplitude reduction factor, $f_j^{eff}(k)$ is the effective amplitude function for each path, σ_j^2 is the Debye-Waller parameter, $\Lambda(k)$ is the photoelectron mean free path, and ϕ_j is the phase shift due to the Coulomb potentials of the central atom and the atoms of the j^{th} shell. The Fourier Transform of the $\chi(k)$ gives a radial distribution function in which the local structure around the absorbing atom is clearly visible in the real space. For this reason, the EXAFS technique is usually associated with the PDF, although, unlike the *g(r)* obtained from X-ray data, the *g(r)* from EXAFS data only regards the pairs in which the absorbing atom is present. Programs able to treat EXAFS data are available [78]. A fitting procedure can be performed using both ab-initio calculated parameters (the values of $f_j^{eff}(k)$, $\Lambda(k)$ and ϕ_j for the possible scattering paths) and refinable parameters as the distances r_j or the coordination numbers N_j.

Chapter 4

DMC. A program for the refinement of nanoparticles

4.1 Overview

In order to study the structure of the materials investigated in this PhD thesis, the computer program DMC (Debye Monte Carlo) for the refinement of nanoparticles was built. In DMC a starting model is refined by applying an algorithm similar to Reverse Monte Carlo (RMC) [79]. As commonly done in the RMC approach, which will be discussed in detail in the next section, small atomic displacements are randomly generated on a model structure simulating the thermal and the surface relaxation disorders. The displacements are accepted or rejected on the basis of the agreement between calculated and experimental XRPD patterns. In addition, the PDF function can be calculated by applying the Fourier Transform to the calculated and experimental XRPD patterns. In this instance, the displacements are accepted or rejected on the basis of the agreement between both XRPD patterns and PDFs. Contrary to the RMC algorithm, where first the PDF function is calculated and then, if necessary, a Fourier Transform is applied in order to minimize the differences also in the reciprocal space, in DMC the coordinates of the atoms in the model are used to calculate the diffraction pattern and then, if necessary, the PDF can be obtained by applying a Fourier Transform to the data in the reciprocal space. Indeed, a peculiar feature of this program is that the starting model is a set of atoms placed in the space describing one or more whole particles and that the XRPD pattern is calculated using the Debye Scattering Equation. This approach overcomes the problems which arise due to the use of the traditional crystallographic methods in the study of poorly nanocrystalline materials, as discussed in Chapter 3. To speed up the computing time, the XRPD pattern is calculated by using graphics processing units (GPUs).

This innovative approach opens up the possibility of using an RMC-like approach to successfully model particles made out of several thousand of atoms in a very reasonable computing time. The program is written in C/C++/CUDA [80].

4.2 The Reverse Monte Carlo method

The Reverse Monte Carlo is a modelling method for atomic structures [79; 81; 82]. A starting model is used to calculate a function related to its structure which is compared with the corresponding experimental data. The difference between the two functions is given by the agreement parameter χ^2:

$$\chi^2 = \frac{1}{\sigma^2} \sum_{i=1}^{N_P} w_i (Y_i^{obs} - Y_i^{calc})^2 \tag{4.1}$$

where Y_i^{obs} and Y_i^{calc} are the values of the experimental and calculated function in the i^{th} point respectively; N_P is the number of data points; w_i is a weight parameter and σ is called the temperature parameter. An iterative minimization procedure of the agreement parameter is run by moving the atoms of the starting model from their original positions. After each move the Y_i^{calc} is recalculated and a new agreement parameter $\chi^{2\prime}$ is provided. The move is accepted according to the criterion:

$$rnd[0,1] \leq e^{-(\chi^{2\prime} - \chi^2)/2} \tag{4.2}$$

where $rnd[0,1]$ is a random real number between 0 and 1. If the new agreement parameter is less than the old agreement parameter the move is accepted because the right member of the formula 4.2 is greater than 1. If not, the move could be accepted in any event; the smaller the difference between $\chi^{2\prime}$ and χ^2, the higher the probability. The temperature parameter σ in 4.1 can be tuned to allow a smaller or a greater number of moves in order to avoid local minimum traps. The recursive procedure continues until convergence. The structural functions involved in the RMC can be PDFs and diffraction patterns, both for x-rays and neutrons, EXAFS, NMR and every function that can be calculated by using atomic coordinates [83; 84]. The RMC method is a fitting procedure, so the consistency of the resulting model is not assured. The procedure should include constraint with respect to the distances between atoms, density and other physical parameters. In any case the tridimensional structure carried out by the algorithm, realistic or not, is not unique: other models can be consistent with the experimental data. Statistically, RMC gives the most disordered model, which is that with the highest configurational entropy.

4.3 The DMC program

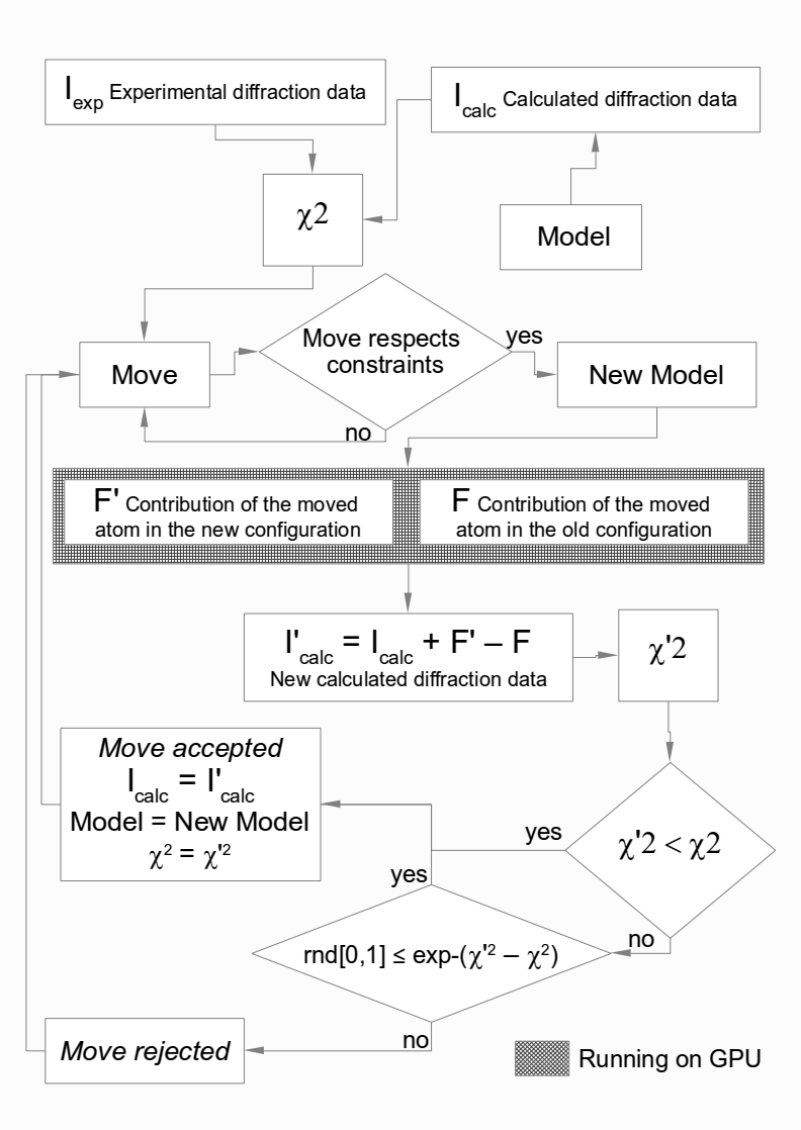

Figure 4.1: The scheme of the program DMC.

The diagram of the code used for the RMC refinement using Debye Scattering Equation on GPUs is shown in Fig 4.1. Data inputs required include:

- the experimental diffraction data;
- the starting model (an atomic coordinates file);

- the calculated diffraction data of the starting model;
- the settings file containing options for the refinement.

The starting model can be described using a classic absolute coordinates file, including atomic number and x, y, z coordinates for each atom. The latter file contains an additional column where a Boolean variable (1 or 0) specifies whether the corresponding atom is allowed to be moved or not. Experimental data can be from the X-ray tube or from synchrotron sources. A version able to manage neutron diffraction data will be available soon. Different corrections can be taken into account depending on the experimental settings and some of them can be provided by the program. The diffraction pattern of the starting model must be calculated using Debye Scattering Equation. In the present version, the program does not calculate the diffraction pattern from the starting model, so it must be calculated using an external program available for this purpose, such as Debyer [85]. The core of the code is the basic RMC method. In particular, the difference between the experimental and the calculated data is minimized using the agreement factor χ^2. The χ^2 of formula 4.1 is provided by comparing the experimental and calculated XRPD patterns and their Fourier Transforms (PDF functions):

$$\chi^2_{tot} = k_{XRPD}\chi^2_{XRPD} + k_{PDF}\chi^2_{PDF} \tag{4.3}$$

where k_{XRPD} and k_{PDF} are arbitrary weights and the χ^2_{XRPD} and χ^2_{PDF} are obtained using the formula 4.1. Weights can be chosen in order to balance the fit in a way the operator considers preferable. To improve the agreement close to the maximum, the parameter w_i in the formula 4.1 is equal to the square of Y_i^{obs}, that is the square of the experimental diffraction pattern in the case of χ^2_{XRPD} and the square of the experimental PDF in the case of χ^2_{PDF}. The reader should note that since the calculated pattern is obtained using the Debye Scattering Equation, it actually represents coherent scattering with no absorption and polarization contribution (that is the so-called cross-section scattering, see Section 3.1.2). The experimental data must be therefore adequately corrected. The program in its latest version is able to calculate and correct the following:

- Incoherent scattering contribution;
- Lorentz-Polarization contribution;
- Thermal contribution, calculated as shown in formula 3.3 with only one possible average value for the parameter B;
- Scale factor, calculated using linear fitting (provided by GSL libraries [86; 87]) between calculated pattern and experimental data after the corrections.

A generic background can be also calculated using a 3^{rd} degree polynomial function. In this case the scale factor is simultaneously calculated and linear fitting using GSL libraries provides best scale factor and polynomial coefficient values. An RMC cycle corresponds to the following events: one atom is randomly chosen from the list of those that can be moved and its coordinates are randomly modified within a maximum displacement value; furthermore a constraint over the minimum distance allowed between neighboring atoms is imposed. A new diffraction pattern and their Fourier Transform are then calculated from the new atoms configuration as shown in the previous section and compared with the experimental data, providing the new $\chi^{2\prime}$ which is accepted according to formula 4.2. The maximum and minimum distances between pairs of atoms, the maximum displacement value and the temperature factor σ can be tuned in the settings file.

4.4 Calculating the diffraction pattern with GPUs

During recent years, especially thanks to the video-games industry, graphics processor units (GPUs) have been rapidly improving in terms of performance. This potentiality corresponds to a great opportunity also for more general purposes, which arent necessarily applications related to graphics computing. Computational scientists have started to use the GPUs to run heavy codes with great results in terms of time saving [88; 89; 90]. This advantage is due to the structure of the graphics processor. In Fig 4.2 a comparison between the structure of the Central Processing Unit (CPU) and the GPU is shown. A single CPU features a limited number of subunits, called cores, whereas a GPU can have thousands of cores.

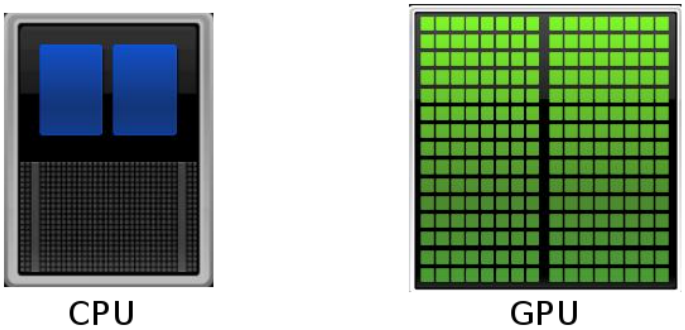

Figure 4.2: The difference between CPU and GPU.

A single core is an elaborative unit, which has its own arithmetic logic unit

(ALU) and where a logic or arithmetic operation occurs. CPUs and GPUs were designed for different purposes. The cores can work simultaneously in order to run arithmetical and logical operations. A CPU was conceived primarily as an executive unit, making logic operations (if this, do that, else do something else) above all. Logic operations cannot be executed simultaneously and, for this reason, CPUs have few cores, however each core is capable of extremely high performance. A GPU is designed to run the same instruction to large groups of pixels on the screen. This work can be performed at the same time by different units, and for this purpose a large number of cores with their own ALUs are available. From an arithmetical computing standpoint, although a single CPU's core is much faster than a single GPU's core when calculating a set of operations, if these operations can be executed simultaneously, a multiple-core GPU can be tremendously fast. A code running on different cores working simultaneously is called *parallelized code* and simultaneous operations can be divided into *streams*. The necessary conditions in order to run parallel instructions are that the result of each instruction does not depend on the result of the others. This paradigm is illustrated in Fig 4.3, using an analogy drawn on the popular American TV series *The Simpsons*. The prodigious Lisa represents a powerful single-core CPU, whereas a group of trained monkeys represents the multi-core GPU. Depending on the instructions, one can be faster than the other. The Debye Scattering equation can be easily parallelized. The result of each contribution of the double sum in formula 3.13 does not depend on the other contributions.

Figure 4.3: The analogies between Lisa Simpson and the CPU and between a group of monkeys and the GPU

Gelisio and others [70] first used a GPU in the calculation of the Debye Scattering Equation. They calculated the XRPD pattern of models different in size both on a GPU and a CPU and they presented the results in terms of performances. In the specific case of the program DMC, after each move the diffraction

pattern needs to be recalculated. This would in principle slow down the computing time tremendously; however the calculation can be simplified, because the change in the scattering intensity depends only on the distances involving the moved atom k. The new scattering intensity I'(q) is then calculated:

$$I'(q) = I(q) - 2\sum_j f_k f_j \frac{\sin(qr_{kj})}{qr_{kj}} + 2\sum_j f_k f_j \frac{\sin(qr'_{kj})}{qr'_{kj}} \tag{4.4}$$

where r_{kj} and r'_{kj} are the distances between atom k and j before and after the move, respectively. Each contribution is calculated in a single stream, as illustrated in Fig 4.4. The product f_k f_j is calculated before the RMC iteration starts and it is simply loaded by the GPU. In the work shown in this thesis the code runs on an Nvidia GeForce gtx 690 GPU [91] and the CUDA language is used in order to manage the graphics card. The Nvidia GeForce gtx 690 contains two separate GPUs, since new and old contributions are calculated simultaneously, CPU parallelization is introduced into the code: one CPU core calls the first GPU, another CPU core calls the second GPU. The OpenMP Application programming interface is used for the CPU parallelized code [92]. In Appendix A the code of the routine for the calculation of the diffraction pattern is reported.

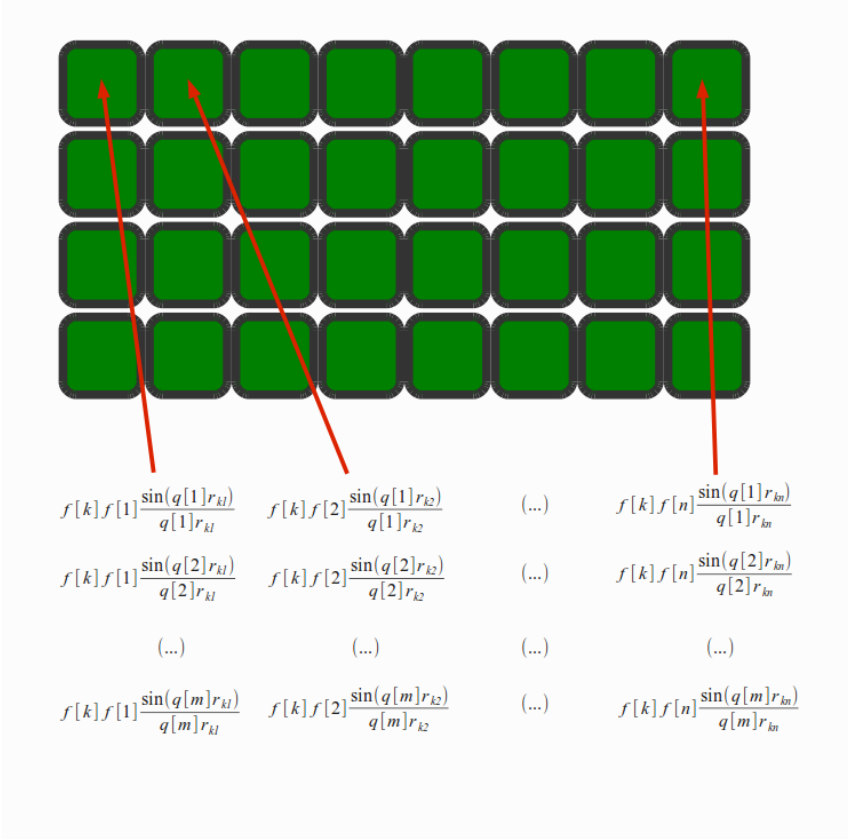

Figure 4.4: The calculation of the Debye Equation on GPUs in the program DMC. Each core of the GPU calculates a single contribution of the summation in formula 4.4.

Chapter 5

Feroxyhyte structural analysis

5.1 Overview

Because of the poor crystallinity, a reasonable model for feroxyhyte can only be determined putting together different information. Not only the proposed unit cell and atom coordinates should be able to fit the experimental XRPD pattern, but the model should be also consistent with observations and experimental data from other techniques, e.g. Extended X-ray Absorption Spectroscopy (EXAFS). Moreover, the experimental peak broadening and the low angle features should be reproduced by introducing additional effects such as average size and shape distribution of the CSDs, occurrence of stacking faults, strain and stress within the CSDs, uncertainty in the composition, and presence of additional phases. These issues have been addressed by Drits et al. [3], who proposed a crystalline model for δ-FeOOH with definite atom coordinates and site occupancy factors (SOFs). In this crystalline structure, which is an elaboration of the original model by Francombe et al. [93] and Patrat et al. [24], the smallest structural unit is described as trigonal, with a network consisting of anionic ABAB hexagonal layers and iron atoms set in the octahedral sites. Their final result, which includes some modifying effects to improve the agreement with the experimental XRPD pattern, is an excellent reproduction of the experimental XRPD pattern (see Figure 7 of reference [3]). From this point of view, it does not seem necessary to revise the above mentioned model, which however as a major drawback does not share the common features of other Fe iron oxyhydroxides. It should be pointed out that the smallest structural unit of the Drits model depicts a mean structure, as the presence of Fe atoms with occupancies of 1/4 would implies the definition of a larger cell; besides, O atoms from O^{2-} and OH^{-} are set in equivalent positions, so that they come out crystallographically undistinguishable. Basically, the entire structure appears quite similar to that of hematite, α-Fe_2O_3 [17], in which the coordination octahedra of iron atoms are connected by corners, edges

and faces, with a ternary axis along the c-direction. On the other hand, the networks of goethite [20], lepidocrocite [94] and akaganeite [22] do not present the ternary axis and any face sharing of octahedra. Besides, the face sharing occurrence predicted by the Drits model is in contrast with magnetic measurement results [23]. In Section 5.3, we will show an interesting connection between the structure of goethite and the structure of feroxyhyte and we will hypothesize a novel interpretation of the mean model represented by the Drits unit cell. This connection is verified by EXAFS and Reverse Monte Carlo analysis, the results of which are shown and discussed in Section 5.4. We first tested and compared the structure networks of goethite and hematite as starting structure data in the fitting of EXAFS data of feroxyhyte. Afterwards, we have addressed the investigation of the local structure of feroxyhyte by applying the Reverse Monte Carlo algorithm in the reciprocal space and by using a starting model based on some relevant features common to both the Drits model and to the goethite network shown in Section 5.3. The DMC program is used but, since the experimental pattern is obtained using Cu-Kα source diffractometer with a low resolution in q, the RMC fitting was performed only in the reciprocal space.

5.2 Synthesys and characterization of feroxyhyte

Feroxyhyte was prepared according to Carlson and Schwertmann [12] by adding dropwise a 5M KOH solution to 100 mL of a 0.1 M solution of $FeCl_2 \cdot 4H_2O$, under constant stirring, until pH = 8 was reached; then rapidly 15 mL of H_2O_2 (30%) were added. To improve flocculation, 5M KOH solution was added again dropwise until pH = 8. The product was centrifuged, washed and dried in an oven at 45°C for 18 h, and characterized by both scanning and transmission electron microscopy and x-ray powder diffraction. Transmission electron microscopy (TEM) images were collected using a Hitachi 7000 microscope operating at 125 kV, by depositing a drop of dispersion of feroxyhyte into ethanol on a carbon coated copper grid. Scanning Electron Microscopy (SEM) was performed on a Hitachi S4000 equipped with a field emission gun and operating at 20 kV. Prior to observations the powder was coated with platinum (2 nm) by an Emitech K575 turbo sputtering apparatus. XRPD data were collected on a PANalytical Empyrean diffractometer using a Cu-Kα tube operating at 40 kV and 40 mA, coupled with a graphite monochromator on the diffracted beam and a X-Celerator linear detector, scanning over an angular range from 10°(2θ) to 110°(2θ) with a step size of 0.05°(2θ) and a total acquisition time of 38 h. A conventional sample holder and fixed slits were used to ensure that a constant volume of the sample was irradiated during the 2θ scanning. The sample holder was submitted to a spinning speed of 1 Hz in order to reduce any preferred orientation effect. EXAFS

data was collected at the Elettra Synchrotron 11.1 (XAFS) beamline in Trieste at room temperature using a Si (111) monochromator in transmission mode at the Fe K-edge (7112 eV). Samples were prepared by pressing the powders diluted in polyvinylpyrrolidone (PVP) into pellets. Experimental XRPD pattern is shown in Figure 5.1 and it displays the characteristic four peaks at $2\theta = 35°$, 40°, 54° and 63°; Figure 5.2 reports representative SEM and TEM images of the synthesized feroxyhyte. These data clearly indicate the occurrence of disc-shape particles, as suggested by previous observations [3] which are quite polydisperse in size.

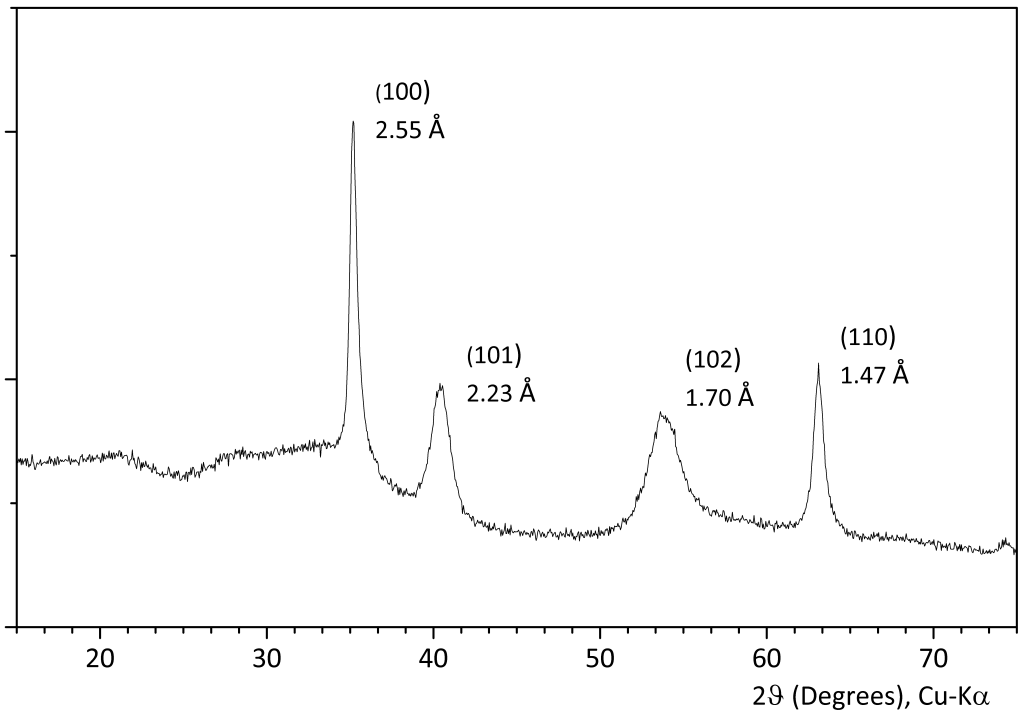

Figure 5.1: Experimental XRPD pattern of feroxyhyte.

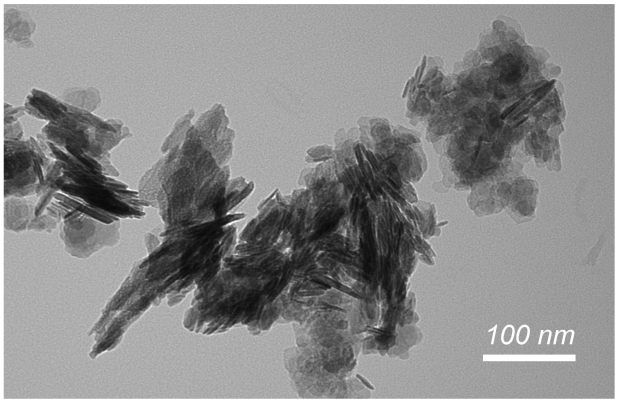

(a)

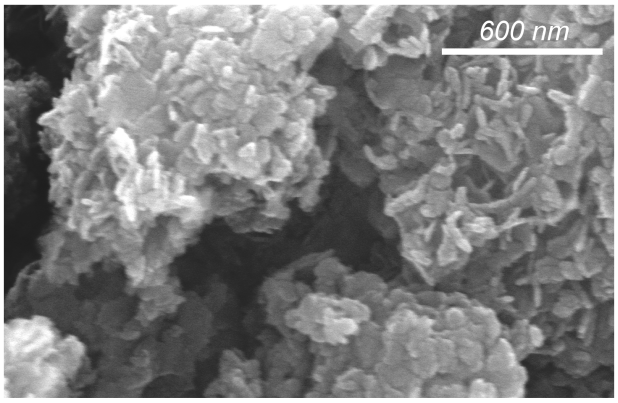

(b)

Figure 5.2: TEM (a) and SEM (b) representative images of feroxyhyte particles, showing the disc-shape particles polydisperse in size.

5.3 Goethite and feroxyhyte relationship: a novel interpretation of the mean structure of feroxyhyte

5.3.1 Novel feroxyhyte structural model interpretation

In our attempt to find a possible structural reference for a novel description of the structure of feroxyhyte we left out poorly crystalline materials such as ferrihydrites, and instead we considered the known structures of common iron oxy-hydroxides such as goethite, lepidocrocite and akaganeite. Each of these materials has distinctive unit cell symmetry, density and anionic distribution, hence a definite and a distinct XRPD pattern, but they all present many structural analogies, which reasonably should be shared by any other Fe oxy-hydroxide structure. In particular, the Fe-O^{2-} distances are 0.10-0.15 Å shorter than Fe-OH^{-} distances; Fe^{3+} and O^{2-} form -Fe-O-Fe-O- chains (in akaganeite they define eight-atom rings) connected by OH^{-} bridges; hence the O^{2-} species is crystallochemically different from the OH^{-} one. In all of these structures the atomic unit depicted in Figure 5.3 is present, which can be geometrically viewed as two edge-sharing octahedra with the Fe atoms in the cavities and O^{2-} in the vertices connecting other similar units. However, the Fe-O-Fe angles are different in the structures of the three above mentioned oxy-hydroxides, thus giving rise to network connectivity with different unit cells, hence different densities. In fact, the volumes per FeOOH unit are equal to 34.7 $Å^3$ in goethite, 37.3 $Å^3$ in lepidocrocite and 42.3 $Å^3$ in akaganite; another form of FeOOH obtained under high pressure has a unit volume of 32.7 $Å^3$ [1].

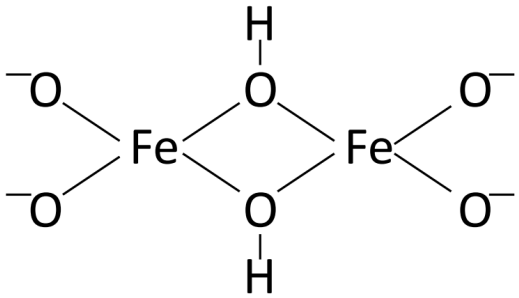

Figure 5.3: Two edge sharing octahedra: this atomic unit is found in the well characterized Fe oxy-hydroxides (goethite, lepidocrocite and akaganite).

Assuming that the local structures of feroxyhyte contain the same structural elements common to other oxy-hydroxides, we now need to determine which of the

goethite, lepidocrocite and akaganeite structures is the best reference to describe the same mean structure proposed by Drits et al. Two useful indications for the choice arise from the observations that the feroxyhyte unit cell volume is about 34 Å^3 and that the anionic sheet sequence in feroxyhyte is ABAB. These characteristics are only found in goethite, which was therefore chosen as reference network for the possible local structures present in feroxyhyte. Comparing the unit cells of goethite (cell G in Figure 5.4, a = 9.95 Å, b = 3.01 Å, c = 4.62 Å, V = 138 Å^3, Z = 4, space group Pnma) with that of the Drits model of feroxyhyte (Table 2.2, a = b = 2.947 Å, c = 4.56 Å, γ = 120°, V = 34.3 Å^3, Z = 1, space group P-3m1) it can be observed that they possess similar values for their b and c axes, and that the ratio $a_{goethite}/a_{feroxyhyte} \simeq 4\sin(120°)$. Sin(120°) is typical of geometrical transformations between orthorhombic cells and their corresponding trigonal cells, suggesting how the Drits feroxyhyte trigonal cell can be connected to the goethite orthorhombic cell, as described in the following.

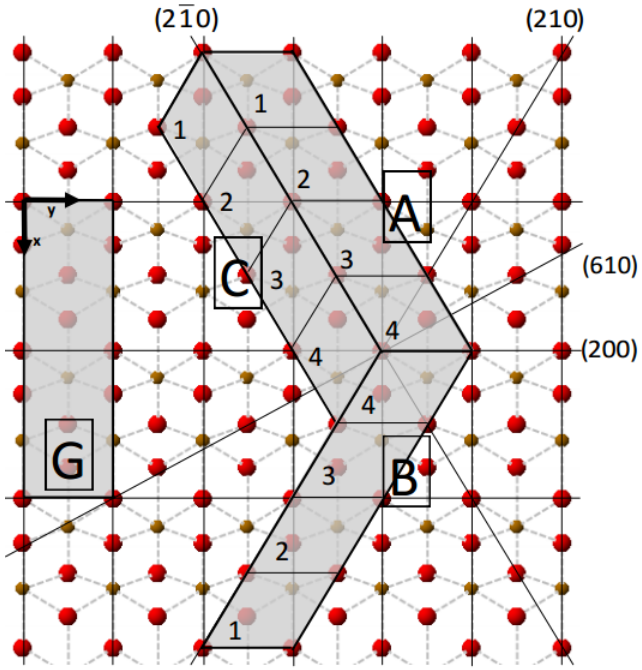

Figure 5.4: Geometrical connection between the orthorhombic cell of goethite and the trigonal cell of the feroxyhyte Drits model (Drits et al. 1993 [3]). In the xy-projection of the goethite network (unit cell G) 12 different subunits with feroxyhyte-like structure can be detected: A1-A4 , B1-B4 , C1-C4. Units A , B and C are delimited by the (200), (210) and (2-10) planes, which are the twinning planes of twinned goethite. Fe: red circles, O: brown circles.

		Drits model, 1993 a=2.947Å, b=2.947Å, c=4.56Å γ=120°				Present work a=2.941Å, b=2.941Å, c=4.62Å γ=120°			
Atom	Site	x	y	z	SOF	x	y	z	SOF
Fe1	1a	2/3	1/3	0.065	0.25	2/3	1/3	0.045	0.25
Fe2	1a	2/3	1/3	0.435	0.25	2/3	1/3	0.455	0.25
Fe3	1a	2/3	1/3	0.565	0.25	2/3	1/3	0.545	0.25
Fe4	1a	2/3	1/3	0.935	0.25	2/3	1/3	0.955	0.25
O1	1a	0	0	0.250	1	0	0	0.250	1
O2	1a	1/3	2/3	0.750	1	1/3	2/3	0.750	1

Table 5.1: Comparison of feroxyhyte cell parameters and atom positions for the Drits model and the present interpretation. The Drits model original coordinates (reported in Table 2.2) have been conveniently redefined for direct comparison.

The periodic repetition of the goethite structure can be alternatively described by choosing a different unit cell. If we look at the xy plane, two periodic monoclinic units (A and B in Figure 5.4) appear especially interesting as alternatives to the commonly accepted cell (G in Figure 5.4). A and B have the same unit cell parameters: a = 3.01 Å, b = 11.63 Å, c = 4.62 Å, γ=121.17. As shown in Figure 5.4, each of these cells can be divided into 4 subunits (A1-A4, B1-B4). It is interesting to note that each subunit has the same atom content, (FeOOH), and that the associated cell parameters are very close to those proposed by Drits. In each of these subunits the O ions have coordinates very close to those of the Drits model and the coordinates of the 4 Fe ions in Drits model find a corresponding Fe ion in each of the 4 subunit with similar coordinates. There is another unit, C, that is particularly interesting, whose dimensions are: a = 2.91 Å, b = 11.63 Å, c = 4.62 Å, γ = 117.66°. Even if it is not periodic, when it is divided into 4 subunits (C1-C4), these subunits are very similar to those found in A and B. Consequently, it seems reasonable to propose that these subunits could represent different local arrangements of atoms able to describe the mean model of feroxyhite, alternatively to the approach followed by Drits et al. To verify this hypothesis, an averaging process was carried out in the following way: first averaging the 4 subunits present in units A, B, and C, three average cells were obtained, Am, Bm, Cm. The atomic coordinates of Fe and of O (from O^{2-} and OH^{-}) were averaged on the xy-plane, whereas the z coordinates were kept to their original values, thus maintaining a clear link with the starting goethite structure. An average of the atomic coordinates of Fe and of O on the xy-plane was then taken of these three average cells, giving rise to a final rhombohedral (trigonal) unit cell, with the following cell parameters: a_{mean} = (3.01+2.91+2.91) Å/3 = 2.94 Å;

b_{mean} = (2.91+3.01+2.91) Å/3 = 2.94 Å; γ_{mean} = (121.17+121.17+117.66)°/3 = 120°. These values practically coincide with the corresponding parameters of the Drits cell for feroxyhyte; as shown in Table 5.1, where the final average cell obtained in this work is compared with the cell proposed by Drits, specifying all the atom coordinates. Figure 5.5 showing the superposition in the xy-plane of the 12 different subunits is especially indicative of the atomic coordinates involved in the averaging process.

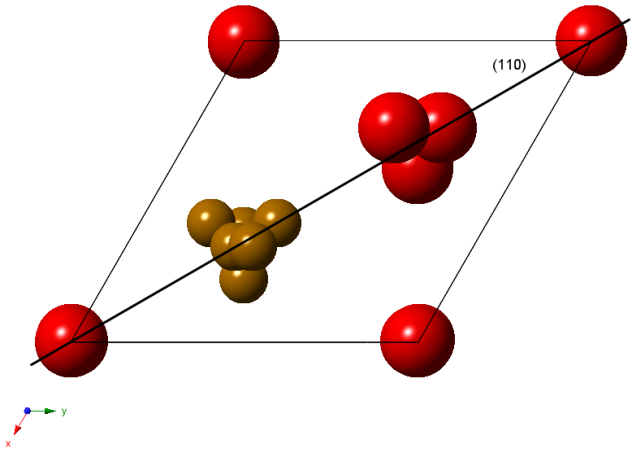

Figure 5.5: Overlapping in the xy-plane of the 12 different subunits shown in Figure 5.4. Fe: brown circles, O: red circles.

5.3.2 Discussion

A comparison of the XRPD patterns of this mean cell and of that of Drits feroxyhyte is reported in Figure 5.6, together with the experimental XRPD pattern. The two calculated patterns show strong similarities and they are both in agreement with the experimental XRPD pattern, taking into account that effects leading to line broadening and to the low angle diffuse scattering halo present were not considered here. In particular, it is found that the four characteristic Bragg reflections are set at almost the same angular values and have similar relative intensities.

From the goethite network 12 subunits have been singled out (4 subunits for each of the A,B,C units), from which a mean cell has been calculated possessing shape, size, content and positions of atomic species very close to those of the feroxyhyte mean model given by Drits et al. This similarity is reflected in the two calculated XRPD patterns displayed in Figure 5.6, supporting the fact that the local arrangements of the 12 subunits obtained from goethite can effectively

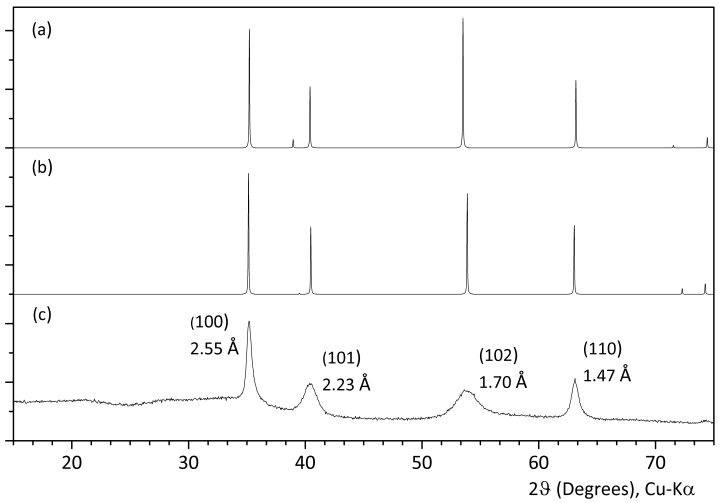

Figure 5.6: a) Calculated feroxyhyte XRPD pattern for the unit cell shown in Table 5.1 (present work); b) calculated feroxyhyte XRPD pattern for the Drits unit cell; c) experimental pattern

represent the commonly accepted mean structure of feroxyhyte. For a better understanding of the connection between the local structures of goethite and the mean model of feroxyhyte one may follow how the starting complex XRPD pattern of goethite can be simplified to the final simple 4-line pattern of Drits feroxyhyte through the transformation given above. A look at the XRPD patterns of units A and B is not particularly interesting. In fact, A and B are periodic units, hence their XRPD patterns are those of goethite (Figure 5.7a). C is not periodic, hence its XRPD pattern is different, although it looks similar to goethite. Conversely, a clear simplification with respect to the goethite is displayed by the 12 patterns of the subunits A1-A4, B1-B4 and C1-C4. They all look almost indistinguishable as for line positions, and only show small differences in line intensities. The calculated XRPD of one of these units is shown in Figure 5.7b.

A further simplification of the XRPD patterns is shown by the mean structures A_m, B_m, C_m obtained averaging the structures of the 4 different subunits within units A, B, C. These XRPD patterns are almost coincident; and in Figure 5.7 A_m is shown as an example. With respect to the goethite pattern the lines with $2\theta < 34°$, that is, (200), (101), (201) and (301), are missing, as well as the strong lines (111) and (511) and most of the fainter lines, while the remaining lines are modified in their intensity ratios. The reason of this simplification lies in the greater symmetry of the mean units A_m, B_m and C_m. It is interesting to note that the stronger eight lines of Figure 5.7 form four pairs, each of them

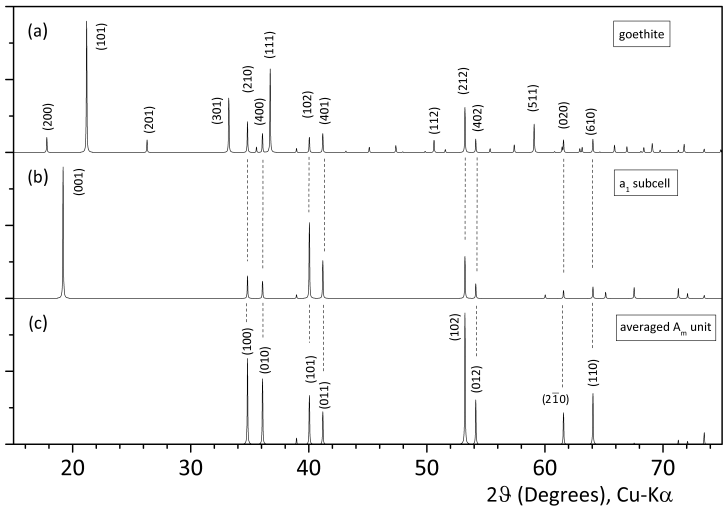

Figure 5.7: Progressive simplification of the XRPD pattern from goethite to the mean structure A_m. a) XRPD pattern of goethite, b) XRPD pattern of a1 subcell and c) XRPD pattern of averaged Am unit. The peak (001) in the intermediate pattern is due to the presence of the Fe atom with SOF=1.

appearing as the splitting of one of the four lines of Drits model (Figure 5.6). The splitting phenomenon is due to cell parameters, a $\neq$ b, $\gamma \neq 120°$. Finally, the XRPD pattern of the final unit cell is calculated (Figure 5.6a). This cell is obtained averaging the networks of the three mean units A_m, B_m and C_m, that is, the networks of the 12 different subunits (Figure 5.4). As already reported above, the cell parameters of the final unit cell practically coincide with the corresponding parameters of the Drits cell and, consequently, the four pairs of reflections in the XRPD (Figure 5.7c) pattern appear as four single reflections practically coincident with those appearing in the XRPD pattern of the Drits model (see Figure 5.6). The small differences still present in the positions of the reflections can be ascribed to the small differences in cell parameters, in particular in the c parameter (4.62 Å against 4.56 Å). A support to the proposed approach to describe the local structure of feroxyhyte may be found in the well documented ability of goethite to form twinned crystals growing along the planes (210) and (200), with a boundary along the (2-10) plane [95; 96; 97**?**] (see in particular Figure 4.10 of reference [1]). These planes are the same which separate units A, B and C in Figure 5.4.

It is worth noting that the generation of the mean model of feroxyhyte starting from local structures of goethite greatly affects peak intensities in the XRPD patterns (Figure 5.7). In particular, the intensity of the (610) reflection of goethite

at d = 1.45 Å is much lower than that of the corresponding reflection (110) of feroxyhyte at d = 1.47 Å (ratio about 1/4). A comparison of the relative planes shows in fact that the (610) plane of goethite (Figure 5.4) is less crowded than the (110) plane of feroxyhyte (Figure 5.5). Similar effects can be observed in the XRPD pattern of poorly crystalline goethite obtained by oxidation of $FeCl_2$ (ref [98], p. 79). Its XRPD pattern compared with that of well-crystallized goethite shows enlargements and intensity variations of peaks. Although these modifications are not easy to interpret, it is meaningful that the peaks typical of feroxyhyte tend to increase in the XRPD pattern of poorly crystalline goethite. An additional evidence of the similarity between the structure of feroxyhyte and goethite which is at the base of the novel interpretation proposed in our work can be inferred by the resemblance of the EXAFS data of feroxyhyte and goethite published by Manceau et al. [30].

5.4 Feroxyhyte structure study using EXAFS and reciprocal space RMC

5.4.1 EXAFS analysis using goethite and hematite paths

The Athena and Artemis programs are used for data analysis [78]. Experimental data treatment (normalization and background subtraction) is performed using the program Athena, while fitting is carried out using the program Artemis. Normalized and corrected EXAFS data and its Fourier Transform are shown in Appendix B. The Fourier Transform is obtained adopting a Hanning window function [99] from 2.4 $Å^{-1}$ to 17.8 $Å^{-1}$. The Artemis program, using the routines Atoms and Feff [100], is able to generate EXAFS paths from known atomic structures. Goethite and hematite paths are generated and used in two different tests as starting paths for the fitting of the experimental feroxyhyte data. In this way, we would like to verify which of the two iron oxy-hydroxide shows a structure more similar to feroxyhyte. Each path can be described by four parameters, namely atomic coordination number, Debye-Waller factor, E_0 energy shift and interatomic distances. In Table 5.2 the shortest hematite paths are shown. The oxygen atoms forming the coordination octahedron do not feature the same distance from the iron atom, since it is slightly shifted from the center of the polyhedron. The first Fe-Fe distance (2.90 Å) corresponds to face sharing octahedra, while the Fe-Fe distances of 2.971 Å and 3.364 Å belong to edge and corner sharing octahedra respectively. Longer Fe-Fe distances were excluded from the fit procedure. Table 5.3 shows the paths corresponding to the first distances in the goethite structure. As already observed in the case of hematite, two different Fe-O distances are found for the octahedral coordination of the iron atom.

path	N	Amp	R (Å)	atoms
1	3	100	1.946	Fe-O
2	3	82.70	2.116	Fe-O
3	1	13.52	2.900	Fe-Fe
4	3	38.40	2.971	Fe-Fe
5	3	28.69	3.364	Fe-Fe
6	3	26.51	3.398	Fe-O
..	..	..	..	..

Table 5.2: Paths calculated by Feff for hematite. Paths from 1 to 5 were used in the fit of feroxyhyte EXAFS data.

path	N	Amp	R (Å)	atoms
1	2	100	1.953	Fe-O
2	1	49.93	1.954	Fe-O
3	2	85.97	2.089	Fe-O
4	1	42.74	2.093	Fe-O
5	2	37.42	3.010	Fe-Fe
6	1	15.14	3.231	Fe-O
7	2	30.60	3.281	Fe-Fe
8	4	8.79	3.358	Fe-O-O
..	..	..	..	..

Table 5.3: Paths calculated by Feff for goethite. Paths from 1 to 5 and 7 were used in the fit of feroxyhyte EXAFS data.

Fe-Fe distances are longer with respect to the corresponding distances found in hematite, since goethite does not show face-sharing octahedra.

5.4.2 Feroxyhyte starting model for the RMC refinement

A starting model for RMC refinement is built on the basis of the relationship between the Drits cell and the goethite structure. As shown in Section 5.3, four blocks are detectable dividing the monoclinic cell A by four along the x axis (Figure 5.8); atomic coordinates and block parameters are shown in Table 5.4. The starting model for RMC refinement is built randomly stacking these four blocks along the x, y and z directions and imposing constraints on the shortest distances. For this reason, along the c-axis, $block_2$ and $block_4$ cannot follow $block_3$ and $block_2$ cannot follow $block_1$. A better starting agreement between the calculated and experimental XRPD patterns in terms of peak positions, was obtained with blocks

	Block$_1$			Block$_2$			Block$_3$			Block$_4$		
	x	y	z	x	y	z	x	y	z	x	y	z
O1	0.0	0.0	0.302	0.0	0.0	0.288	0.0	0.0	0.198	0.0	0.0	0.212
O2	0.292	0.584	0.788	0.288	0.576	0.802	0.292	0.584	0.712	0.288	0.576	0.698
Fe	0.684	0.368	0.545	0.604	0.208	0.045	0.684	0.368	0.955	0.604	0.208	0.455

Table 5.4: Atomic coordinates and block parameters for the four blocks detected from the goethite structure (a = 2.91 Å; b = 3.01 Å; c = 4.62 Å; $\alpha = 90°$; $\beta = 90°$; $\gamma = 121.17°$).

hematite R_w=0.0018			goethite R_w=0.0017		
path	atoms	R (Å)	path	atoms	R (Å)
1	Fe-O	1.97	1	Fe-O	1.97
2	Fe-O	2.11	2	Fe-O	1.97
3	Fe-Fe	2.98	3	Fe-O	2.11
4	Fe-Fe	3.05	4	Fe-O	2.11
			5	Fe-Fe	2.96
			7	Fe-Fe	3.11

Table 5.5: Result of the EXAFS fits using hematite and goethite paths in terms of distances. Coordination numbers have not been refined.

having the same cell parameters of the Drits unit cell. However, to preserve the goethite nature the coordinates of the atoms are those shown in Table 5.4. The cylindrical shape of the built model corresponds to the same shape proposed by Drits [3]. Based on the experimental TEM and SEM observations, several discs consisting in about 50 thousand atoms which differ in size were generated. The best promising model (12 nm diameter and 3 nm height) was chosen for the RMC refinement. As suggested by Drits, a spherical particle (10Ådiameter) of ultra-dispersed hematite is created and its contribution in terms of calculated XRPD is added.

5.4.3 Results and discussion

Looking at the EXAFS results shown in Table 5.5, a good fit has been obtained using both hematite and goethite paths. The agreement values of R_w are small and in the same order of magnitude. This result might be expected, since the local structure between iron oxides is quite similar. The same results in terms of first Fe-O distances are produced: 1.97 Å for the closest three oxygen atoms, 2.11

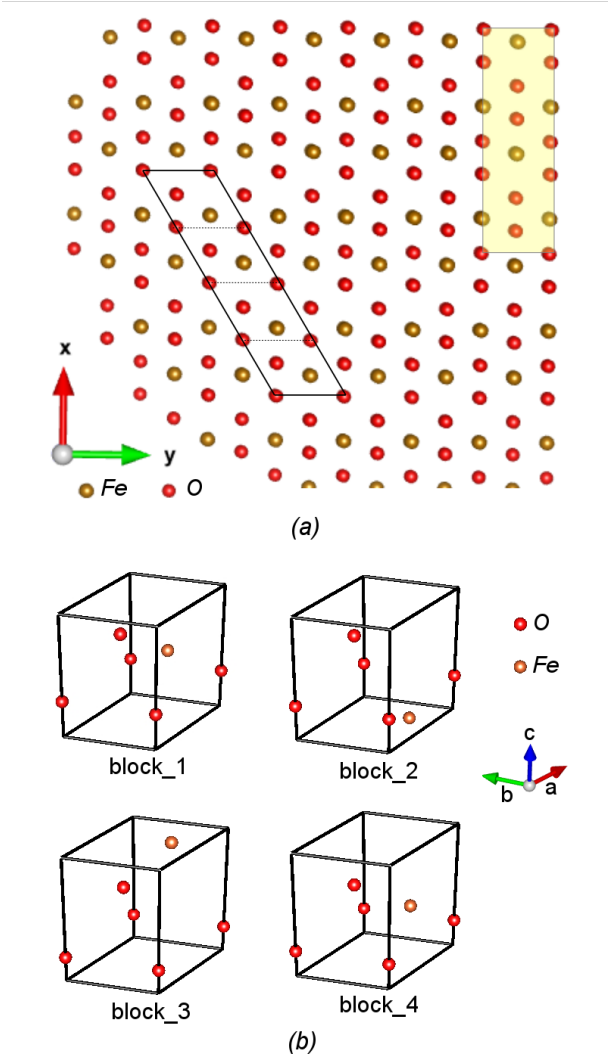

Figure 5.8: (a) The network of the goethite in the xy plane projection. The orthorombic cell is figured on the right; the alternative monoclinic cell is on the left. This cell is composed by four blocks, shown in (b). These blocks have the same lenght of a, b, c and the same value of α, β, γ, but different atomic coordinates (see Table 1).

Å for the remaining three. The first Fe-Fe distance is found at 2.97 Å and 2.98 Å starting from hematite and goethite respectively. Interestingly, these values are in between the typical distances found in face sharing octahedra and in edge sharing octahedra. Finally, different results are apparent for the second Fe-Fe distance. The difference in starting amplitude between path 4 of hematite and path 7 of goethite should be taken into account in order to explain this dissimilarity. EXAFS is unable to unambiguously solve the presence of face sharing octahedra in the feroxyhyte structure, although the distance found for the first Fe-Fe distance is closer to the typical value for edge-sharing octahedra than to the value expected for face sharing octahedra. The results collocate the feroxyhyte structure at a midpoint between the structures of hematite and goethite. It should be noted that EXAFS describes the average local structure around the absorbing atom. In view of that, face-sharing octahedra cannot be excluded.

The model built for the RMC refinement in this work shows some structural differences with the model proposed by Drits with regard to the arrangements of the blocks. Indeed, as described in Section 2.3, Drits suggests that the local structure of feroxyhyte is made by face-sharing octahedra-chains along the c-axis: two octahedral sites occupied by the iron atom are followed by two unoccupied sites. In the goethite structure, because every block is followed by a block of the same kind along the c-axis, an octahedral site occupied by the iron atom is followed by one unoccupied site. Instead, because of the random stacking of the blocks, the features of our model with respect to the octahedra sequence along the c-axis, can be summarized as follows:

- face-sharing octahedra occur as a consequence of the stacking of block_2 on block_4 and block_1 on block_3
- goethite network (occupied octahedron followed by vacant octahedron) occurs as a consequence of the stacking of two blocks of the same kind.

The sequence of the blocks on the xy plane shows that the goethite network is preserved when, along the y-axis, a block follows a block of the same kind and, along the x-axis, when the sequence 1-2-3-4 occurs. In some way, the stacking along the three axes gives rise to a mixture of the features typical of the Drits model with those typical of the goethite structure. In that sense, we can say that the model built for the RMC refinement is in agreement with the EXAFS results. As described earlier, both ultradispersed hematite structure and feroxyhyte structure are refined at the same time with the RMC method. In Figure 5.9 the experimental and the calculated diffraction pattern after the RMC refinement using the best model is shown. RMC refinement on ultradispersed hematite improves the agreement between experimental and calculated pattern in the diffuse scattering, whereas refinement on feroxyhyte model results in a reduction of the

intensity differences on the peaks. A satisfactory agreement between experimental and calculated data has been obtained. Small differences can only be detected at q = 3.9 $Å^{-1}$ and in the region q = 4.5 $Å^{-1}$ - 5.5 $Å^{-1}$. Our work shows that good results were obtained without introducing face-sharing octahedra chains, although, in this model, face-sharing octahedra is not totally excluded. Further insights on the structural model can be inferred from the results obtained by the calculated patterns using different amounts of hematite. Best results in terms of agreement with the experimental pattern were obtained using 30% ultradispersed hematite. Although the role of the synthetic procedure on the relative amount of hematite should be taken into account, the contribution of hematite found in our work is significantly higher than the one arising from Drits. In order to obtain a better agreement with the experimental data, Drits suggests the presence of 5% stacking faults. In our description stacking faults do not systematically occur. Agreement in the intensity of the peaks is achieved exclusively allowing for small displacements of iron and oxygen atoms from the original positions. Overall, although the Drits model has been so far a valuable tool to represent the mean structure of feroxyhyte, we have demonstrated that an alternative interpretation results in a local structure with features closer to the other well known structures of iron oxy-hydroxides. This work does not solve unambiguously the local arrangements of the feroxyhyte structure, but shows how a good agreement with the experimental data can be obtained using a different local structure network. Future developments include RMC refinement on the reciprocal and direct space simultaneously and taking into account different possible ways of stacking the goethite blocks.

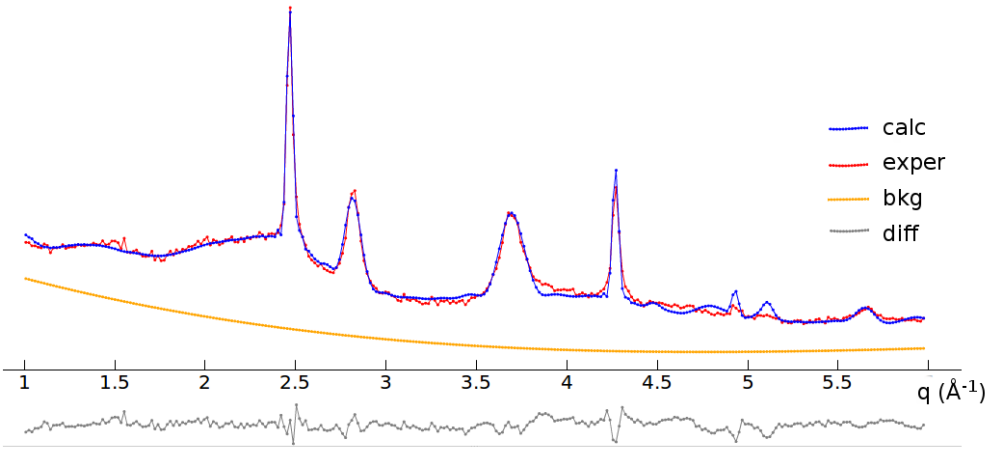

Figure 5.9: Experimental and calculated XRPD patterns for the model of ferroxyhyte obtained stacking the blocks of Figure 5.8 after the RMC refinement.

Chapter 6

Ferrihydrite structural analysis

6.1 Overview

As stressed in Section 2.3, ferrihydrite structure has been a hot topic for material scientists in recent years, especially after Michel and others presented a new model in 2007 [33] as an alternative to the previous model proposed by Drits and others in 1993 [2]. Both models were supported by different works, but no experimental incontrovertible evidence has been disclosed so far. In 2013 Gilbert and others presented a new model [41]. Interestingly, the latter is a hybrid between the Drits and the Michel model, found using the whole-particle-RMC approach which we touched upon in Chapter 4. Spherical particles with a diameter of 3.6 nm were built in order to represent the Drits model, the Michel model and a hybrid disordered model showing structural features both of the Drits and the Michel models. These models were used as starting models in an RMC analysis in which the differences between experimental and calculated data both in the real space and in the reciprocal space were minimized. The data in the reciprocal space was calculated using the Debye Scattering Equation. Due to its complexity, the Drits model has been simplified, using the defect-free phase and representing the defective-phase introducing stacking faults. Hematite was not considered. In our work, an EXAFS and an RMC analysis using the program DMC have been performed with the aim of evaluating the agreement of the Drits and Michel models with the experimental data. We addressed the complex Drits model, taking into account structural features not considered by Gilbert, like the presence of hematite or the possible local arrangements produced by stacking defective and defect-free unit cells. We will show that there is no way to describe all of the possible structural motifs of the Drits model using a single representative particle. Our results are compared with those obtained by Gilbert.

6.2 Experimental and methods

6.2.1 Synthesis and characterization

Ferrihydrite 6L was prepared adding unhydrolysed 7.5 g of $Fe(NO_3)_3 \cdot 9H_2O$ to 750 mL of preheated water and leaving the solution stirring at 75°C for 10 minutes. The solution was then rapidly cooled in an ice bath for 20 minutes and titered at room temperature with KOH 1M until pH = 7. A centrifuge was used in order to separate the precipitate, which was repeatedly washed with distilled water and then dried in an oven. The synthesis yielded 1.9 g of ferrihydrite. A laboratory x-ray diffraction pattern was collected on a PANalytical Empyrean diffractometer using a Cu-Kα tube operating at 40 kV and 40 mA, coupled with a graphite monochromator on the diffracted beam and a X-Celerator linear detector, scanning over an angular range 2θ = 10-110°. Small portions of the solution were taken during the titration at pH = 3, 4, 5 and 6, in order to study the formation of ferrihydrite at different pH values. All the samples were dried and characterized using Cu-Kα x-ray diffraction. The formation of ferrihydrite starts at low pH in a very small concentration (diffraction patterns are shown in Appendix B). The adding of the base is required in order to have substantial precipitation, although, if the pH is too high, the most stable hydroxide goethite is formed [101]. The Cu-Kα diffraction pattern of the sample at pH=7, which is used in TGA, EXAFS and synchrotron measurements, is shown in Figure 6.1. It displays the characteristic six peaks at 2θ = 35°, 40°, 45°, 55°, 63° and 64°. Synchrotron x-ray diffraction pattern was collected at the Elettra Synchrotron MCX beamline in Trieste, using 20 KeV radiation (λ = 0.62 $\AA$). A transmission mode experiment was performed, using a 0.5 mm boron-silica glass capillary collecting data for 40 hours in the angle range 2θ = 3-161°. EXAFS data was collected at the Elettra Synchrotron 11.1 (XAFS) beamline in Trieste at room temperature using a Si (111) monochromator in transmission mode at the Fe K-edge (7112 eV). Samples were prepared by pressing the powders diluted in polyvinylpyrrolidone (PVP) into pellets. Thermogravimetric and differential thermal analysis (TGA and DTA) were performed on a 851 Mettler Toledo TGA/SDTA at a heating rate of 10°C/min from room temperature to 1000°C in an O_2 atmosphere placing about 30mg of ferrihydrite in an alumina crucible. The TGA/DTA data, shown in Appendix B, is in agreement with that observed by other authors [101], showing an endothermic transformation with a loss in weight of 26% between 100°C and 200°C, compatible with the transformation into hematite.

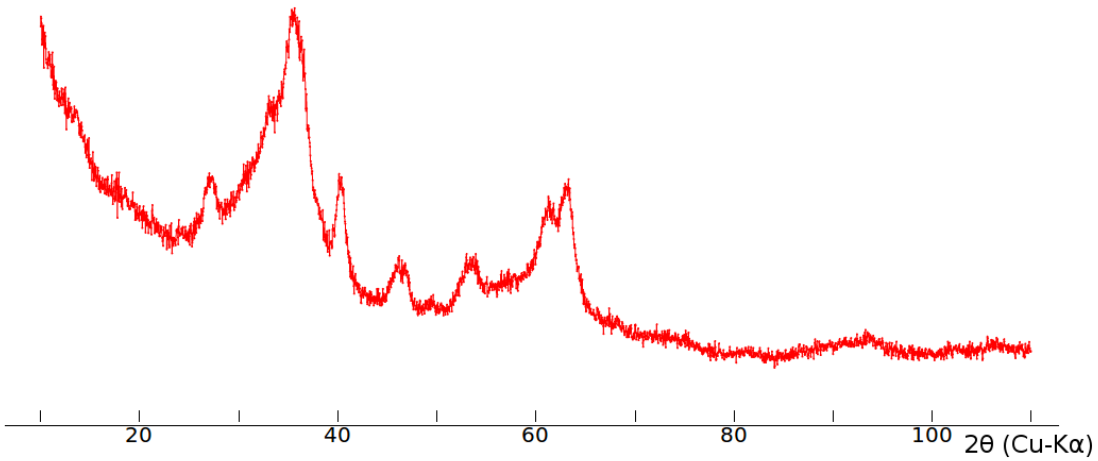

Figure 6.1: The diffraction pattern of ferrihydrite, showing the characteristic six peaks at $2\theta = 35°$, $40°$, $45°$, $55°$, $63°$ and $64°$

6.2.2 EXAFS data analysis

The Demeter suite [78] is used for EXAFS data analysis. The program Athena is used for the treatment of the experimental data: to sum the different collections, to fit pre- and post- edge background and to extract the normalized absorbance as a function of the wavevector k. The program Artemis is exploited in order to obtain structural information. First Fe-O and Fe-Fe paths in terms of distances from the absorbing atom Fe are calculated on the basis of the Michel and the Drits models using the Atoms and FEFF routines [100]. These paths are used to obtain the starting distances and coordination number values in two different data sets, with the aim of studying the agreement between the experimental data and the two models. The atomic positions obtained from neutron diffraction data and Rietveld refinement for the Drits model [32], both for defective and defect-free phases, were used instead of the original coordinates proposed by Drits. The corresponding CIF files are available in Appendix C. The calculated Fe-O and Fe-Fe paths used in the fitting procedure are shown in Table 6.1 Three oxygen atoms are closer to the central iron than the others, since the iron in the Drits model is shifted from the center of the octahedron. In the defective phase this shift is larger allowing face sharing between octahedra. It should be noted that the Fe-Fe distance for sharing face octahedra found by Jansen (2.995 Å) is shorter

than the distance found in the original Drits model (1.88 Å). The same value of 2.995 Å is also found for Fe-Fe distances in the sharing edge octahedra of the defect-free phase. The coordination number is calculated taking into account the occupancies of Fe sites (0.4 in defect-free cell and 0.25 in defective cell). All of the distances were allowed to change during the fitting procedure. In order to reduce the number of degrees of freedom, only two Debye-Waller parameters are considered, σ_{Fe-O} and σ_{Fe-Fe}, which is the variance in the distances of Fe-O and Fe-Fe pairs, respectively. The ratio between defect-free and defective phases is set to 1:1. The atomic positions for the Michel model (Table 6.1) are calculated using the model Fhyd6 presented in 2007 [33]. The corresponding CIF file is available in Appendix C. In Michel Model both octahedral (80%) and tetrahedral (20%) coordination of oxygen atoms around iron atoms is found. The octahedron is distorted, showing four different Fe-O distances. In the tetrahedron, one of the four oxygen atoms is much closer to the iron. Despite the presence of a Fe-Fe distance of 1.91 Å the Michel model does not display face sharing. The effective coordination number is then calculated taking into account the ratio between the tetrahedral and octahedral coordination. The EXAFS spectrum chi(k)*k^3 from experimental data is Fourier transformed from k = 2.0 to k = 17.7 $Å^{-1}$ to obtain a Radial Distribution Function not corrected for the phase shift. A Hanning function[99] is also used as a dumping function to minimize the termination effects in the Fourier transformation. The function in the real space is then fitted in the range from r = 1.0 Å to r = 3.1 Å.

6.2.3 RMC analysis using DMC

6.2.3.1 Michel model

Four different representative spherical particles of 4nm of diameter representing the Michel model were created, varying the amount of vacant sites of the iron atom (0%, 10%, 20% and 30%). The vacancies are randomly distributed on octahedral and tetrahedral sites. The calculated x-ray diffraction pattern of the four particles are shown in Figure 6.2. Differences mainly pertain to the intensities of the peaks at q = 2.5, 3.8 and 4 $Å^{-1}$, which decrease at the increasing of the vacancy rate. The best promising two models (20% and 30% of vacant sites, respectively) were chosen for the RMC refinement.

6.2.3.2 Drits model

The stacking of the defect-free and defective cells may generate very different local structural motifs. Four blocks, called ABA1, ABA2, ACA1 and ACA2, shown in Figure 6.4, can be used in order to describe the Drits structure networks. Each block displays the cell parameters of the defective unit cell and contains

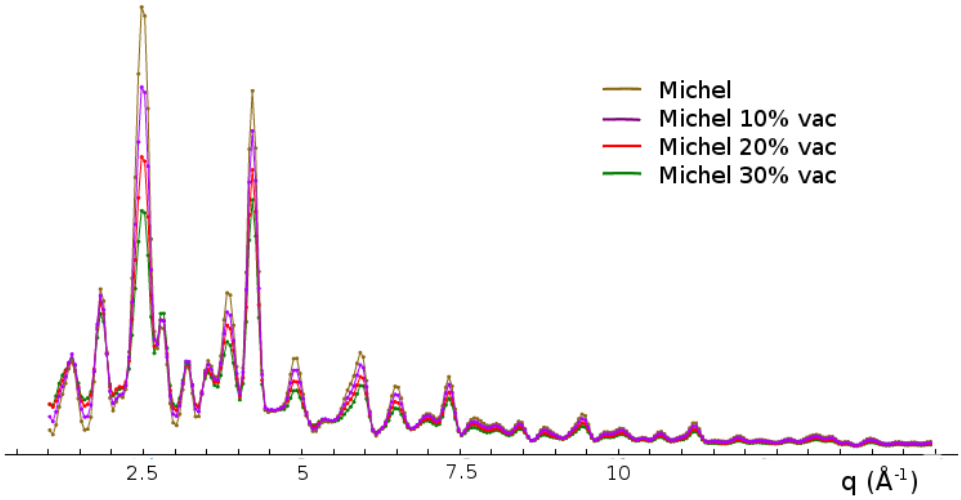

Figure 6.2: Calculated x-ray diffraction patterns of the Michel model with different amount of vacant sites of the iron atom (0%, 10%, 20% and 30%).

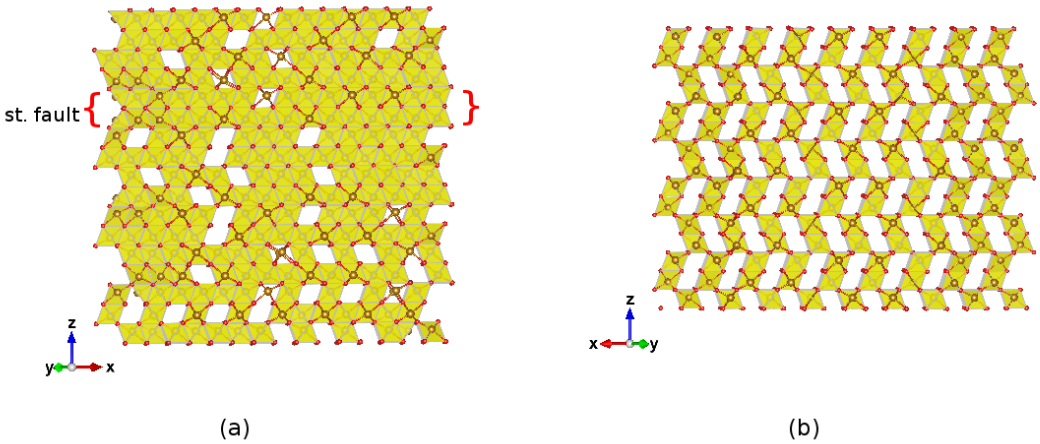

Figure 6.3: (a) The structure of ferrihydrite according to Drits. Depending on the stacking of the blocks, different local structural motifs can be generated. The defective phase is originated by stacking faults. (b) The defect-free supercell structure.

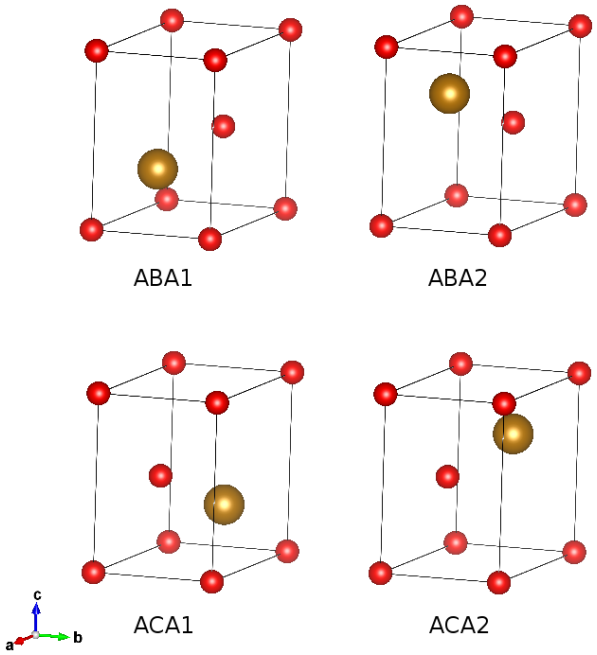

Figure 6.4: The blocks composing the Drits model

two oxygen atoms and one iron atom with a site occupancy equal to 1. If an ABA block is followed along the z direction by an ACA block, the resulting phase is defect-free. The defective phase results due to the stacking of ABA with ABA or ACA with ACA blocks. Octahedra sharing faces are generated if ABA2 is followed by ABA1 or if ACA2 is followed by ACA1, as a special case of the defective phase. A set of representative particles were generated taking into account different random stacking configurations. Their diffraction patterns were calculated, displaying significant differences, even in patterns generated using the same stacking probability, as shown in Fig 6.5a. The position of the stacking faults, the number of stacking faults and the distance between two faults result in a great influence in the intensities of the peaks. Nevertheless, none of the calculated patterns seem to be consistent with the experimental, since the peak at q = 2.4 $Å^{-1}$ in the calculated patterns shows a similar intensity, if not smaller, with respect to the peak at q = 2.6 $Å^{-1}$, while in the experimental data the first is considerably larger than the second. The peak at q = 2.4 $Å^{-1}$ becomes more intense if a defect-free supercell results from the stacking of the blocks (Figures 6.5b and 6.3b). In this supercell the block ABA1 is followed by ABA2 along x and y and vice versa and, along z, ABA1 is followed by ACA1 and ABA2 by ACA2. However, the calculated pattern of a particle showing a supercell's regions displays a peak at q = 1.25 $Å^{-1}$ due to the increase of the periodic unit along x and y, which does not appear in the experimental pattern. The most promising model is chosen for the RMC refinement. As suggested by Drits, ultradispersed hematite was considered in the fitting, by calculating the diffraction pattern of a hematite spherical particle of 2nm of diameter and by adding it to the ferrihydrite diffraction pattern. Hematite shows a peak around q = 2.5 $Å^{-1}$, improving the agreement between experimental and calculated data. A fit with the purpose of obtaining the best ratio hematite/ferrihydrite is performed using GSL linear fitting libraries [86] before the RMC iterations begin.

6.3 Results and discussion

A good EXAFS fit is obtained using both Drits-Jansen paths and Michel paths. Some considerations can be pointed out looking at the resulting parameter values and comparing them with the starting values (Table 6.1). The final Fe-O distances found in the fit using Drits paths (paths 1, 2, 5, 6) do not exhibit differences with the model, except for path 5. The shift of the iron atom from the center of the octahedron due to the face-sharing, which if present, could be overestimated in the Drits model. The shortest Fe -Fe distance is 2.96 Å, which does not change from the stating value. This value does not assure the presence of face-sharing octahedra, since it is exactly in the midpoint between the Fe-Fe distances usually

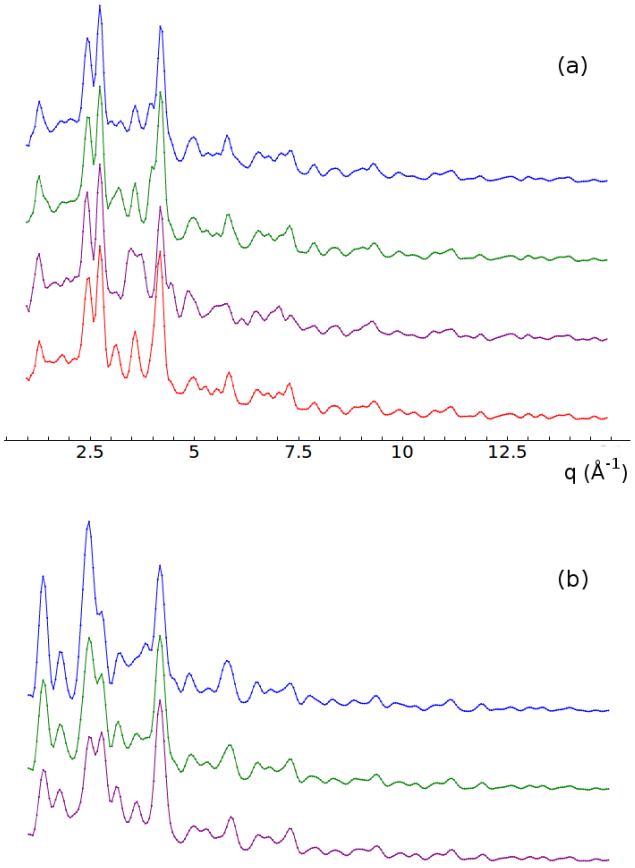

Figure 6.5: (a) X-ray diffraction patterns calculated from models with the same stacking probability show significant differences. (b) X-ray diffraction patterns calculated from models contemplating the presence of defect-free supercell. The blue pattern is calculated from a model with only defect-free supercell. The presence of defect-free supercell is progressively decreasing for the green pattern and the violet pattern, with the progressive reduction of the intensity of the peak at q = 1.25 $Å^{-1}$.

$R_{fit} = 0.00031$					
path	pair	N	start dist (Å)	fit dist (Å)	Δr (Å)
Drits defect-free					
1	Fe-O	3	2.01	1.99	0.02
2	Fe-O	3	2.13	2.14	0.01
3	Fe-Fe	2.4	2.96	3.10	0.14
4	Fe-Fe	1.2	3.07	3.37	0.30
Drits defective					
5	Fe-O	3	1.87	1.96	0.09
6	Fe-O	3	2.32	2.33	0.01
7	Fe-Fe	1.5	2.96	2.95	0.01
8	Fe-Fe	1.5	3.33	3.46	0.13
$\sigma_{Fe-O} = 0.012$					
$\sigma_{Fe-Fe} = 0.012$					

Table 6.1: EXAFS fit results for the Drits model.

found in iron oxy-hydroxides involved in face-sharing and edge-sharing octahedra. The fit using Michel paths returns shorter Fe-O distances. A value of 1.97 Å is found for all the Fe-O paths, except for path 4. This value is extremely far from the shortest Fe-O distance found in the Michel model, but it is in agreement with other EXAFS results [38; 101]. It should be noted that Fe-O distances of Michel model have been criticized because of the violation of Pauling's 2^{nd} rule [36] (see Section 2.4) and further corrections have been proposed by Michel in 2010 [37]. The shortest Fe-Fe distance value is slightly larger than the value found in the fit performed using Drits paths and it is more attributable to a distance typical of edge-sharing than face-sharing octahedra. Longer Fe-Fe distances could not be easily interpreted, since they come out from shells at higher r-values.

In Figure 6.6 is reported a comparison between the variation of the agreement values χ^2 with the number of moves performed during the RMC refinement for the Drits and Michel models. Best starting agreement for Drits model is found to have a large amount of hematite phase, up to 60%, a value tremendously different from that proposed by Drits. The large amount of hematite component comes out in order to improve the agreement with the experimental data in the region around q = 2.5 $Å^{-1}$, where the most intense ferrihydrite peak falls. Nevertheless, the Michel models with 20% and 30% of vacant sites give better results than the Drits model in terms of the total agreement between functions and experimental data both in reciprocal and real space. In Figures 6.7 and 6.8 the results of the fits for the Drits model (a) and for the Michel model with 30% of vacancies (b) are reported. The pattern calculated from the Drits model shows better agreement in terms of peak

$R_{fit} = 0.0011$					
path	pair	N	start dist (Å)	fit dist (Å)	Δr (Å)
Michel					
1	Fe-O (oct)	0.8	1.94	1.97	0.03
2	Fe-O (oct)	1.6	2.01	1.97	0.04
3	Fe-O (oct)	0.8	2.04	1.97	0.07
4	Fe-O (oct)	1.6	2.14	2.15	0.01
5	Fe-O (tet)	0.2	1.79	1.97	0.18
6	Fe-O (tet)	0.6	1.95	1.97	0.02
7	Fe-Fe	2	2.91	2.97	0.06
8	Fe-Fe	2	3.01	3.11	0.10
$\sigma_{Fe-O} = 0.010$					
$\sigma_{Fe-Fe} = 0.007$					

Table 6.2: EXAFS fit results for the Michel model.

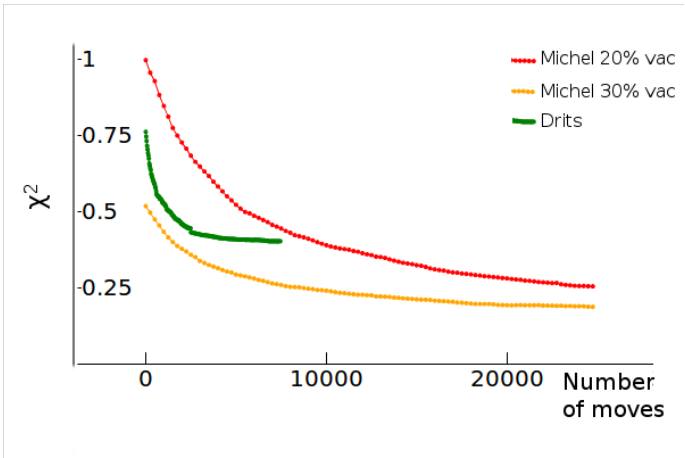

Figure 6.6: The variation of the agreement value χ^2 during the RMC refinement using DMC for the Michel models with 20% and 30% of vacant sites and the Drits model.

positions, but the intensities and shapes of the peaks are not well reproduced. The Michel model fails to reproduce peak position, as already observed by several authors [35; 41]. In particular the region before q = 2.5 $Å^{-1}$ shows two peaks not present in the experimental data. Other two peaks (at q = 3.5 $Å^{-1}$ and 3.85 $Å^{-1}$) resulting from the Michel model are absent in the experimental pattern. Moreover, the peak experimentally observed at q = 3.7 $Å^{-1}$ is not reproduced by the calculated data. The PDF function of the Michel model rising by the RMC refinement correctly reproduces the experimental data. It was an expected result, since this model was hypothesized on the basis of real space studies. The PDF obtained from the Drits model shows significant differences with the experimental PDF, especially at R $\simeq$ 3 Å, in correspondence of the first Fe-Fe distances, and in the range R = 4-7 Å. In summary, the EXAFS analysis does not solve the question of the presence of tetrahedral coordination or the presence of face-sharing octahedra, both of which are characterizing features of the Michel and Drits models respectively, but it does indicate that both of the models need to be reviewed in terms of distances. Important information was obtained from the RMC analysis. As found by Gilbert and others [41], neither the Drits model, nor the Michel model are able to accurately describe the experimental diffraction pattern and the PDF data. With respect to the work of Gilbert, we addressed the multifaceted features of the Drits model more. Unsatisfying results were obtained, however we have been unable to build a model hosting the numerous local arrangements proposed by Drits. The results of a single particle model are too small to be considered as representative of the complex Drits model and, probably, different and better results could be obtained using multiparticle systems.

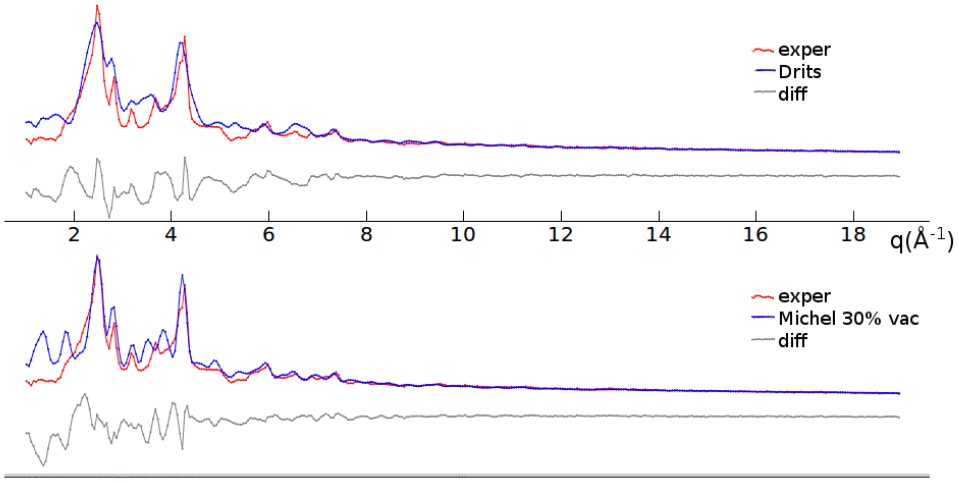

Figure 6.7: The diffraction patterns after RMC refinement for the Drits model (a) and the Michel model with 30% of vacancies (b) compared with the experimental data.

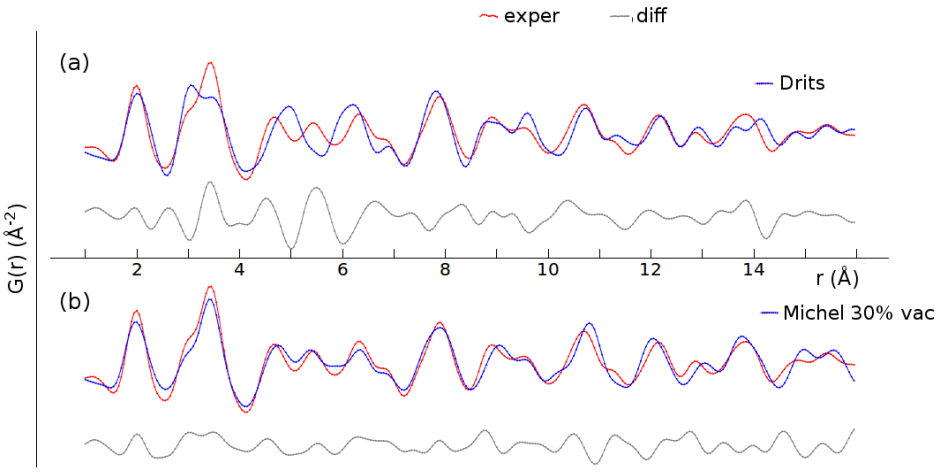

Figure 6.8: The PDFs after RMC refinement for the Drits model (a) and the Michel model with 30% of vacancies (b) compared with the experimental data.

Chapter 7

Schwertmannite structural analysis

7.1 Overview

Rietveld refinement and RMC analyses using the DMC program were conducted on schwertmannite in order to study the validity of the model proposed by Fernandez-Martinez et al. in 2010 [5]. As introduced in Section 2.5, these authors suggest that schwertmannite shares structural motifs with the iron oxy-hydroxide akaganeite (as previously proposed by other authors [4]), with sulfates occupying two possible sites. In one site the sulfur shares two oxygen atoms with the octahedral iron framework belonging to the akaganeite-like network, forming an inner sphere complex, located in the proximity of the walls of the channel. In the other site the sulfate group is located in the center of the channel and it is bonded with the oxygen atoms of the akaganeite-like structure *via* H-bonds (outer sphere). The diffraction patterns of two synthetic and two natural samples were collected and used as experimental data in the Rietveld and RMC refinements. It is known that schwertmannite transforms to goethite or jarosite [46; 102; 103; 104; 105; 106; 107] upon mixing with near-neutral water. Actually, some authors have reported the presence of goethite in schwertmannite samples studied by HR-TEM. [45]. In particular, an intimate structural relationship between the structures of goethite and schwertmannite has been described by Fernandez-Martinez et al (2010). The transformation of schwertmannite into goethite would be achievable by a simple relocation of iron octahedra from the structure of schwertmannite [5], in a simple topotactic transformation. For this reason, in our study the presence of additional goethite has been contemplated.

7.2 Synthesis and characterization

Data from different samples, natural and synthetic, is used in this study. Sample *SynHT* was synthesized by dissolving about 25 g of $Fe_2(SO_4)_3$ in 500 mL of deionized water at 85°C for 1 hour. The precipitate was vacuum filtered and freeze-dried to complete dryness using a VirTis Benchtop freeze-dryer (Hucoa-Erlss). Sample *Syn* was synthesized according to Schwertmann and Cornell [98] by adding $FeCl_3$ into a solution of Na_2SO_4 at 60°C. After 12 min the produced suspension was cooled to room temperature and dialyzed for 30 days. Natural samples *Nat-Air* and *Nat-Freeze* were taken from the Monte Romero mine in Spain (Iberian Pyrite Belt), as fresh precipitates from the acid drainage. Sample *Nat-Air* was air-dried, while sample *Nat-Freeze* was freeze-dried. HEXD measurements were carried out at the beamline ID15B at the European Synchrotron Radiation Facility (ESRF) using a monochromatic x-ray with an energy of $\sim$ 87 KeV (0.1419 Å) in Debye-Scherrer geometry, where the samples were loaded in polyamide (kapton) capillaries. The beamline was calibrated using a CeO_2 standard (NIST 679b) for the data collection of the sample *SynHT* and using a Ni standard for the data collection of samples *Syn*, *Nat-Air* and *Nat-Freeze*. The diffraction patterns were collected using a MARCCD165 2D (sample *SynHT*) and a Pixium 4700 (samples *Syn*, *Nat-Air* and *Nat-Freeze*) detector and the data was converted from 2D to 1D using the program Fit2D [108].

7.3 Rietveld refinement: models and refinement strategy

The program Maud [109] is used for the Rietveld refinement. Both the schwertmannite and goethite models were included in the refinement procedure. Schwertmannite presents a triclinic structure with the akaganeite-like channels hosting the sulfate groups. Sulfate groups occupy 4 different positions in the Fernandez-Martinez et al. model, with two sulfates forming outer sphere complexes and two other in inner-sphere complexes. Here, a unit cell with eight sites for sulfates has been considered in order to allow the possibility that sulfates can be distributed in a different way than that described by Fernandez-Martinez et al. Four of them share two oxygen atoms with the iron atoms forming the channels (inner sphere sulfate), the remaining four are placed in the center of the channel and they are bonded with the FeOOH network *via* H-bonds. In this model the resulting stoichiometry is $FeOOH \cdot 0.25[SO_4]^{2-}$, since each sulfate site shows an occupancy equal to 0.5. The CIF files of goethite and schwertmannite which were used as starting models in the fit are reported in Appendix C. Two fits were performed on each sample, the first considering only the presence of schwertmannite, the

second contemplating also the presence of goethite. The following refinement strategy was applied:

- the starting diffraction pattern was calculated considering a spherical shape domain with the diameter of 4 nm and by applying a scale factor in such a way that the intensity of the calculated pattern is roughly comparable with that of the experimental data, in order to steer the goodness of fit;

- the first step was performed in order to refine the scale factor, the background (estimated with a 4^{th} degree polynomial) and the 2θ offset. In the case contemplating the presence of goethite, the concentration of the two phases is also refined;

- the second step also considers the domain size and the cell parameters;

- finally, the sulfate occupancies were optimized. Some constraints are posed: the occupancy of the oxygen atom in a sulfate group is equal to the occupancy of the bonded sulfur; the sum of the sulfur occupancies must be equal to 4; the occupancy of the inner sulfate is equal to 1 minus the occupancy of the outer sulfate. In this way, only four degrees of freedom are added to the system.

No further parameters were involved in the refinement in order to avoid a large number of degrees of freedom.

7.4 Models for RMC

The DMC program was used for the RMC analysis. Three single particle models of schwertmannite were created by stacking a convenient number of schwertmannite unit cells (see Appendix C for the CIF file of the used unit cells). The particles have a spherical shape with a diameter of 3 nm. In order to explore the effect of the sulfate occupancy, the models differ in the inner/outer sulfate ratios. The first model comprises 50% inner sphere and 50% outer sphere sulfates, the second model comprises 30% inner sphere and 70% outer sphere sulfates, the third comprises 70% inner sphere and 30% outer sphere sulfates. The Goethite particle was generated by stacking the goethite unit cell (see CIF file in Appendix C) and cutting a sphere with a diameter of 3 nm. Partially coordinated iron atoms on the surface of the particles had been removed. In the cases contemplating the presence of goethite, the positions of the atoms of both schwertmannite and goethite were refined.

	SynHT	Syn	Nat-Air	Nat-Freeze
R_w with goet (%)	4.3	4.6	4.5	4.7
R_w without goet (%)	9.1	5.8	4.8	5.4

Table 7.1: Agreement parameter R_w of the Rietveld refinements of the studied samples with and without the presence of goethite.

	SynHT	Syn	Nat-Air	Nat-Freeze
goethite (%)	26	15	14	13
schwertmannite (%)	74	85	86	87

Table 7.2: Amounts of goethite and schwertmannite found by Rietveld refinements for the studied samples in the fits contemplating the presence of goethite.

7.5 Results and discussion

In Table 7.1 the result of the fits in terms of the agreement parameter R_w (%) for the four samples with and without goethite is shown. The presence of goethite guarantees a better result in all of the studied cases. This is absolutely clear for the *SynHT* sample, where the goethite concentration found is the highest, while for the other samples the difference between the agreement parameter of the fit contemplating goethite and that of the fit without goethite is smaller. The effect of the presence of goethite can be better appreciated by looking at the diffraction patterns shown in Figure 7.1, where the Rietveld fits for the samples *SynHT*, *Syn*, *Nat-Air* and *Nat-Freeze* in the presence and absence of goethite are reported.

Regarding the sample *SynHT*, the presence of goethite is required in order to reproduce the peak at $2\theta = 3°$, which corresponds with the (101) peak of goethite. The addition of this phase also results in the improvement of the intensity of the peaks at $2\theta = 5°$ and, though to a lesser extent, at $2\theta = 3.75°$ and $2\theta = 6.25°$. The peak at $2\theta = 3°$ appears less intense in the remaining patterns. In the samples *Syn* and *Nat-Air* this peak can be distinguished as a shoulder of the peak at 2θ= 2.5°, while in the sample *Nat-Freeze* is not distinguishable at all. This behavior is in agreement with the values found for the concentration of goethite (Table 7.2), that is progressively decreasing from the sample *SynHT* to the sample *Nat-Freeze*. Although not distinctly observable in the pattern of the sample *Nat-Freeze*, the presence of goethite assures the perfect reproduction of the peak shape. The values of the refinable parameters found by the Rietveld refinement are shown in Table 7.3. Domain size does not significantly change during the refinement process, except for the *SynHT* sample. Anyway, taking into account the error that can be produced by considering surface effects and disorder, all the values

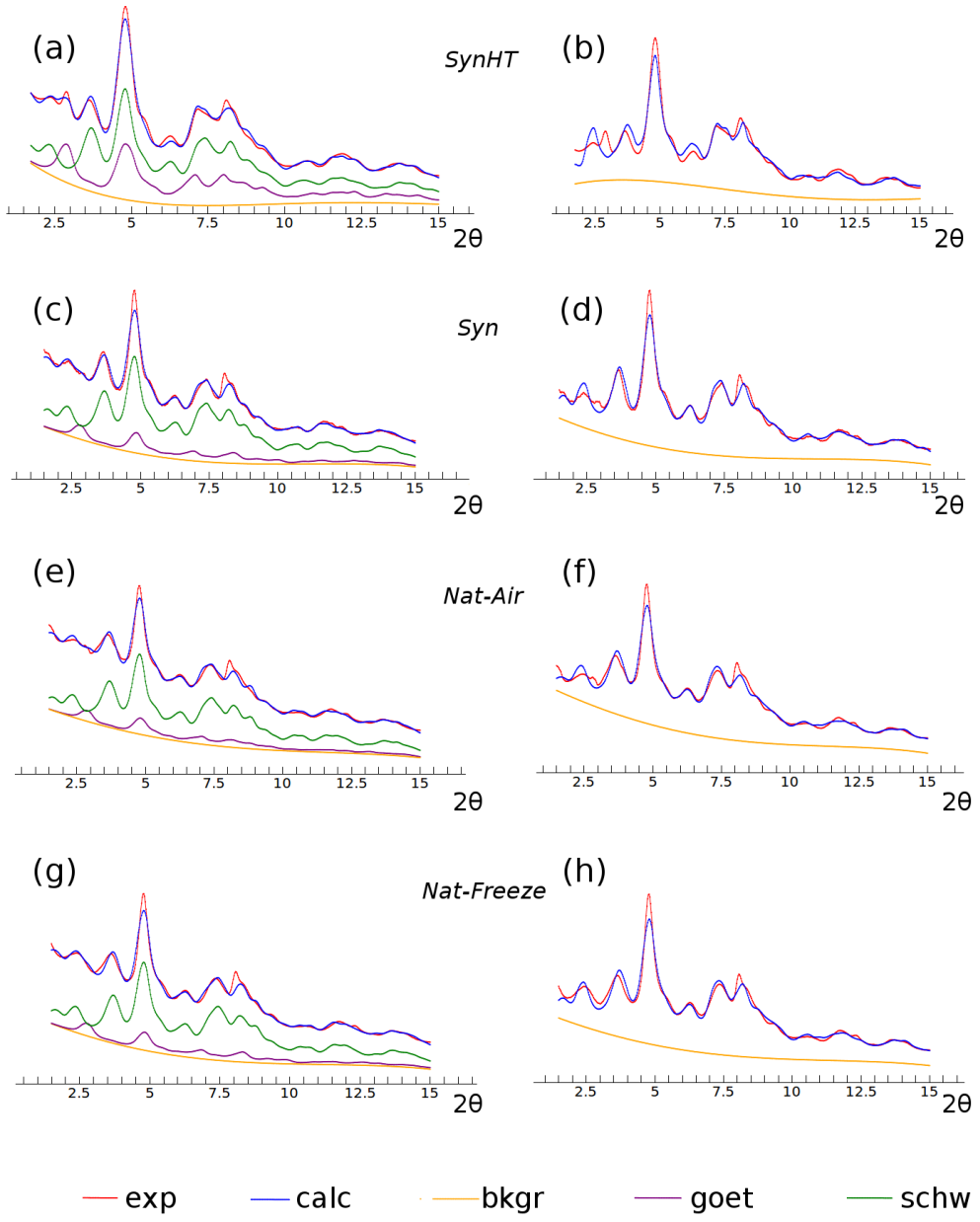

Figure 7.1: Rietveld refinements for sample *SynHT* with goethite (a), sample *SynHT* without goethite (b), sample *Syn* with goethite (c), sample *Syn* without goethite (d), sample *Nat-Air* with goethite (e), sample *Nat-Air* without goethite (f), sample *Nat-Freeze* with goethite (g), sample *Nat-Freeze* without goethite (h).

Parameter	SynHT	Syn	Nat-Air	Nat-Freeze	Starting
Size goet (Å)	44	40	40	40	40
Size schw (Å)	36	41	40	40	40
Cell goethite					
a (Å)	9.60	8.98	9.40	8.9	9.9134
b (Å)	3.08	3.06	3.08	3.06	3.0128
c (Å)	4.67	4.92	4.59	5.0	4.58
Cell schwertmannite					
a (Å)	10.48	10.43	10.59	10.45	10.5870
b (Å)	6.04	6.07	6.08	6.08	6.0622
c (Å)	10.42	10.54	10.32	10.43	10.515
α	91	90	90	90	90
β	85	85	86	85	87
γ	89	90	90	90	90
Sulfate occupancy					
inner sphere	2.11	2.17	1.87	2.21	2
outer sphere	1.89	1.83	1.13	1.79	2

Table 7.3: Parameters found by Rietveld refinements for the studied samples in the fits contemplating the presence of goethite.

can be considered in accordance with literature [45]. With respect to the cell parameters, comparable results are found for the schwertmannite unit cell, which do not considerably change from the starting values. On the other hand, goethite displays alterations of the a and c axes, with a common tendency to decrease for a and to increase for c. With respect to the sulfate occupancy, refinement produced no improvement of results. The sulfate inner/outer ratio has implications on the ratio of the intensity of the peaks at $2\theta = 2.5°$ and $2\theta = 3.75°$. The intensity of these peaks is almost reproduced before considering the sulfate occupancy as a refinable parameter. The starting inner/outer ratio $\simeq 1$ guarantees a good fit and it does not vary during the refinement procedure. Differences between calculated and experimental patterns remain after the refinement procedure. They regard the peaks at $2\theta = 5°$ in all of the studied patterns, which are not reproduced in intensity, especially for the samples *Syn*, *Nat-Air* and *Nat-Freeze*, and the peak at $2\ \theta = 8°$, which is also not reproduced in shape.

In order to address the results obtained by Rietveld refinement, an RMC refinement is conducted for the samples *SynHT* and *Nat-Freeze*, since they show the extreme cases with respect to the presence of goethite. We also focused on the effects of the inner/outer sulfate ratios. With respect to the model *SynHT*,

we conducted three RMC simulations using the three different schwertmannite particles with different inner/outer sulfate ratios as starting models. The amount of goethite content is evaluated before RMC starts by applying linear fitting on the experimental diffraction pattern. The resulting calculated diffraction pattern is a weighted sum of the patterns calculated from goethite and schwertmannite particles. A background (3^{rd} degree polynomial) is added in order to consider the presence of other structural contributions by water or amorphous content. A similar goethite content (30%) is estimated for the three schwertmannite models. Results in terms of variation of the agreement parameter as a function of the number of moves are shown in Figure 7.2. The model with a 50% inner and a 50% outer sphere sulfate gives the best agreement both before RMC iterations and at the end of the refinement. The resulting diffraction pattern and PDF for this model are shown in Figures 7.3 and 7.4, displaying a goodness of fit between experimental and calculated data. Peaks in the diffraction pattern are adequately reproduced, confirming the results obtained by the Rietveld Refinement, while slight differences in PDF consider only the intensities of some peaks but not their positions. The *Nat-Freeze* model shows the highest uncertainty with respect of the presence of goethite, since the (101) peak of goethite is unidentifiable in the experimental diffraction pattern. For this reason we conducted two RMC refinements: one is performed by using the data calculated from the schwertmannite particle only; the second is performed by considering the presence of goethite. The variation of the χ^2 parameter with the number of moves is shown in Figure 7.5, while the calculated and experimental diffraction patterns and PDFs are reported in Figure 7.6 and 7.7. Once again the presence of goethite ensures better agreement with the experimental data. The best result is obtained with a pattern calculated by summing the pattern of the model containing 50% inner and 50% outer sulfates and the pattern of goethite, weighted 82% and 18% respectively, values very close to those obtained by Rietveld refinement. We also tested the two models with different inner/outer sulfate ratios without goethite, but their agreement was worse than the agreement obtained for the 50% inner and 50% outer models.

In view of these results, some considerations can be pointed out. A double refinement of schwertmannite was conducted, using both a non-crystalline approach in which disorder due to atom displacement was considered and a crystalline approach in which the integrity of the symmetries in the unit cell was preserved. Our results confirm the goodness of the model proposed by Fernandez-Martinez and others, with the diffraction patterns and the PDF calculated from their model adequately reproducing the experimental data. The coexistence of sulfates located in two different sites, one close to the walls of the schwertmannite octahedral framework (inner sphere sulfate) and the other in the center of the channels (outer sphere sulfate) is confirmed by both the Rietveld and RMC refinements.

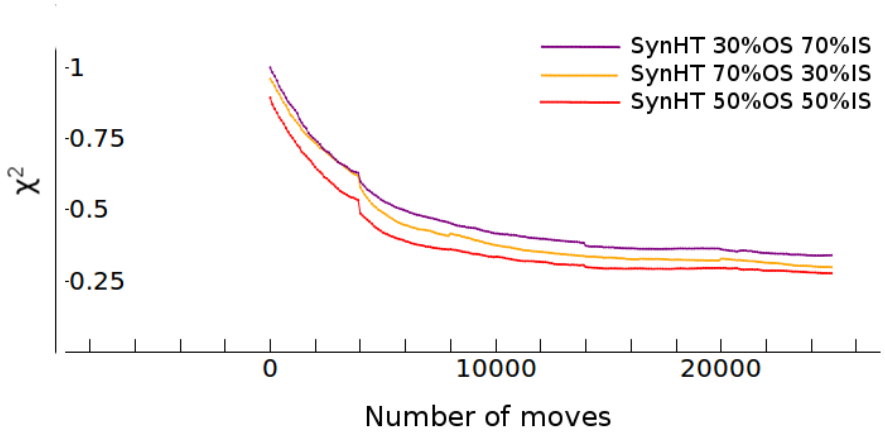

Figure 7.2: The variation of the agreement parameter χ^2 during the RMC refinement for the models showing different inner sphere sulfate (IS) / outer sphere sulfate (OS) ratio (sample SynHT).

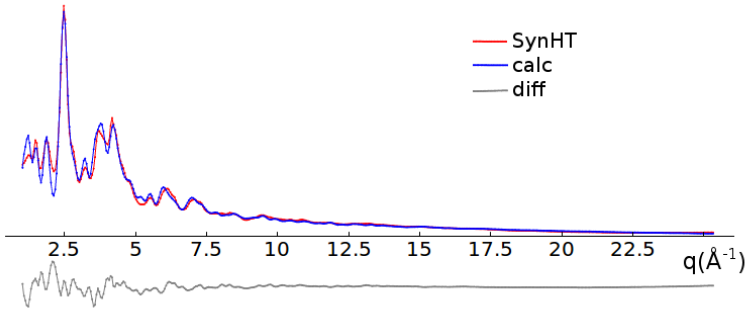

Figure 7.3: The calculated pattern of the model with 50% outer and 50% inner sphere after the RMC refinement compared with the experimental data (sample SynHT).

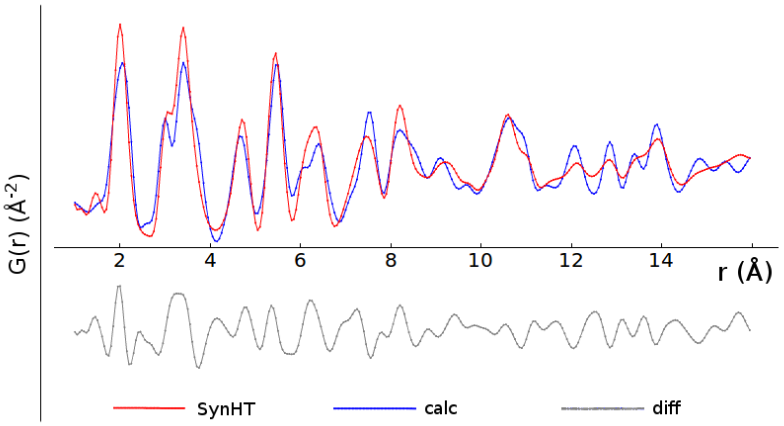

Figure 7.4: The calculated PDF of the model with 50% outer and 50% inner sphere after the RMC refinement compared with the experimental data (sample SynHT).

We obtain the best results if these two sites are equally populated. Moreover, we obtain interesting results considering the presence of other phases in our samples. The presence of goethite is confirmed by both the Rietveld and RMC refinements for all of the studied samples, even in the sample whose pattern does not show clear evidence of peaks attributable to goethite. The concentration of this phase can be roughly estimated by looking at the intensity of the peak at $2\theta = 3°$ where the (101) goethite peak falls. An interesting issue involves the possibility of the goethite network being located inside the schwertmannite structure, since in the Rietveld refinement we found values of cell parameters indicating significant distortions. It should be noted that in the refinement procedure the goethite phase is trapped in an orthorhombic symmetry, with angles fixed at 90°. Probably, a smaller change of the a and c axes could result by adding degrees of freedom to the angles. In any case, considerably less distortion is found in isolated nanogoethite samples [110]. A second interesting question is if it is possible to obtain pure schwertmannite, since we have here demonstrated that it cannot be easily inferred by looking at the diffraction pattern. A large range of values of solubility product is found in samples considered to be pure [47]. The presence of goethite should probably be taken into account in order to calculate the solubility product with a view to obtain a smaller range of values.

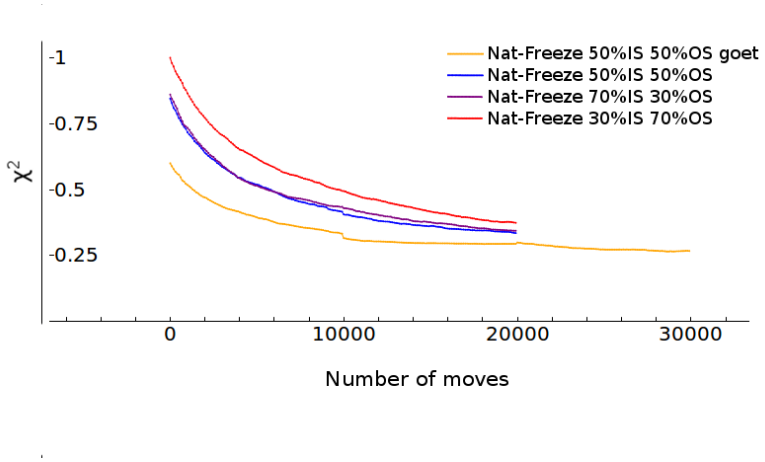

Figure 7.5: The variation of the agreement parameter χ^2 during the RMC refinement for the models showing different inner sphere sulfate (IS) / outer sphere sulfate (OS) ratio and contemplating the presence of goethite (sample Nat-Freeze).

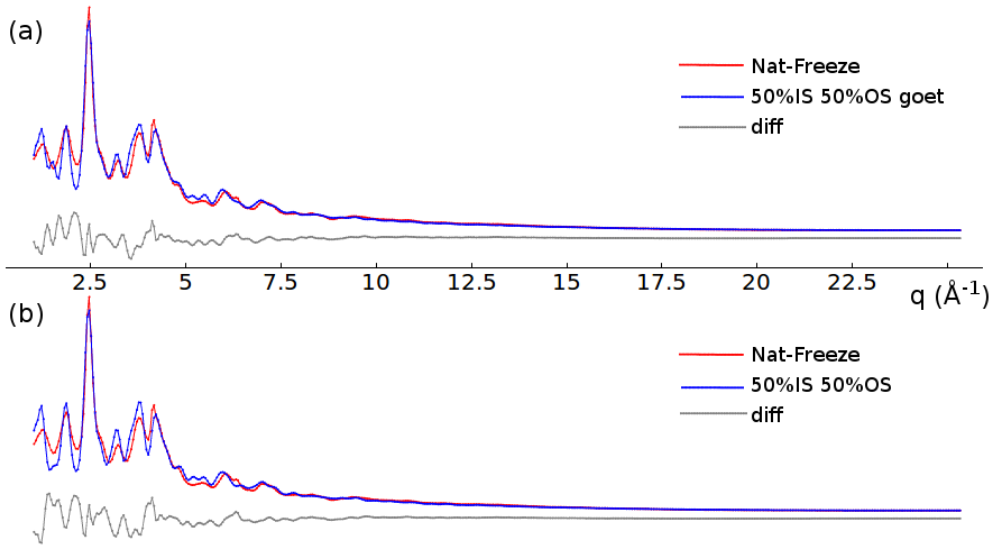

Figure 7.6: The calculated patterns of the model with 50% outer and 50% inner sphere after the RMC refinement compared with the experimental data (sample Nat-Freeze) in presence of 18% of goethite (a) and without goethite (b).

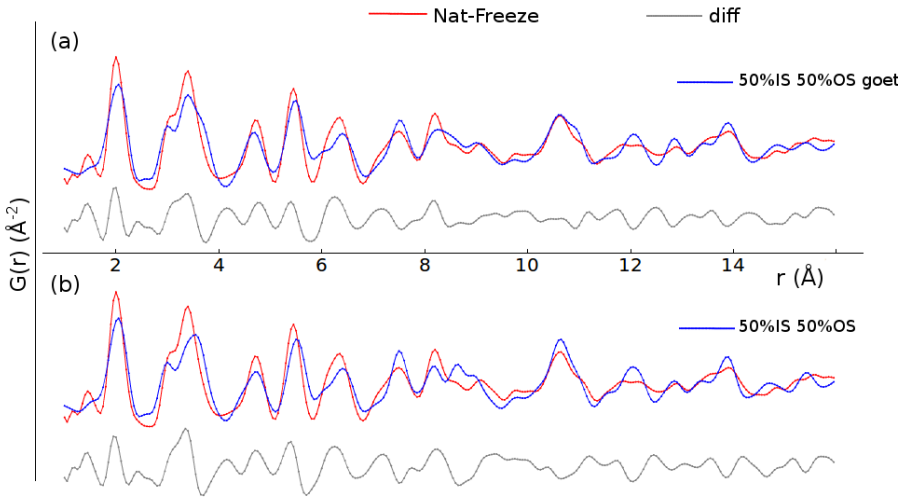

Figure 7.7: The calculated PDFs of the model with 50% outer and 50% inner sphere after the RMC refinement compared with the experimental data (sample Nat-Freeze) in presence of 18% of goethite (a) and without goethite (b).

Chapter 8

Concluding remarks and future work

In this thesis the elusive structures of three nanosized poorly-crystalline iron oxy-hydroxides, feroxyhyte, ferrihydrite and schwertmannite, are deeply studied. Different tools for the structural analysis were utilized. The widely used EXAFS and Rietveld Refinement techniques and an RMC analysis were employed in order to obtain complementary information on the structures of these materials. In particular, the RMC-like analysis was performed using a whole single particle approach which exploited the Debye Scattering Equation. A program able to refine real and reciprocal space data by applying displacements to the atoms of the model (DMC) was built and used to verify the consistency of proposed models for feroxyhyte, ferrihydrite and schwertmannite. It partially runs on GPUs, taking advantage of their computational speed, and it promises to be a suitable tool for the analysis of the structure of disordered particles with a very large number of atoms. Looking at the similarities between the structures of goethite and the model proposed by Drits and others for feroxyhyte, we hypothesized a new interpretation of the structure of this material. A disordered framework of local atomic arrangements deriving from the goethite structure and the Drits mean unit cell is tested as a representative model. This model shows common features with both goethite and the structure proposed by Drits; the presence of sharing-face octahedra, which is unusual for iron oxy-hydroxides, is not totally excluded but it appears reduced with respect to the Drits hypothesis. In the future we would like to address the study of the structure of this material, using synchrotron data which also allows the analysis of the radial distribution function, taking into account different possibilities in the stacking of the blocks. The study of the accuracy the models proposed so far for ferrihydrite (Drits and Michel) using an RMC whole particle approach was conducted performed simultaneously but independently by us and Gilbert and others, who, during the PhD period, published

an interesting paper showing the inconsistency of both Drits and Michel models in order to reproduce experimental data. In our work we reach the same conclusion. Moreover, they proposed a new disordered model showing hybrid features between Drits and Michel models. This model contemplates the controversial iron tetrahedral coordination, which is not observed in the structure of other iron oxy-hydroxides. In the future we would like to test the Gilbert model using other experimental data. The structure of schwertmannite is studied by using both the Rietveld Refinement and our DMC program. Our results show the consistency of the model proposed by Bigham and later confirmed by Fernandez-Martinez, that schwertmannite is iso-structural with the iron oxy-hydroxide akaganeite. In particular, our results verify the existence of two possible sites for the sulfates hosted in the channels (inner and outer sphere sulfates). These sites are occupied with the same probability. Interestingly, we found that better results in order to reproduce schwertmannite diffraction patterns are obtained when contemplating the presence of the additional phase goethite, thus giving new insights on the polyphasic nature of schwertmannite.

Appendix A

Part of the DMC code (main program and the routine for the calculation of the Debye Equation on GPUs) is here reported.

```
/*
       oct 21, 2014
       Cuda Version of DMC
       Modified for nspec=3 (Fe O S)
       Treating Schwertmannite structure

       Including parallel work of two gpus
       Correction for chi2 as function of intensity
       Use of spline curves to interpolate exp vs calc
       Simultaneous PDF and XRD pattern fitting
       Correction for Compton Scattering (Fe 0.33; Ox 0.66)
       Window function gaussian / hanning / gaussian+hanning

*/


 #include<stdio.h>
 #include<math.h>
 #include<stdlib.h>
 #include<gsl/gsl_multifit.h>
 #include<omp.h>
 #include<time.h>
 #include<cuda.h>
 #include<cuda_runtime.h>
```

. APPENDIX A

```
#include<sys/stat.h>



#define ID2move 1  /////////
#define nspec 3
#define pi (float) 3.141592

//setting exp condition: lambda 0.2127 (A), ESRF Grenoble wavelenght
#define lambda (float) 0.2127  //
// #define theta_monochr (float) 20.0

//setting g(r) parameters
#define deltar (float) 0.05
#define rmin (float) 1.0
#define NR 300
#define b_parameter (float) 0.05

#define w_pattern (float) 0.00001
#define w_PDF (float) 0.99999


// Forward declaration

   void Reading_dimensions(int*, char*, char*, char*);
   void Reading_exp(char*, float*, float*);
   void Reading_calc(char*, float*, float*);
   void Reading_pos(char*, int*, float*, float*, float*, int*, int*);

   void Init_list(float*, float*, float*, int*, int*, int*, float , int, int);
   void Reading_list(int*);
   void Init_fatsc2(float* , int*, float*, int*, int, int);

   void Theta_to_q(float*, float*, int);
   void Lorentz_polarization(float* , float* , int);
   void Thermal(float*, float*, int);
   void Adsorption();
```

```
   void Preferred_orientation();
   void Compton(float*, float*, int);
   void Interpolation(float*, float*, float*, float*, int, int);
   void Interpolation_spline(float*, float*, float*, float*, int, int);
   void Background_scale_coeff(float*, float*, float *, float*, float*, int);
   void Background_scale_calc(float* , float*, float*, float*, float*, float*, int);

   void PDF_calculation(float*, float*, float*, float*, float*, float*, int, float*);
   void PDF_sc_fac(float*, float*, float*, int*, int, int, float*, int*);
   void PDF_rval(float*, float*, int, float*);
   float CalculateIntegral(int, float*, float*);
   void Reading_other_phase(char*,int*);

   void Preparing_new_vectors(float*, float*, float*, float*, float*, float*, int);
   void Chisquare(float*, float*, float*, float*, float*, int, float, int);
   int Accepting(float*);
   void Move(float*, float*, float*, float*, float*, float*, int*, int, float, float,
        float, float*, float*, int, int*);
   int Chosen_atom_func(int,int*);
   void Parallel_Debye_sum(double*, float*, int, int, int, int);
   void Calculating_ints(float*, float*, float*, float*, int, float);
   void Update_vectors(float*, float*, float*, float*, float*, float*, float*, float
       *, float*, int, int);
   void Rectify_vectors(float*, float*, float*, float*, float*, float*, int);
   void Print_results(float*, float*, float*, float*, int*, int*, float*, float*,
       float*, int , int);
   __global__ void Debye_kernel(float*, float*, float*, int*, float*, float*, double
       *, float*, int, int, int);

   void print_last_CUDA_error();

//MAIN PROGRAM

  int main(){

      //make dir
      int stat;
```

```
stat = mkdir("dmcfolder",0777);

//input variables
char fileexp_name[20];
char filecalc_name[20];
char filepos_name[20];
float xmax_move, ymax_move, zmax_move;
float rlist;
float distmin[6];
float distmax[6];
float sigma;
int n_cicle;
int n_cicle_print;
int n_points[3];
char other_phases_name[20];
int n_phases;
float weight_phases[2];

//experimental XRD variables
int np_exp;
float* thetaval;
float* exp_ints;

//calculated XRD variables
int np_calc;
float* qval;
float* calc_ints;
float* incoh_ints;

//PDF variables
float* fmed2_PDF;
float* f2med_PDF;
float* calc_PDF;
float* exp_PDF;
float* rval;
float* W_function;
```

```
int other_n_atoms[nspec];

//model variables
int n_atoms;
int* atomic_number;
float* x;
float* y;
float* z;
int* moveable_list;
int n_moveable[1];

//list variables
int* neighbors_list;
int list_size;

//fatsc2 variables
float* sc_fac;
int* id_atom;
// REMEMBER: we define a matrix id_couple
// id_atom = 0 for Fe, 1 for O, 2 for S
// definited in Init_fatsc2()

//exp data treatment variables
float* exp_qval;
float* correct_exp_ints;
float* coeff;
float* backgr;

//chisquare and mc variables
int n_o;
float* chi2;
float* new_calc_ints;
float* new_x;
float* new_y;
float* new_z;
float* new_calc_PDF;
int accepted;  //1 yes; 0 no;
```

```
int n_accepted;
float* history_chi2;

//devicetohost matrix contribute
double* new_result;
double* old_result;
float* new_contribute;
float* old_contribute;

//reading settings file:
FILE *settings_file=fopen("settings.dmc","r");
fscanf(settings_file, "%s", fileexp_name);
fscanf(settings_file, "%s", filecalc_name);
fscanf(settings_file, "%d", &n_phases);
fscanf(settings_file, "%s %f", filepos_name, &weight_phases[0]);
fscanf(settings_file, "%s %f", other_phases_name, &weight_phases[1]);
fscanf(settings_file, "%f %f %f", &xmax_move, &ymax_move, &zmax_move);
fscanf(settings_file, "%f", &rlist);
fscanf(settings_file, "%f %f %f", &distmin[0], &distmin[1], &distmin[2]); //Fe-
    Fe (0+0) ; Fe-O (0+1) ; O-O (1+1)
fscanf(settings_file, "%f %f %f", &distmin[3], &distmin[4], &distmin[5]); //Fe-
    S (0+2) ; S-O (2+1) ; S-S (2+2)
fscanf(settings_file, "%f %f %f", &distmax[0], &distmax[1], &distmax[2]); //Fe-
    Fe (0+0) ; Fe-O (0+1) ; O-O (1+1)
fscanf(settings_file, "%f %f %f", &distmax[3], &distmax[4], &distmax[5]); //Fe-
    S (0+2) ; S-O (2+1) ; S-S (2+2)
fscanf(settings_file, "%f", &sigma);
fscanf(settings_file, "%d", &n_cicle);
fscanf(settings_file, "%d", &n_cicle_print);
fclose(settings_file);
sigma = sigma * sigma;


//reading exp, calc & pos file

Reading_dimensions(n_points, fileexp_name, filecalc_name, filepos_name);
```

```
np_exp = n_points[0];
np_calc = n_points[1];
n_atoms = n_points[2];

printf("number␣of␣phases:␣%d\n", n_phases);
printf("experimental␣points:␣%d,␣q␣values␣points:␣%d,␣total␣atoms␣main␣phase:␣%
    d\n", np_exp, np_calc, n_atoms);


//allocating pattern vectors
thetaval = (float *) malloc(np_exp* sizeof(float));
exp_ints = (float *) malloc(np_exp* sizeof(float));
qval = (float *) malloc(np_calc* sizeof(float));
calc_ints = (float *) malloc(np_calc* sizeof(float));
//allocating model vectors
x = (float *) malloc(n_atoms* sizeof(float));
y = (float *) malloc(n_atoms* sizeof(float));
z = (float *) malloc(n_atoms* sizeof(float));
atomic_number = (int *) malloc(n_atoms* sizeof(int));
moveable_list = (int *) malloc(n_atoms* sizeof(int));
//allocating PDF vectors
calc_PDF = (float*) malloc(NR* sizeof(float));
exp_PDF = (float*) malloc(NR* sizeof(float));
fmed2_PDF = (float*) malloc(np_calc*sizeof(float));
f2med_PDF = (float*) malloc(np_calc*sizeof(float));
rval = (float*) malloc(NR*sizeof(float));
W_function = (float*) malloc(np_calc*sizeof(float));

Reading_exp(fileexp_name,thetaval,exp_ints);

Reading_calc(filecalc_name,qval,calc_ints);

Reading_pos(filepos_name,atomic_number,x,y,z,moveable_list,n_moveable);

Reading_other_phase(other_phases_name, other_n_atoms);

printf("%d␣moveable␣atoms\n", n_moveable[0]);
```

```
      //calculating list
      list_size = 20*n_moveable[0];
      neighbors_list = (int *) malloc(list_size* sizeof(int));
      int yes;
//      printf("Do you want to read a list created before? type 1 for yes\n");
//      scanf("%d",&yes);
        yes=2;
      if (yes==1){
      Reading_list(neighbors_list);
      }
      if(yes!=1){
      printf("creating list...\n");
      Init_list(x, y, z, atomic_number, moveable_list, neighbors_list, rlist, n_atoms
          , list_size);
      }

      //calculating scattering factors

      id_atom = (int *) malloc(n_atoms* sizeof(int));
      sc_fac = (float *) malloc((2*nspec)*np_calc* sizeof(float));
      Init_fatsc2(sc_fac, id_atom, qval, atomic_number, np_calc, n_atoms);

      //treating exp data: interpolation on q correct values, background, scale,
          polarization factor

      printf("treating experimental data...\n");

      exp_qval = (float *) malloc(np_exp* sizeof(float));
      Theta_to_q(thetaval, exp_qval, np_exp);

      correct_exp_ints = (float *) malloc(np_calc* sizeof(float));

      Interpolation_spline(exp_ints, correct_exp_ints, exp_qval, qval, np_calc,
          np_exp);

      incoh_ints = (float *) malloc(np_calc* sizeof(float));
```

```
      Compton(incoh_ints, qval, np_calc);

      coeff = (float *) malloc(5* sizeof(float));
      Background_scale_coeff(correct_exp_ints, qval, calc_ints, incoh_ints, coeff,
          np_calc);

      backgr = (float *) malloc(np_calc* sizeof(float));
      Background_scale_calc(backgr, incoh_ints, correct_exp_ints, coeff, qval,
          calc_ints, np_calc);

     //calculating fmed2_PDF vector for PDF treating data and rval vector

     PDF_sc_fac(fmed2_PDF, f2med_PDF, qval, atomic_number, n_atoms, np_calc,
         weight_phases, other_n_atoms);
     PDF_rval(rval, W_function, np_calc, qval);

     //calculating PDF of experimental data

// Change here in order to calculate or to load PDF
     PDF_calculation(correct_exp_ints, exp_PDF, qval, rval, fmed2_PDF, f2med_PDF,
         np_calc, W_function);

//      printf("Remember: exp pdf file should be interpolated and named exp_PDF.dat\n
    ");
//      FILE *f99=fopen("exp_PDF.dat","r");
//      for(int i=0; i<NR; i++){
//      fscanf(f99,"%f %f \n", &rval[i], &exp_PDF[i]);
//      }
//      fclose(f99);


     //calculating PDF of start model data

     PDF_calculation(calc_ints, calc_PDF, qval, rval, fmed2_PDF, f2med_PDF, np_calc,
         W_function);

      FILE *f1=fopen("dmcfolder/start_PDF.dmc","w");
```

```
 for(int i=0; i<NR; i++){
 fprintf(f1,"%f␣%f␣%f\n", rval[i], exp_PDF[i], calc_PDF[i]);
 }
 fclose(f1);



//calculating first chisquare

chi2 = (float *) malloc(2*sizeof(float));
history_chi2 = (float *) malloc(n_cicle*sizeof(float));
n_o = 0;
Chisquare(correct_exp_ints, calc_ints, exp_PDF, calc_PDF, chi2, n_o, sigma,
    np_calc);

printf("Chisquare␣=␣%f\n", chi2[n_o]);



//DebyeMonteCarlo cycles
 //allocating montecarlo vectors
 new_calc_ints = (float *) malloc(np_calc* sizeof(float));
 new_calc_PDF = (float *) malloc(NR* sizeof(float));
 new_x = (float *) malloc(n_atoms* sizeof(float));
 new_y = (float *) malloc(n_atoms* sizeof(float));
 new_z = (float *) malloc(n_atoms* sizeof(float));
 new_contribute = (float *) malloc(np_calc* sizeof(float));
 old_contribute = (float *) malloc(np_calc* sizeof(float));

 Preparing_new_vectors(x,y,z,new_x,new_y,new_z,n_atoms);

 srand(time(NULL));

 //Preparing device. Declaring device vectors, grid specify, cudaMalloc,
     cudaMemcpy
 float* d_x0;
 float* d_y0;
 float* d_z0;
```

```
double* d_result0;
float* d_Rij0;
float* d_qval0;
float* d_sc_fac0;
int* d_id_atom0;

float* d_x1;
float* d_y1;
float* d_z1;
double* d_result1;
float* d_Rij1;
float* d_qval1;
float* d_sc_fac1;
int* d_id_atom1;


int gridx=n_atoms/32;
int gridy=np_calc/32;
printf("n blocks on x = %d\n", gridx+1);
printf("n blocks on y = %d\n", gridy+1);
new_result = (double *) malloc((gridy+1)*(gridx+1)*32*32*sizeof(double));
old_result = (double *) malloc((gridy+1)*(gridx+1)*32*32*sizeof(double));

dim3 dimBlock(32, 32);
dim3 dimGrid(gridx+1,gridy+1);

int gpuNumber, gpuID;
cudaError_t errorCode;

errorCode = cudaGetDeviceCount( &gpuNumber );
if (errorCode) printf("problem with cudaDeviceCount\n");
printf("Numero di GPU disponibili: %d\n", gpuNumber);



cudaSetDevice(0);
int device;
```

```
cudaGetDevice(&device);
printf("allocating/copying␣data␣in␣device␣%d\n", device);

cudaMalloc((void **)&d_x0, n_atoms*sizeof(float));
cudaMalloc((void **)&d_y0, n_atoms*sizeof(float));
cudaMalloc((void **)&d_z0, n_atoms*sizeof(float));
cudaMalloc((void **)&d_Rij0, n_atoms*sizeof(float));
cudaMalloc((void **)&d_result0, (gridy+1)*(gridx+1)*32*32*sizeof(double));
cudaMalloc((void **)&d_id_atom0, n_atoms*sizeof(int));
cudaMalloc((void **)&d_qval0, np_calc*sizeof(float));
cudaMalloc((void **)&d_sc_fac0, np_calc*(nspec*2)*sizeof(float));

cudaMemcpy(d_id_atom0, id_atom, n_atoms*sizeof(int), cudaMemcpyHostToDevice);
cudaMemcpy(d_qval0, qval, np_calc*sizeof(float), cudaMemcpyHostToDevice);
cudaMemcpy(d_sc_fac0, sc_fac, np_calc*(nspec*2)*sizeof(float),
    cudaMemcpyHostToDevice);



cudaSetDevice(1);
cudaGetDevice(&device);
printf("allocating/copying␣data␣in␣device␣%d\n", device);

cudaMalloc((void **)&d_x1, n_atoms*sizeof(float));
cudaMalloc((void **)&d_y1, n_atoms*sizeof(float));
cudaMalloc((void **)&d_z1, n_atoms*sizeof(float));
cudaMalloc((void **)&d_Rij1, n_atoms*sizeof(float));
cudaMalloc((void **)&d_result1, (gridy+1)*(gridx+1)*32*32*sizeof(double));
cudaMalloc((void **)&d_id_atom1, n_atoms*sizeof(int));
cudaMalloc((void **)&d_qval1, np_calc*sizeof(float));
cudaMalloc((void **)&d_sc_fac1, np_calc*(nspec*2)*sizeof(float));

cudaMemcpy(d_id_atom1, id_atom, n_atoms*sizeof(int), cudaMemcpyHostToDevice);
cudaMemcpy(d_qval1, qval, np_calc*sizeof(float), cudaMemcpyHostToDevice);
cudaMemcpy(d_sc_fac1, sc_fac, np_calc*(nspec*2)*sizeof(float),
    cudaMemcpyHostToDevice);
```

```
n_o = 1;
n_accepted = 0;




for (int i=0; i<n_cicle; i++){
  for(int nmoves=0; nmoves<n_cicle_print; nmoves++){
   int random_atom = rand()%n_moveable[0];
   int chosen_atom = Chosen_atom_func(random_atom,neighbors_list);

   Move(x, y, z, new_x, new_y, new_z, neighbors_list, random_atom, xmax_move,
       ymax_move, zmax_move, distmin, distmax, chosen_atom, atomic_number);


   #pragma omp parallel
    #pragma omp sections
     {
      #pragma omp section  //new contribution
      {
      cudaSetDevice(0);


   cudaMemcpy(d_x0, new_x, n_atoms*sizeof(float), cudaMemcpyHostToDevice);
   cudaMemcpy(d_y0, new_y, n_atoms*sizeof(float), cudaMemcpyHostToDevice);
   cudaMemcpy(d_z0, new_z, n_atoms*sizeof(float), cudaMemcpyHostToDevice);
   Debye_kernel<<<dimGrid, dimBlock>>>(d_x0,d_y0,d_z0,d_id_atom0,d_qval0,
       d_sc_fac0,d_result0,d_Rij0,n_atoms,np_calc,chosen_atom);
   cudaMemcpy(new_result,d_result0,(gridy+1)*(gridx+1)*32*32*sizeof(double),
       cudaMemcpyDeviceToHost);
   Parallel_Debye_sum(new_result, new_contribute, n_atoms, np_calc, chosen_atom,
        gridx);


      }
```

```
   #pragma omp section  //old contribution
   {
   cudaSetDevice(1);


cudaMemcpy(d_x1, x, n_atoms*sizeof(float), cudaMemcpyHostToDevice);
cudaMemcpy(d_y1, y, n_atoms*sizeof(float), cudaMemcpyHostToDevice);
cudaMemcpy(d_z1, z, n_atoms*sizeof(float), cudaMemcpyHostToDevice);
Debye_kernel<<<dimGrid, dimBlock>>>(d_x1,d_y1,d_z1,d_id_atom1,d_qval1,
    d_sc_fac1,d_result1,d_Rij1,n_atoms,np_calc,chosen_atom);
cudaMemcpy(old_result,d_result1,(gridy+1)*(gridx+1)*32*32*sizeof(double),
    cudaMemcpyDeviceToHost);
Parallel_Debye_sum(old_result, old_contribute, n_atoms, np_calc, chosen_atom,
     gridx);


   }
  }

Calculating_ints(new_calc_ints, calc_ints, old_contribute, new_contribute,
    np_calc, weight_phases[0]);

PDF_calculation(new_calc_ints, new_calc_PDF, qval, rval, fmed2_PDF, f2med_PDF
    , np_calc, W_function);

Chisquare(correct_exp_ints, new_calc_ints, exp_PDF, new_calc_PDF, chi2, n_o,
    sigma, np_calc);

accepted = Accepting(chi2);

if (accepted==1){
Update_vectors(x, y, z, new_x, new_y, new_z, calc_ints, new_calc_ints, chi2,
    n_atoms, np_calc);
n_accepted++;
}
else Rectify_vectors(x, y, z, new_x, new_y, new_z, chosen_atom);
```

```
        }

      Print_results(qval, calc_ints, rval, new_calc_PDF, atomic_number, moveable_list
          , x, y, z, np_calc, n_atoms);
      printf("chisquare = %f\n", chi2[0]);
      printf("computed %f %\n", (i+1.0)/n_cicle*100.0);
      printf("%d accepted moves\n", n_accepted);
      history_chi2[i] = chi2[0];

     }



       cudaSetDevice(0);
       cudaFree(d_x0);
       cudaFree(d_y0);
       cudaFree(d_z0);
       cudaFree(d_qval0);
       cudaFree(d_id_atom0);
       cudaFree(d_sc_fac0);
       cudaFree(d_result0);
       cudaFree(d_Rij0);

       cudaSetDevice(1);
       cudaFree(d_x1);
       cudaFree(d_y1);
       cudaFree(d_z1);
       cudaFree(d_qval1);
       cudaFree(d_id_atom1);
       cudaFree(d_sc_fac1);
       cudaFree(d_result1);
       cudaFree(d_Rij1);


//printing chi2history
```

```
      FILE *f=fopen("dmcfolder/chi2_history.dmc","w");
      fprintf(f,"TOTAL MOVES = %d\n", n_cicle*n_cicle_print);
      for(int i=0; i<n_cicle; i++){
       fprintf(f,"%d %f\n", i*n_cicle_print, history_chi2[i]);
      }
      fclose(f);

     printf("Dmc has finished! de-BYE!\n");


}



}

////////////////////////DMC routines////////////////////////


  __global__ void Debye_kernel(float*X, float*Y, float*Z, int*ida, float*Q, float*
      Fatsc2, double*In, float* Rij, int n_atoms, int NQ, int chat){

    int idx = blockIdx.x * blockDim.x + threadIdx.x;
    int id_couple[3][3];
    id_couple[0][0]=0;
    id_couple[1][0]=1;
    id_couple[0][1]=1;
    id_couple[1][1]=2;
    id_couple[2][0]=3;
    id_couple[0][2]=3;
    id_couple[1][2]=4;
    id_couple[2][1]=4;
    id_couple[2][2]=5;

    if (idx>=n_atoms) return;
```

```
    Rij[idx]=sqrt((X[idx]-X[chat])*(X[idx]-X[chat])+(Y[idx]-Y[chat])*(Y[idx]-Y[chat])
        +(Z[idx]-Z[chat])*(Z[idx]-Z[chat]));

    int idq = blockDim.y*blockIdx.y+threadIdx.y;

    if (idq>=NQ) return;

    In[idq*blockDim.x*gridDim.x+idx]=Fatsc2[idq+NQ*(id_couple[ida[idx]][ida[chat]])]*
        sin(Rij[idx]*Q[idq])/(Rij[idx]*Q[idq]);

}
```

. APPENDIX A

Appendix B

B.1 Structural analysis of feroxyhyte. Supporting materials

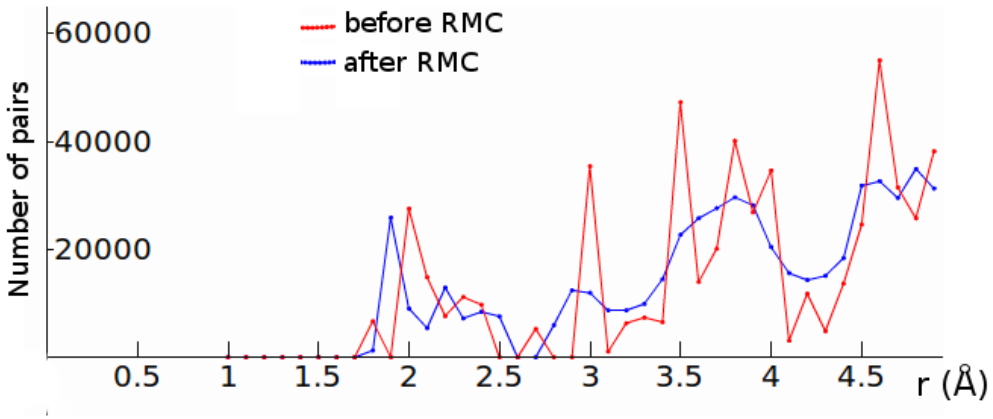

Figure 1: The number of pairs of atoms at different distances before and after the RMC refinement using DMC on the model built in order to represent the structure of feroxyhyte. The refined structure preserves the physical consistency.

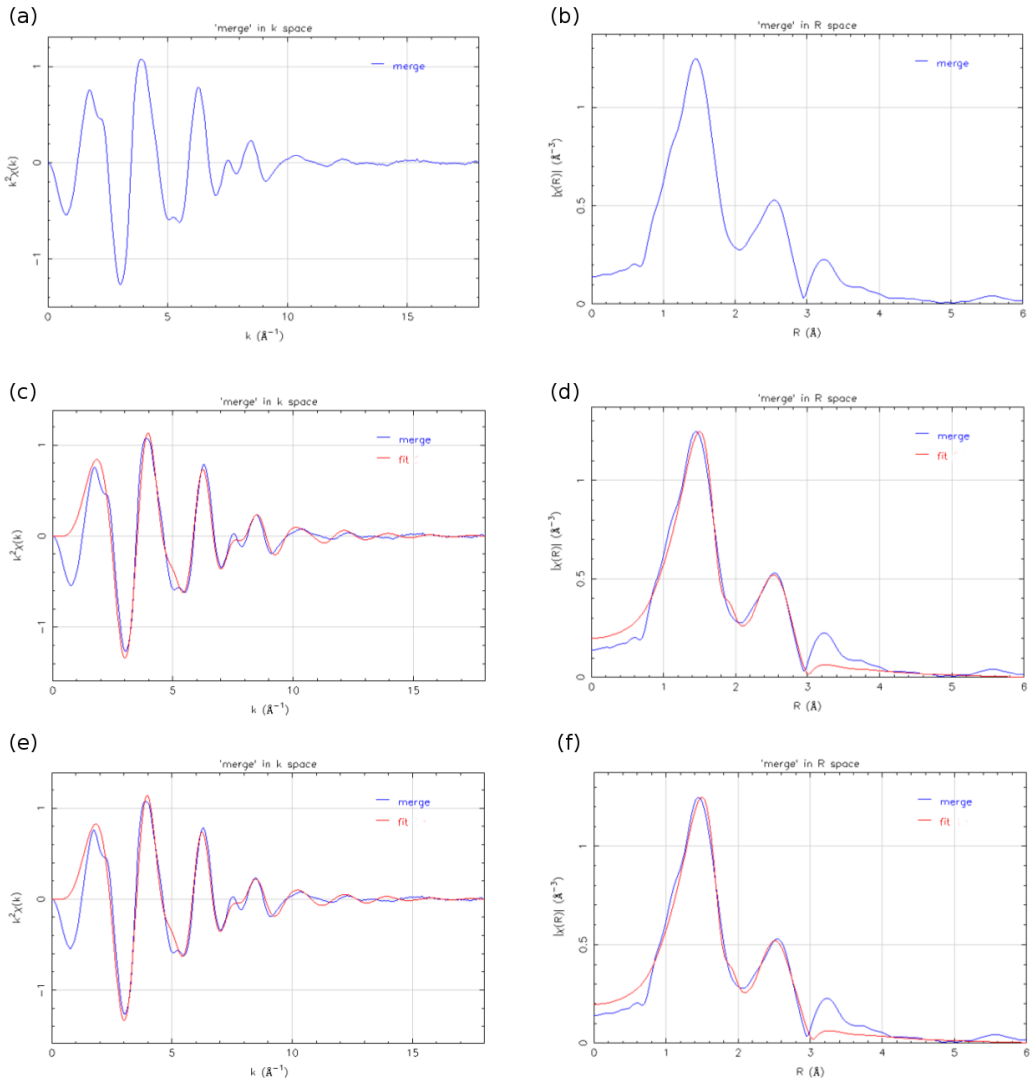

Figure 2: EXAFS study of feroxyhyte using hematite and goethite paths. The experimental EXAFS function in k space (a) and its Fourier Transform in r (b); the result of the fits using hematite paths in k space (c) and r space (d); the result of the fits using goethite paths in k space (e) and r space (f).

B.2 Structural analysis of ferrihydrite. Supporting materials

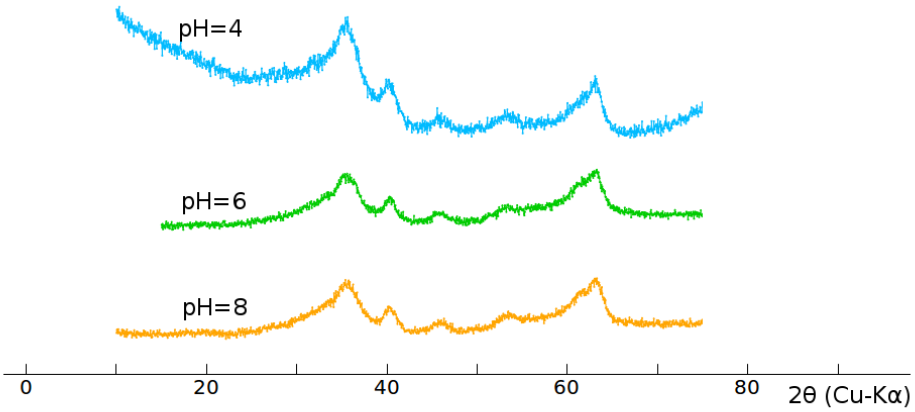

Figure 3: Diffraction patterns of the precipitate of the iron (III) nitrate solution titered at pH = 4, 6 and 8. The patterns show the characteristic six lines of ferrihydrite, indicating that this material begins its formation at low pH values.

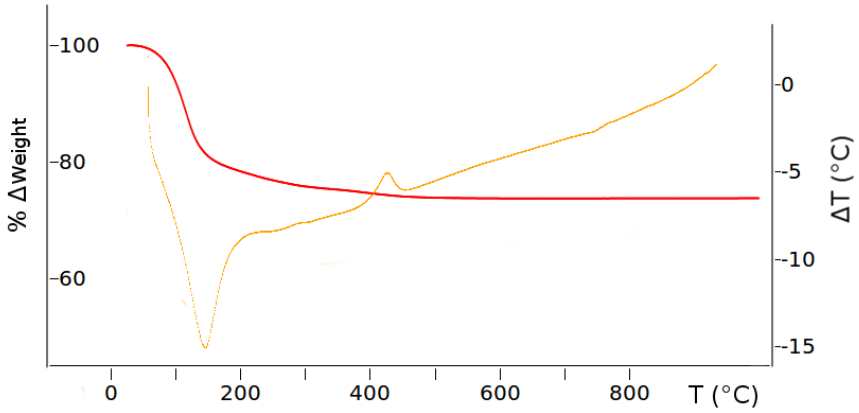

Figure 4: TGA (red) and SDTA (orange) of the ferrihydrite sample. A strong endothermic transformation occurs between 100°C and 200°C, with a loss in weight of 26%, compatible with the transformation into hematite. A small esothermic transformation occurs after 400°C

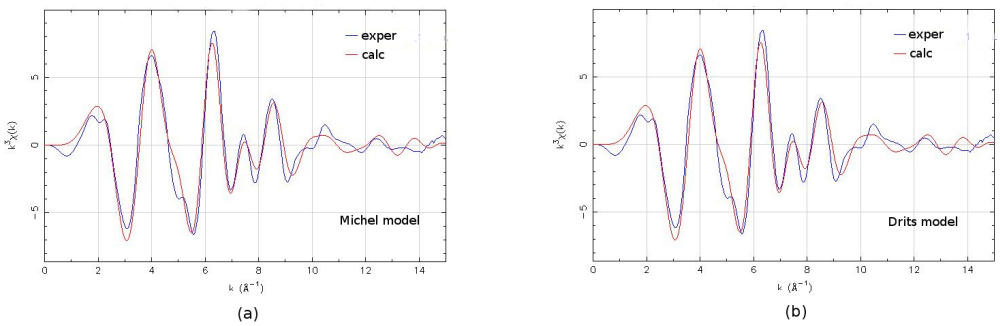

Figure 5: EXAFS fits in k space using paths calculated from the Michel model (a) and from the Drits model (b).

B.3 Structural analysis of schwertmannite. Supporting materials

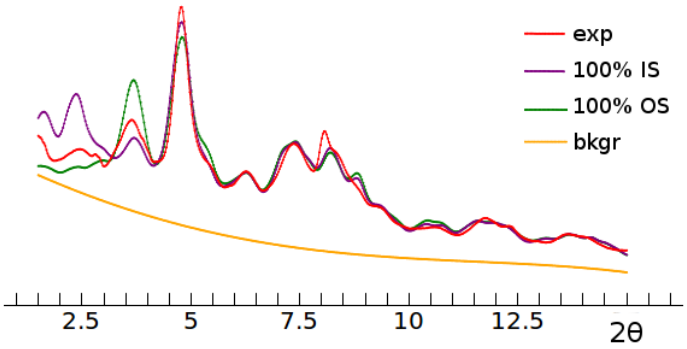

Figure 6: The influence of the inner sphere sulfate and outer sphere sulfate occupancies: a sensitivity analysis performed on the sample Nat-Air showing the patterns calculated by the Rietveld refinement from models with occupancies fixed at extreme values: 100% inner sphere sulfate and 100% outer sphere sulfate. The Rietveld refinement indicates that best agreement is obtained when the ratio ~ 1.

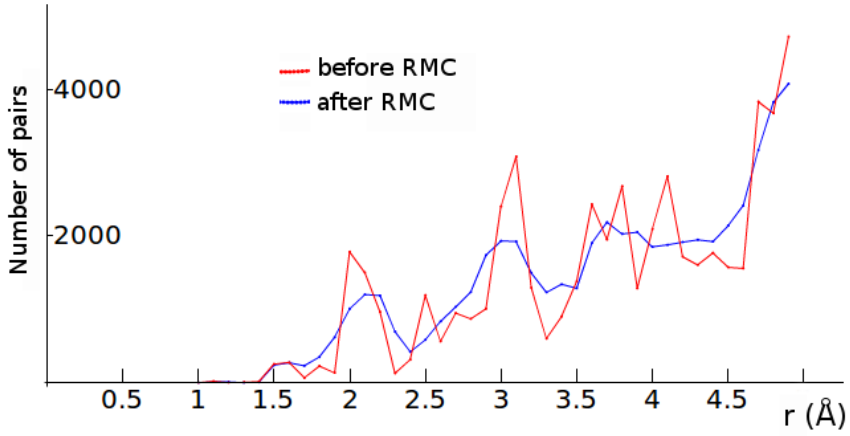

Figure 7: Number of pairs of atoms at different distances before and after the RMC refinement using DMC for the model showing the best agreement with experimental data of sample SynHT. The refined structure preserves the physical consistency

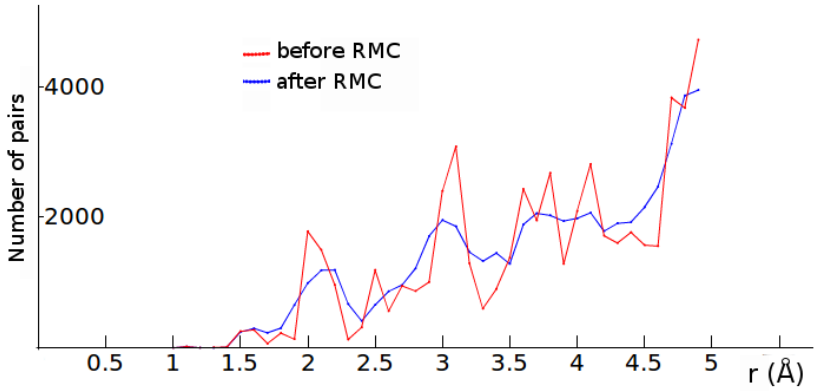

Figure 8: Number of pairs of atoms at different distances before and after the RMC refinement using DMC for the model showing the best agreement with experimental data of sample Nat-Freeze. The refined structure preserves the physical consistency

Appendix C

CIF files of the structures used for refinements are here reported

CIF file of hematite [17]

```
data_global
_chemical_name_mineral 'Hematite'
loop_
_publ_author_name
'Blake R L'
'Hessevick R E'
'Zoltai T'
'Finger L W'
_journal_name_full 'American Mineralogist'
_journal_volume 51
_journal_year 1966
_journal_page_first 123
_journal_page_last 129
_publ_section_title
;
 Refinement of the hematite structure
;
_database_code_amcsd 0000143
_chemical_formula_sum 'Fe2 O3'
_cell_length_a 5.038
_cell_length_b 5.038
_cell_length_c 13.772
_cell_angle_alpha 90
_cell_angle_beta 90
```

```
_cell_angle_gamma 120
_cell_volume 302.722
_exptl_crystal_density_diffrn      5.256
_symmetry_space_group_name_H-M 'R -3 c'
loop_
_space_group_symop_operation_xyz
  'x,y,z'
  '2/3+x,1/3+y,1/3+z'
  '1/3+x,2/3+y,2/3+z'
  'x,x-y,1/2+z'
  '2/3+x,1/3+x-y,5/6+z'
  '1/3+x,2/3+x-y,1/6+z'
  'y,x,1/2-z'
  '2/3+y,1/3+x,5/6-z'
  '1/3+y,2/3+x,1/6-z'
  '-x+y,y,1/2+z'
  '2/3-x+y,1/3+y,5/6+z'
  '1/3-x+y,2/3+y,1/6+z'
  '-x,-x+y,1/2-z'
  '2/3-x,1/3-x+y,5/6-z'
  '1/3-x,2/3-x+y,1/6-z'
  '-y,-x,1/2+z'
  '2/3-y,1/3-x,5/6+z'
  '1/3-y,2/3-x,1/6+z'
  'x-y,-y,1/2-z'
  '2/3+x-y,1/3-y,5/6-z'
  '1/3+x-y,2/3-y,1/6-z'
  'y,-x+y,-z'
  '2/3+y,1/3-x+y,1/3-z'
  '1/3+y,2/3-x+y,2/3-z'
  '-x+y,-x,z'
  '2/3-x+y,1/3-x,1/3+z'
  '1/3-x+y,2/3-x,2/3+z'
  '-x,-y,-z'
  '2/3-x,1/3-y,1/3-z'
  '1/3-x,2/3-y,2/3-z'
  '-y,x-y,z'
```

```
  '2/3-y,1/3+x-y,1/3+z'
  '1/3-y,2/3+x-y,2/3+z'
  'x-y,x,-z'
  '2/3+x-y,1/3+x,1/3-z'
  '1/3+x-y,2/3+x,2/3-z'
loop_
_atom_site_label
_atom_site_fract_x
_atom_site_fract_y
_atom_site_fract_z
Fe   0.00000   0.00000   0.35530
O   0.30590   0.00000   0.25000
loop_
_atom_site_aniso_label
_atom_site_aniso_U_11
_atom_site_aniso_U_22
_atom_site_aniso_U_33
_atom_site_aniso_U_12
_atom_site_aniso_U_13
_atom_site_aniso_U_23
Fe 0.00772 0.00772 0.00279 0.00386 0.00000 0.00000
O 0.00656 0.00800 0.00442 0.00405 0.00177 0.00365
```

CIF file of goethite[111]

```
data_global
_chemical_name_mineral 'Goethite'
loop_
_publ_author_name
'Gualtieri␣A'
'Venturelli␣P'
_journal_name_full 'American␣Mineralogist'
_journal_volume 84
_journal_year 1999
_journal_page_first 895
_journal_page_last 904
_publ_section_title
;
 In situ study of the goethite-hematite phase transformation by real time
 synchrotron powder diffraction
 Sample at T = 25 C
;
_database_code_amcsd 0002226
_chemical_formula_sum 'Fe␣H␣O2'
_cell_length_a 9.9134
_cell_length_b 3.0128
_cell_length_c 4.5800
_cell_angle_alpha 90
_cell_angle_beta 90
_cell_angle_gamma 90
_cell_volume 136.791
_exptl_crystal_density_diffrn      4.314
_symmetry_space_group_name_H-M 'P␣n␣m␣a'
loop_
_space_group_symop_operation_xyz
  'x,y,z'
  'x,1/2-y,z'
  '-x,1/2+y,-z'
  '1/2-x,1/2+y,1/2+z'
  '1/2+x,1/2-y,1/2-z'
```

```
  '1/2+x,y,1/2-z'
  '1/2-x,-y,1/2+z'
  '-x,-y,-z'
loop_
_atom_site_label
_atom_site_fract_x
_atom_site_fract_y
_atom_site_fract_z
_atom_site_U_iso_or_equiv
Fe   0.14590   0.25000  -0.04860   0.04900
H  -0.10100   0.25000  -0.39900   0.06000
O1  -0.19900   0.25000   0.28500   0.04600
O2  -0.05170   0.25000  -0.19600   0.04600
```

CIF file of defect-free ferrihydrite [32]

```
data_global
_chemical_name_mineral 'Ferrihydrite'
loop_
_publ_author_name
'Jansen␣E'
'Kyek␣A'
'Schafer␣W'
'Schwertmann␣U'
_journal_name_full 'Applied␣Physics'
_journal_volume A74
_journal_year 2002
_journal_page_first S1004
_journal_page_last S1006
_publ_section_title
;
 The structure of six-line ferrihydrite
 Sample: defect-free refinement
;
_database_code_amcsd 0012029
_chemical_compound_source 'Synthetic'
_chemical_formula_sum 'Fe.39␣O.595'
_cell_length_a 2.955
_cell_length_b 2.955
_cell_length_c 9.37
_cell_angle_alpha 90
_cell_angle_beta 90
_cell_angle_gamma 120
_cell_volume 70.857
_exptl_crystal_density_diffrn      2.934
_symmetry_space_group_name_H-M 'P␣-3␣1␣c'
loop_
_space_group_symop_operation_xyz
  'x,y,z'
  'x-y,-y,1/2+z'
  'y,-x+y,-z'
```

```
  '-y,-x,1/2-z'
  '-x+y,-x,z'
  '-x,-x+y,1/2+z'
  '-x,-y,-z'
  '-x+y,y,1/2-z'
  '-y,x-y,z'
  'y,x,1/2+z'
  'x-y,x,-z'
  'x,x-y,1/2-z'
loop_
_atom_site_label
_atom_site_fract_x
_atom_site_fract_y
_atom_site_fract_z
_atom_site_occupancy
Fe   0.33333   0.66667   0.13600   0.39000
O1   0.00000   0.00000   0.00000   0.19000
O2   0.66667   0.33333   0.25000   1.00000
```

CIF file of defective ferrihydrite [32]

```
data_global
_chemical_name_mineral 'Ferrihydrite'
loop_
_publ_author_name
'Jansen␣E'
'Kyek␣A'
'Schafer␣W'
'Schwertmann␣U'
_journal_name_full 'Applied␣Physics'
_journal_volume A74
_journal_year 2002
_journal_page_first S1004
_journal_page_last S1006
_publ_section_title
;
 The structure of six-line ferrihydrite
 Sample: defective refinement
;
_database_code_amcsd 0012028
_chemical_compound_source 'Synthetic'
_chemical_formula_sum 'Fe.48␣O'
_cell_length_a 2.955
_cell_length_b 2.955
_cell_length_c 4.685
_cell_angle_alpha 90
_cell_angle_beta 90
_cell_angle_gamma 120
_cell_volume 70.857
_exptl_crystal_density_diffrn      2.006
_symmetry_space_group_name_H-M 'P␣3'
loop_
_space_group_symop_operation_xyz
  'x,y,z'
  '-y,x-y,z'
  '-x+y,-x,z'
```

```
loop_
_atom_site_label
_atom_site_fract_x
_atom_site_fract_y
_atom_site_fract_z
_atom_site_occupancy
Fe1   0.33333   0.66667   0.16300   0.24000
Fe2   0.33333   0.66667   0.33700   0.24000
Fe3   0.33333   0.66667   0.66300   0.24000
Fe4   0.33333   0.66667   0.83700   0.24000
O1   0.00000   0.00000   0.00000   1.00000
O2   0.66667   0.33333   0.50000   1.00000
```

CIF file of Michel ferrihydrite[33]

```
data_global
_chemical_name_mineral 'Ferrihydrite'
loop_
_publ_author_name
'Michel␣F␣M'
'Ehm␣L'
'Antao␣S␣M'
'Lee␣P␣L'
'Chupas␣P␣J'
'Liu␣G'
'Strongin␣D␣R'
'Schoonen␣M␣A␣A'
'Phillips␣B␣L'
'Parise␣J␣B'
_journal_name_full 'Science'
_journal_volume 316
_journal_year 2007
_journal_page_first 1726
_journal_page_last 1729
_publ_section_title
;
 The structure of ferrihydrite, a nanocrystalline material
 Sample: Fhyd6
;
_database_code_amcsd 0015439
_chemical_compound_source 'Synthetic'
_chemical_formula_sum 'Fe4.93␣(O8␣H)'
_cell_length_a 5.928
_cell_length_b 5.928
_cell_length_c 9.126
_cell_angle_alpha 90
_cell_angle_beta 90
_cell_angle_gamma 120
_cell_volume 277.733
_exptl_crystal_density_diffrn      4.835
```

```
_symmetry_space_group_name_H-M 'P 63 m c'
loop_
_space_group_symop_operation_xyz
  'x,y,z'
  '-x,-x+y,1/2+z'
  'x-y,x,1/2+z'
  '-y,-x,z'
  '-y,x-y,z'
  'x-y,-y,1/2+z'
  '-x,-y,1/2+z'
  'x,x-y,z'
  '-x+y,-x,z'
  'y,x,1/2+z'
  'y,-x+y,1/2+z'
  '-x+y,y,z'
loop_
_atom_site_label
_atom_site_fract_x
_atom_site_fract_y
_atom_site_fract_z
_atom_site_occupancy
_atom_site_U_iso_or_equiv
Fe1   0.16950   0.83040   0.63650   1.00000   0.01100
Fe2   0.33333   0.66667   0.33790   0.97000   0.01100
Fe3   0.33333   0.66667   0.95950   0.96000   0.01100
O-H1   0.00000   0.00000   0.04460   1.00000   0.00700
O2   0.33333   0.66667   0.76340   1.00000   0.00700
O3   0.16970   0.83020   0.24670   1.00000   0.00700
O4   0.52270   0.47730   0.97960   1.00000   0.00700
```

CIF file of Schwertmannite

This is an original CIF file containing the structure of schwertmannite used in the Rietveld refinement and in RMC analysis as stacking unit of the single particle model.

```
data_schwert-1so_alex+8SO4
_audit_creation_date                2014-12-19
_audit_creation_method              'Materials Studio'
_symmetry_space_group_name_H-M      'P1'
_symmetry_Int_Tables_number         1
_symmetry_cell_setting              triclinic
loop_
_symmetry_equiv_pos_as_xyz
  x,y,z
_cell_length_a                      10.5870
_cell_length_b                      6.0622
_cell_length_c                      10.5150
_cell_angle_alpha                   90.0000
_cell_angle_beta                    87.0000
_cell_angle_gamma                   90.0000
loop_
_atom_site_label
_atom_site_type_symbol
_atom_site_fract_x
_atom_site_fract_y
_atom_site_fract_z
_atom_site_U_iso_or_equiv
_atom_site_adp_type
_atom_site_occupancy
H1     H     0.84800   0.27800   0.90500   0.00000  Uiso   1.00
H2     H     0.63300   0.04900   0.37400   0.00000  Uiso   1.00
H3     H     0.15200   0.27800   0.09500   0.00000  Uiso   1.00
H4     H     0.40704   0.41527   0.67473   0.00000  Uiso   1.00
Fe5    Fe    0.85440   0.00000   0.34240   0.00000  Uiso   1.00
Fe6    Fe    0.34520   0.00000   0.14500   0.00000  Uiso   1.00
O7     O     0.66300   0.00000   0.28830   0.00000  Uiso   1.00
O8     O     0.66200   0.00000   0.04290   0.00000  Uiso   1.00
```

O9	O	0.29465	-0.01650	0.33505	0.00000	Uiso	1.00
O10	O	0.03740	0.00000	0.32500	0.00000	Uiso	1.00
Fe11	Fe	0.35440	0.25000	0.84240	0.00000	Uiso	1.00
Fe12	Fe	0.84520	0.25000	0.64500	0.00000	Uiso	1.00
O13	O	0.16300	0.25000	0.78830	0.00000	Uiso	1.00
O14	O	0.16200	0.25000	0.54290	0.00000	Uiso	1.00
O15	O	0.79460	0.25000	0.83510	0.00000	Uiso	1.00
O16	O	0.53740	0.25000	0.82500	0.00000	Uiso	1.00
Fe17	Fe	0.14560	0.00000	0.65760	0.00000	Uiso	1.00
Fe18	Fe	0.65480	0.00000	0.85500	0.00000	Uiso	1.00
O19	O	0.33700	0.00000	0.71170	0.00000	Uiso	1.00
O20	O	0.33800	0.00000	0.95710	0.00000	Uiso	1.00
O21	O	0.70540	0.01649	0.66479	0.00000	Uiso	1.00
O22	O	0.96260	0.00000	0.67500	0.00000	Uiso	1.00
Fe23	Fe	0.64560	0.25000	0.15760	0.00000	Uiso	1.00
Fe24	Fe	0.15480	0.25000	0.35500	0.00000	Uiso	1.00
O25	O	0.83700	0.25000	0.21170	0.00000	Uiso	1.00
O26	O	0.83800	0.25000	0.45710	0.00000	Uiso	1.00
O27	O	0.20540	0.25000	0.16490	0.00000	Uiso	1.00
O28	O	0.46260	0.25000	0.17500	0.00000	Uiso	1.00
H29	H	0.84800	0.77800	0.90500	0.00000	Uiso	1.00
H30	H	0.59718	0.61123	0.31091	0.00000	Uiso	1.00
H31	H	0.15200	0.77800	0.09500	0.00000	Uiso	1.00
H32	H	0.36683	0.93454	0.62664	0.00000	Uiso	1.00
Fe33	Fe	0.85440	0.50000	0.34240	0.00000	Uiso	1.00
Fe34	Fe	0.34520	0.50000	0.14500	0.00000	Uiso	1.00
O35	O	0.66300	0.50000	0.28830	0.00000	Uiso	1.00
O36	O	0.66200	0.50000	0.04290	0.00000	Uiso	1.00
O37	O	0.29421	0.53293	0.33586	0.00000	Uiso	1.00
O38	O	0.03740	0.50000	0.32500	0.00000	Uiso	1.00
Fe39	Fe	0.35440	0.75000	0.84240	0.00000	Uiso	1.00
Fe40	Fe	0.84520	0.75000	0.64500	0.00000	Uiso	1.00
O41	O	0.16301	0.73350	0.78828	0.00000	Uiso	1.00
O42	O	0.16200	0.75000	0.54290	0.00000	Uiso	1.00
O43	O	0.79460	0.75000	0.83510	0.00000	Uiso	1.00
O44	O	0.53740	0.75000	0.82500	0.00000	Uiso	1.00
Fe45	Fe	0.14560	0.50000	0.65760	0.00000	Uiso	1.00

Fe46	Fe	0.65480	0.50000	0.85500	0.00000	Uiso	1.00
O47	O	0.33700	0.50000	0.71170	0.00000	Uiso	1.00
O48	O	0.33800	0.50000	0.95710	0.00000	Uiso	1.00
O49	O	0.70545	0.48350	0.66481	0.00000	Uiso	1.00
O50	O	0.96260	0.50000	0.67500	0.00000	Uiso	1.00
Fe51	Fe	0.64560	0.75000	0.15760	0.00000	Uiso	1.00
Fe52	Fe	0.15480	0.75000	0.35500	0.00000	Uiso	1.00
O53	O	0.83700	0.75000	0.21170	0.00000	Uiso	1.00
O54	O	0.83800	0.75000	0.45710	0.00000	Uiso	1.00
O55	O	0.20540	0.75000	0.16490	0.00000	Uiso	1.00
O56	O	0.46260	0.75000	0.17500	0.00000	Uiso	1.00
S57	S	0.47464	3.25293	-0.46403	0.00000	Uiso	0.50
O58	O	0.41235	3.46654	-0.51297	0.00000	Uiso	0.50
O59	O	0.37713	3.07957	-0.44318	0.00000	Uiso	0.50
O60	O	0.55502	3.24284	-0.34496	0.00000	Uiso	0.50
O61	O	0.55935	3.17085	-0.57390	0.00000	Uiso	0.50
S62	S	0.51541	0.76054	0.54586	0.00000	Uiso	0.50
O63	O	0.45078	0.96044	0.61494	0.00000	Uiso	0.50
O64	O	0.50256	0.56229	0.62788	0.00000	Uiso	0.50
O65	O	0.65500	0.75889	0.49302	0.00000	Uiso	0.50
O66	O	0.43636	0.71263	0.43373	0.00000	Uiso	0.50
S67	S	1.01079	0.80977	1.03074	0.00000	Uiso	0.50
O68	O	0.94617	1.00967	1.09982	0.00000	Uiso	0.50
O69	O	0.99795	0.61153	1.11276	0.00000	Uiso	0.50
O70	O	1.15038	0.80812	0.97789	0.00000	Uiso	0.50
O71	O	0.93175	0.76186	0.91860	0.00000	Uiso	0.50
S72	S	0.97002	0.30216	1.02085	0.00000	Uiso	0.50
O73	O	0.90774	0.51577	0.97190	0.00000	Uiso	0.50
O74	O	0.87252	0.12880	1.04170	0.00000	Uiso	0.50
O75	O	1.05040	0.29207	1.13992	0.00000	Uiso	0.50
O76	O	1.05473	0.22008	0.91098	0.00000	Uiso	0.50
O77	O	0.60580	0.26027	0.51143	0.00000	Uiso	0.50
O78	O	0.46879	0.25917	0.68825	0.00000	Uiso	0.50
S79	S	0.60266	0.25785	0.65198	0.00000	Uiso	0.50
O80	O	0.35414	0.76266	0.53037	0.00000	Uiso	0.50
O81	O	0.46793	0.75868	0.33884	0.00000	Uiso	0.50
S82	S	0.33967	0.75830	0.39196	0.00000	Uiso	0.50

```
O83    O     0.08890   0.48077   0.97849   0.00000  Uiso   0.50
O84    O     0.93632   0.51865   0.88103   0.00000  Uiso   0.50
S85    S     0.07551   0.49552   0.83967   0.00000  Uiso   0.50
O86    O     0.95420   0.98804   0.92539   0.00000  Uiso   0.50
O87    O     0.81044   1.01677   1.09599   0.00000  Uiso   0.50
S88    S     0.81709   1.00048   0.95840   0.00000  Uiso   0.50
loop_
_geom_bond_atom_site_label_1
_geom_bond_atom_site_label_2
_geom_bond_distance
_geom_bond_site_symmetry_2
_ccdc_geom_bond_type
H1     O15     0.965   .     S
H2     O7      0.985   .     S
H3     O27     0.965   .     S
H4     O47     0.967   .     S
Fe5    O26     1.939   .     S
Fe5    O7      2.133   .     S
Fe5    O25     2.061   .     S
Fe5    O10     1.936   1_655 S
Fe5    O53     2.061   1_545 S
Fe5    O54     1.939   1_545 S
Fe6    O28     1.996   .     S
Fe6    O27     2.121   .     S
Fe6    O9      2.044   .     S
Fe6    O20     1.981   1_554 S
Fe6    O55     2.121   1_545 S
Fe6    O56     1.996   1_545 S
O7     Fe23    2.061   .     S
O7     Fe51    2.061   1_545 S
O8     Fe23    1.939   .     S
O8     Fe18    1.981   1_554 S
O8     Fe51    1.939   1_545 S
O9     Fe24    2.194   .     S
O9     Fe52    2.051   1_545 S
O9     S82     1.574   1_545 S
O10    Fe24    1.996   .     S
```

O10	Fe5	1.936	1_455	S
O10	Fe52	1.996	1_545	S
Fe11	O20	1.939	.	S
Fe11	O48	1.939	.	S
Fe11	O47	2.061	.	S
Fe11	O19	2.061	.	S
Fe11	O13	2.133	.	S
Fe11	O16	1.936	.	S
Fe12	O22	1.996	.	S
Fe12	O21	2.051	.	S
Fe12	O50	1.996	.	S
Fe12	O49	2.050	.	S
Fe12	O26	1.981	.	S
Fe12	O15	2.042	.	S
O13	Fe17	2.061	.	S
O13	Fe45	2.061	.	S
O13	S84	1.820	.	S
O14	Fe24	1.981	.	S
O14	Fe45	1.939	.	S
O14	Fe17	1.939	.	S
O15	Fe18	2.121	.	S
O15	Fe46	2.121	.	S
O15	S88	2.014	1_545	S
O16	Fe46	1.996	.	S
O16	Fe18	1.996	.	S
Fe17	O19	2.133	.	S
Fe17	O22	1.936	1_455	S
Fe17	O41	2.135	1_545	S
Fe17	O42	1.939	1_545	S
Fe18	O21	2.046	.	S
Fe18	O8	1.981	1_556	S
Fe18	O43	2.121	1_545	S
Fe18	O44	1.996	1_545	S
Fe18	S88	2.081	1_545	S
O19	H32	1.014	1_545	S
O19	Fe39	2.061	1_545	S
O20	Fe6	1.981	1_556	S

O20	Fe39	1.939	1_545	S
O21	Fe40	2.194	1_545	S
O21	S79	1.832	.	S
O22	Fe17	1.936	1_655	S
O22	Fe40	1.996	1_545	S
Fe23	O28	1.936	.	S
Fe23	O25	2.133	.	S
Fe23	O36	1.939	.	S
Fe23	O35	2.061	.	S
Fe24	O38	1.996	.	S
Fe24	O37	2.265	.	S
Fe24	O27	2.042	.	S
O25	Fe33	2.061	.	S
O26	Fe33	1.939	.	S
O27	Fe34	2.121	.	S
O28	Fe34	1.996	.	S
H29	O43	0.965	.	S
H30	O35	0.990	.	S
H31	O55	0.965	.	S
H32	O19	1.014	1_565	S
Fe33	O54	1.939	.	S
Fe33	O35	2.133	.	S
Fe33	O53	2.061	.	S
Fe33	O38	1.936	1_655	S
Fe34	O56	1.996	.	S
Fe34	O55	2.121	.	S
Fe34	O37	2.060	.	S
Fe34	O48	1.981	1_554	S
O35	Fe51	2.061	.	S
O36	Fe51	1.939	.	S
O36	Fe46	1.981	1_554	S
O37	Fe52	1.980	.	S
O37	S82	1.573	.	S
O38	Fe52	1.996	.	S
O38	Fe33	1.936	1_455	S
Fe39	O48	1.939	.	S
Fe39	O47	2.061	.	S

Fe39	O41	2.135	.	S
Fe39	O44	1.936	.	S
Fe39	O20	1.939	1_565	S
Fe39	O19	2.061	1_565	S
Fe40	O50	1.996	.	S
Fe40	O49	2.193	.	S
Fe40	O54	1.981	.	S
Fe40	O43	2.042	.	S
Fe40	O22	1.996	1_565	S
Fe40	O21	2.194	1_565	S
O41	Fe45	1.988	.	S
O41	Fe17	2.135	1_565	S
O42	Fe52	1.981	.	S
O42	Fe45	1.939	.	S
O42	Fe17	1.939	1_565	S
O43	Fe46	2.121	.	S
O43	Fe18	2.121	1_565	S
O43	S88	2.019	.	S
O44	Fe46	1.996	.	S
O44	Fe18	1.996	1_565	S
Fe45	O47	2.133	.	S
Fe45	O50	1.936	1_455	S
Fe45	S84	2.017	.	S
Fe46	O49	2.046	.	S
Fe46	O36	1.981	1_556	S
O48	Fe34	1.981	1_556	S
O49	S79	1.758	.	S
O50	Fe45	1.936	1_655	S
Fe51	O56	1.936	.	S
Fe51	O53	2.133	.	S
Fe51	O8	1.939	1_565	S
Fe51	O7	2.061	1_565	S
Fe52	O55	2.042	.	S
Fe52	O10	1.996	1_565	S
Fe52	O9	2.051	1_565	S
Fe52	S82	2.016	.	S
O53	Fe5	2.061	1_565	S

O54	Fe5	1.939	1_565	S
O55	Fe6	2.121	1_565	S
O56	Fe6	1.996	1_565	S
S57	O59	1.481	.	D
S57	O58	1.553	.	S
S57	O60	1.551	.	S
S57	O61	1.509	.	D
S62	O64	1.481	.	D
S62	O63	1.553	.	S
S62	O65	1.551	.	S
S62	O66	1.509	.	D
O66	S82	1.168	.	S
S67	O69	1.481	.	D
S67	O68	1.553	.	S
S67	O70	1.551	.	S
S67	O71	1.509	.	D
S72	O74	1.481	.	D
S72	O73	1.553	.	S
S72	O75	1.551	.	S
S72	O76	1.509	.	D
O76	S84	1.839	1_655	S
O77	S79	1.477	.	D
O78	S79	1.448	.	S
O80	S82	1.472	.	S
O81	S82	1.441	.	D
S82	O9	1.574	1_565	S
O83	S85	1.477	.	D
S85	O84	1.521	1_455	D
S85	O76	1.839	1_455	S
O84	S85	1.521	1_655	D
O86	S88	1.477	.	S
O87	S88	1.448	.	S
S88	Fe18	2.081	1_565	S
S88	O15	2.014	1_565	S

Notes

The figures of the structures were made using the program Vesta [112]. The graphics were made using the program Fityk [113].

References

[1] Schwertmann U Cornell R M. *The Iron Oxides: Structure, Properties, Reactions, Occurrences and Uses*. Wiley, 1996. xvii, 3, 4, 9, 12, 14, 39, 44

[2] Drits V A, Sakharov B A, Salyn A L and Manceau A. *Clay Minerals*, **28**, 185–208, 1993. xvii, 12, 14, 53

[3] Drits V A, Sakharov B A and Manceau A. *Clay Minerals*, **28**, 209–222, 1993. xvii, xviii, 11, 12, 35, 37, 40, 47

[4] Bigham J M, Carlson L and Murad E. *Mineralogical Magazine*, **58**, 641648, 1994. xvii, 17, 18, 65

[5] Fernandez-Martinez A, Timon V, Ramon Ross G, Cuello G J, Daniels J E and Ayora C. *American Mineralogist*, **95**, 1312–1322, 2010. xvii, 17, 18, 65

[6] Earnshaw A Greenwood N N. *Chemistry of the Element (2nd ed.)*. Oxford: Butterworth-Heinemann, 1997. 3

[7] Towe K M and Lowenstam H A. *Journal of Ultrastructure Research*, **17**, 1–2, 1967. 3, 6

[8] Blakemore R. *Science*, **190**, 377–379, 1975. 6

[9] Eder S H, Cadiou H, Muhammad A, McNaughton P A and Winklhofer M. *Proceedings of the National Academy of Science USA*, **109**, 12022–27, 2012. 6

[10] Kirschvink J L and Gould J L. *Biosystems*, **13**, 181–201, 1981. 6

[11] Mouritsen H and Ritz T. *Current opinion in neurobiology*, **15**, 406–414, 2005. 6

[12] Carlson L and Schwertmann U. *Clays and Clay Minerals*, **28**, 272–280, 1980. 6, 36

[13] Jambor J L and Dutrizac J E. *Chemical Review*, **98**, 2549–2585, 1998. 6

[14] Chasteen N D and Harrison P M. *Journal of Structural Biology*, **126**, 182–194, 1999. 6

[15] Everett J, Cespedes E, Schelford L R, Exley C, Collingwood J F, Dobson J, Van der Laan G, Jenkins C A, Arenholz E, and Telling N D. *Inorganic Chemistry*, **53**, 2803–2809, 2014. 6

[16] Schwertmann U, Bigham J M and Murad E. *European Journal of Mineralogy*, **7**, 547–552, 1995. 6

[17] Blake R L, Hessevick R E, Zoltai T and Finger L W. *American Mineralogist*, **51**, 123–129, 1966. 7, 35, 103

[18] Fleet M E. *Acta Crystallographica*, **B37**, 917–920, 1981. 7

[19] Greaves C. *Journal of Solid State Chemistry*, **49**, 325, 1983. 7

[20] Szytula A, Burewicz A, Dimitrijevic Z, Krasnicki S, Rzany H, Todorovic J, Wanic A and Wolski W. *Physica Status Solidi*, **26**, 429–434, 1968. 7, 36

[21] Wyckoff R W G. *Crystal Structures*, **1**, 290–295, 1963. 7

[22] Post J E and Buchwald V F. *American Mineralogist*, **76**, 272–277, 1991. 7, 36

[23] Okamoto S. *Journal of the American Ceramic Society*, **51**, 594–599, 1968. 9, 14, 36

[24] Patrat G, De Bergevin F, Pernet M and Joubert J C. *Acta Crystallographica*, **B39**, 165–170, 1983. 11, 35

[25] Sestu M, Carta D, Casula M F, Corrias A and Navarra G. *Journal of Solid State Chemistry*, **225**, 256–260, 2015. 14

[26] Janney D E, Cowley J M and Buseck P R. *American Mineralogist*, **85**, 1180–1187, 2000. 14

[27] Towe K M and Bradley W F J. *Journal of Colloid and Interface Science*, **601**, 460–474, 1967. 14, 15

[28] Chukhrov F V, Zvyagin B B, Gorshkov A I, Yermilova L P and Balashova V V. *Izvestiya Akademii Nauk SSSR Ser. Geol.*, **4**, 23–33, 1973. 14

[29] Eggleton R A and Fitzpatrick R W. *Clays and Clay Minerals*, **36**, 111–124, 1988. 14

[30] Manceau A and Drits V A. *Clay Minerals*, **28**, 165–184, 1993. 14, 45

[31] Janney D E, Cowley J M and Buseck P R. *American Mineralogist*, **86**, 327–335, 2000. 14

[32] Jansen E, Kyek A, Schafer W and Schwertmann U. *Applied Physics A Materials Science and Processing*, **74**, S1004–S1006, 2002. 14, 55, 109, 111

[33] Michel F M, Ehm L, Antao S M, Lee P L, Chupas P J, Liu G, Strongin D R, Schoonen M A A, Phillips B L and Parise J B. *Science*, **316**, 1726–1729, 2007. 14, 53, 56, 113

[34] Rancourt D G and Meunier J F. *American Mineralogist*, **93**, 1412–1417, 2008. 15

[35] Manceau A. *Clay Minerals*, **44**, 19–34, 2009. 15, 63

[36] Manceau A. *Clay Minerals*, **45**, 225–228, 2010. 15, 61

[37] Michel F M, Barron V, Torrent J, Morales M P, Serna C J, Boily J F, Liu Q S, Ambrosini A, Cismasu A C and Brown G E. *Proceedings of the Natonal Academy of Sciences*, **107**, 2787–2792, 2010. 15, 61

[38] Maillot F, Morin G, Wang Y, Bonnin D, Ildefonse P, Chaneac C and Calas G. *Geochimica and Cosmochimica Acta*, **75**, 2708–2720, 2011. 15, 61

[39] Harrington R, Hausner D B, Wu W, Bhandari N, Michel F M, Brown G E Jr, Strongin D R and Parise J B. *Environmental Science and Technology*, **45**, 9883–9890, 2011. 15

[40] Manceau A. *American Mineralogist*, **96**, 521–533, 2011. 15

[41] Gilbert B, Erbs J J, Penn R L, Petkov V, Spagnoli D and Waychunas G A. *American Mineralogist*, **98**, 1465–1476, 2013. 15, 53, 63

[42] Loan M, Cowley J M, Hart R and Parkinson G M. *American Mineralogist*, **89**, 1735–1742, 2004. 17

[43] Hockridge J C, Jones F, Loan M and Richmond W R. *Journal of Crystal Growth*, **311**, 3876–3882, 2009. 17

[44] French R A, Monsegue N, Murayama M and Hochella M F. *Physics and Chemistry of Minerals*, **41**, 237–246, 2014. 17

[45] French R A, Caraballo M A, Kim B, Rimstidt J D, Murayama M and Hochella M F. *American Mineralogist*, **97**, 1469–1482, 2012. 17, 65, 70

[46] Bigham J M, Schwertmann U, Traina S J, Winland R L and Wolf M. *Geochimica et Cosmochimica Acta*, **60**, 2111–2121, 1996. 17, 65

[47] Caraballo M A, Rimstidt J D, Macas F, Nieto J M and Hochella M F J. *Chemical Geology*, **360-361**, 22–31, 2013. 17, 73

[48] Bragg L W. *The Crystalline State: Volume I*. New York: The Macmillan Company, 1934. 19

[49] Klug A. *Chemica Scripta*, **14**, 245–256, 1978. 20

[50] Zou X D and Hovmoller S. *Acta Crystallographica*, **A64**, 149–160, 2008. 20

[51] Lutterotti L and Scardi P. *Journal of Applied Crystallography*, **23**, 246–252, 1990. 20

[52] Caglioti G, Paoletti A and Ricci F P. *Nuclear Instrument and Methods*, **3**, 223–228, 1958. 20

[53] Warren B E and Averbach B L. *Journal of Applied Physics*, **21**, 595–599, 1950. 20

[54] Will G. *Powder Diffraction: The Rietveld Method and the Two Stage Method to Determine and Refine Crystal Structures from Powder Diffraction Data*. Springer, 2006. 20

[55] Rietveld H M. *Journal of Applied Crystallography*, **2**, 65–71, 1969. 20, 22

[56] Scardi P and Leoni M. *Acta Crystallographica*, **A58**, 190–200, 2002. 20

[57] Egami T and S J L Billinge. *Underneath the Bragg Peaks (2nd Ed.)*. Pergamon - Elsevier, 2012. 21

[58] Compton H A. *Physical Review*, **21**, 483–502, 1923. 21

[59] Warren B E. *X-ray Diffraction*. Dover Publications, 1991. 21

[60] Klug H P and Alexander L E. *X-ray diffraction procedures for polycrystalline and amorphous materials (2nd Ed.)*. Wiley, New York, USA, 1974. 22

[61] Debye P. *Annalen der Physik*, **46**, 809–823, 1915. 23

[62] Neder R B, Korsunskiy V I, Chory C, Muller G, Hofmann A, Dembsky S, Graf C and Ruhl E. *Physica Status Solidi*, **4**, 3221–3233, 2007. 24

[63] Buljan M, Desnica U V, Radic N, Drazic G, Matej Z, Vales V and Holy V. *Journal of Applied Crystallography*, **42**, 660–672, 2009. 24

[64] Page K, Hood T C, Proffen Th and Neder R B. *Journal of Applied Crystallography*, **44**, 327–336, 2011. 24

[65] Harrington R, Neder R B and Parise J B. *Chemical Geology*, **5**, 3–9, 2012. 24

[66] Germer L H and White A H. *Physical Review*, **60**, 447, 1941. 24

[67] Hall B D and Monot R. *Computational Physics*, **5**, 414–417, 1991. 24

[68] Cervellino A, Giannini C and Guagliardi A. *Journal of Applied Crystallography*, **36**, 1148–1158, 2003. 24

[69] Cervellino A, Giannini C and Guagliardi A. *Journal of Computational Chemistry*, **36**, 995–1008, 2006. 24

[70] Gelisio L, Azanza Ricardo C L, Leoni M and Scardi P. *Journal of Applied Crystallography*, **43**, 995–1008, 2006. 24, 32

[71] Antonov L D, Andreetta C and Hamelryck T. *Proceedings of the International Conference on Bioinformatics Models, Methods and Algorithms*, 2012. 24

[72] Proffen Th and Billinge S J L. *Journal of Applied Crystallography*, **3**, 572–575, 1999. 25

[73] Farrow C L, Juhs P, Liu J W, Bryndin D Bozin E S, Bloch J, Proffen Th and Billinge S J L. *Journal of Physic Condensed Matter*, **19**, 335219, 2007. 25

[74] Beer A. *Annalen der Physik und Chemie*, **86**, 77–78, 1852. 25

[75] Lambert J H. *Photometria sive de mensura et gradibus luminis, colorum et umbrae*. 1760. 25

[76] Sayers D E, Stern E A and Lytle F W. *Physical Review Letters*, **27**, 1204–1207, 1971. 26

[77] Stern E A. *Scientific American*, **234**, 96, 1976. 26

[78] Ravel B and Newville M. *Journal of Synchrotron Radiation*, **12**, 537–541, 2005. 26, 45, 55

[79] McGreevy R L and Pusztai L. *Molecular Simulation*, **1**, 359–367, 1988. 27, 28

[80] *Cuda Programming Guide 2.3*. NVIDIA Corp. 28

[81] Keen D A and McGreevy R L. *Nature*, **334**, 423–425, 1990. 28

[82] Evans R. *Molecular Simulation*, **4**, 409–411, 1990. 28

[83] Tucker M G, Keen D A, Dove M T, Goodwin A L and Hui Q. *Journal of Physics: Condensed Matter*, **19**, 335218, 2007. 28

[84] Gurman S J and McGreevy R L. *Journal of Physics: Condensed Matter*, **2**, 9463–9473, 1990. 28

[85] Wojdyr M. *http://www.unipress.waw.pl/debyer*. 2011. 30

[86] GSL libraries. *http://www.gnu.org/software/gsl*. 30, 59

[87] Galassi M et al. *GNU Scientific Library Reference Manual (3rd Ed.)*. 30

[88] Harris M J. *GPU Gems, Fast fluid dynamics simulation on the GPU*. NVIDIA Corp., 2004. 31

[89] Owens J D, Luebke D, Govindaraju N, Harris M J, Kruger J, Lefhon A E and Purcell T J. *Computer Graphics Forum*, **26**, 80–113, 2007. 31

[90] Kruger J and Westermann R. *Proceedings of SIGGRAPH*, pages 908–916, 2003. 31

[91] GeForce gtx 690 Specfications. *http://www.geforce.com/hardware/desktop-gpus/geforce-gtx-690/specifications*. 33

[92] OPEN MP. *http://www.openmp.org*. 33

[93] Francombe M H and Rooksby H P. *Clay Minerals Bulletin*, **4**, 1–14, 1959. 35

[94] Ewing F J. *Journal of Chemical Physics*, pages 420–424, 1935. 36

[95] Watari F, Van Landuty J, Detavignette P and Amelinckx S. *Journal of Solid State Chemistry*, **29**, 417–427, 1979. 44

[96] Nesterova M, Moreau J and Banfield J F. *Geochimica Cosmochimica Acta*, **67**, 1177–1187, 2003. 44

[97] Yang H, X Zhou X, Tang T, Qi X, Wang C, Lan J, Wang Y, Yang Y and Liu G. *CrystEngComm*, **12**, 4007–4011, 2010. 44

[98] Cornell R M Schwertmann U. *The Iron Oxides in The Laboratory*. Wiley, 2000. 45, 66

[99] Harris F J. *Proceedings of the IEEE*, **66**, 51, 1978. 45, 56

[100] Rehr J J, Kas J J, Prange M P, Sorini A P, Takimoto Y and Vila F D. *Comptes Rendus Physique*, **10**, 548–559, 2009. 45, 55

[101] Carta D, Casula M F, Corrias A, Falqui A, Navarra G and Pinna G. *Materials Chemistry and Physics*, **113**, 349–355, 2009. 54, 61

[102] Acero P, Ayora C, Torrento C and Nieto J M. *Geochimica et Cosmochimica Acta*, **70**, 4130–4139, 2006. 65

[103] Burton E D, Bush R T, Sullivan L A and Mitchell D R G. *Geochimica et Cosmochimica Acta*, **72**, 4551–4564, 2008. 65

[104] Jonsson J, Persson P, Sjoberg S and Lovgren L. *Applied Geochemistry*, **20**, 179–191, 2005. 65

[105] Knorr K H and Blodau C. *Applied Geochemistry*, **22**, 2006–2015, 2007. 65

[106] Regenspurg S, Brand A, and Peiffer S. *Geochimica et Cosmochimica Acta*, **68**, 1185–1197, 2004. 65

[107] Schwertmann U and Carlson L. *Clay Minerals*, **40**, 63–66, 2005. 65

[108] Hammersley A P. *ESRF Internal Report*, ESRF97HA02T, 1997. 66

[109] Lutterotti L. *Nuclear Instruments and Methods in Physics Research*, **B268**, 334–340, 2010. 66

[110] Christensen A N, Jensen T R, Bahl C R H and Di Masi E. *Journal of Solid State Chemistry*, **180**, 1431–1435, 2007. 73

[111] Gualtieri A and Venturelli P. *American Mineralogist*, **84**, 895–904, 1999. 107

[112] Momma K and Izumi F. *Journal of Applied Crystallography*, **44**, 1272–1276, 2011. 123

[113] Wojdyr M. *Journal of Applied Crystallography*, **43**, 1126–1128, 2010. 123